A report to the sponsors of the
Exploration Geophysics Laboratory

Direct-S and Direct-P Modes Produced by Point Sources, Variable-Depth Shot Holes, Shot-Hole Arrays, and Vibrator Arrays

Bob Hardage and Don Wagner

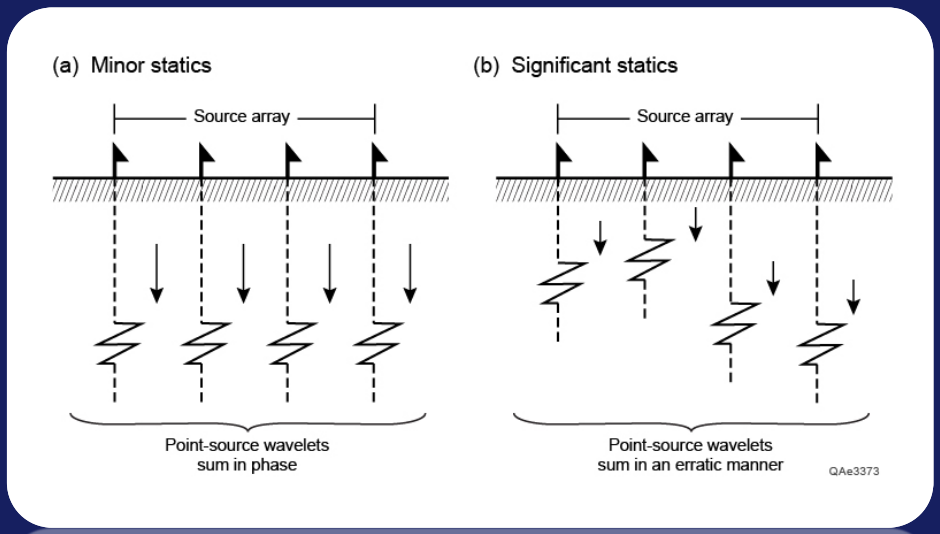

December 2015

EGL Exploration Geophysics Laboratory

Bureau of Economic Geology

QAe4347

A report to the sponsors of the
Exploration Geophysics Laboratory

Direct-S and Direct-P Modes Produced by Point Sources, Variable-Depth Shot Holes, Shot-Hole Arrays, and Vibrator Arrays

Bob Hardage and Don Wagner

December 2015

BUREAU OF ECONOMIC GEOLOGY

Table of Contents

Direct-S and Direct-P Modes Produced by Point Sources, Variable-Depth Shot Holes, Shot-Hole Arrays, and Vibrator Arrays

Bob A. Hardage and Don Wagner

December 2015

Abstract

The optimal source for generating direct-S waves is a point source. However, legacy P-wave seismic data that can be reprocessed to create SV-P images have usually been acquired with source arrays, not with point sources. To aid in extending direct-S imaging with P-wave sources to legacy P-wave data, the Exploration Geophysics Laboratory (EGL) conducted a series of source tests at the Devine Test Site south of Hondo, Texas to determine how direct-S and direct-P modes produced by source arrays compare with direct-S and direct-P modes produced by point sources. In these tests, data were acquired with a sequence of point sources that were successively positioned at closely spaced source stations distributed across a small, square, X-Y area of the test site. These point sources included two vertical-displacement sources – a single vertical vibrator and an explosive in a single shot-hole, and two horizontal-displacement sources – a single radial-horizontal vibrator and a single transverse-horizontal vibrator.

Downgoing illuminating wavefields produced by these sources were recorded by a receiver array consisting of forty-two 3-component geophones stationed at vertical intervals of 50 ft (49.2 m) in well 9 on the Devine Test Site property. The wavefields recorded by this vertical receiver array were then examined as each point source was positioned at each source station across the X-Y source-test pattern to determine how direct-S and direct-P waveshapes were altered from station to station by local variations in soil stiffness coefficients. Comparisons of wavelets produced by closely spaced point sources illustrate shifts in wavelet origin time caused by intra-array S and P source-station statics. This report compares deep-receiver illuminating wavelets produced by point sources and by source arrays to illustrate the effect of intra-array P-wave and S-wave statics across large-dimension source arrays.

Test data were also acquired for explosives positioned at different depths to determine how the primary direct-S mode from a buried explosive charge and the secondary direct-S modes that reflect from the earth-air interface above a buried shot combine to form the total downgoing illuminating S wavefield associated with buried-explosive sources. An insight into this basic physics of buried-source wavefields is essential for deciding how shot depth affects direct-S modes embedded in legacy seismic data generated by explosive sources.

This report has three appendices. Appendix A discusses an unusual secondary S mode called the S* wave that has been proposed by a few theorists to be generated when a buried pure-P source (meaning the source produces no direct-S modes) is positioned near the earth surface. This appendix summarizes attempts by other researchers to verify the existence of an S* mode with real data. An S* mode has been produced in only one real-data case where a small-scale physical model utilized a special buried source that generated much stronger direct-P radiation than direct-S radiation. No one has yet identified an S* wave in real seismic data. No evidence of an S* wave could be found in the source-test data acquired at the Devine Test Site.

Appendix B presents photographs of surface conditions local to source stations utilized in this source test where vibrator pad imprints implied there were significant station-to-station changes in soil stiffness coefficients. This photographic evidence indicates how difficult it is to conclude by visual inspection if physical conditions at a source station will or will not cause significant variations in direct-S modes produced at that station.

Appendix C illustrates specific data windows in the 42-station vertical profile where deep body-wave wavelets were extracted to use in the wavelet analyses in the main text of this report

Introduction

The ideal seismic source for generating direct-S modes is a point source. The reason is that for some near-surface conditions, S-wave static corrections can change over short distances. P-wave statics usually do not vary over short distances because near-surface V_P velocities tend to stabilize when shallow strata are fully, or partially, water saturated. In contrast, water saturation and depth of water table have only small effects on near-surface V_S velocities. Both V_P and V_S statics can be influenced by variations in soil porosity, spatial changes in mineral percentages, and lateral changes in soil stiffness coefficients in near-surface strata. However, variations in these physical parameters of surface soils are difficult to recognize by visual inspection as shown by the photographs in Appendix B.

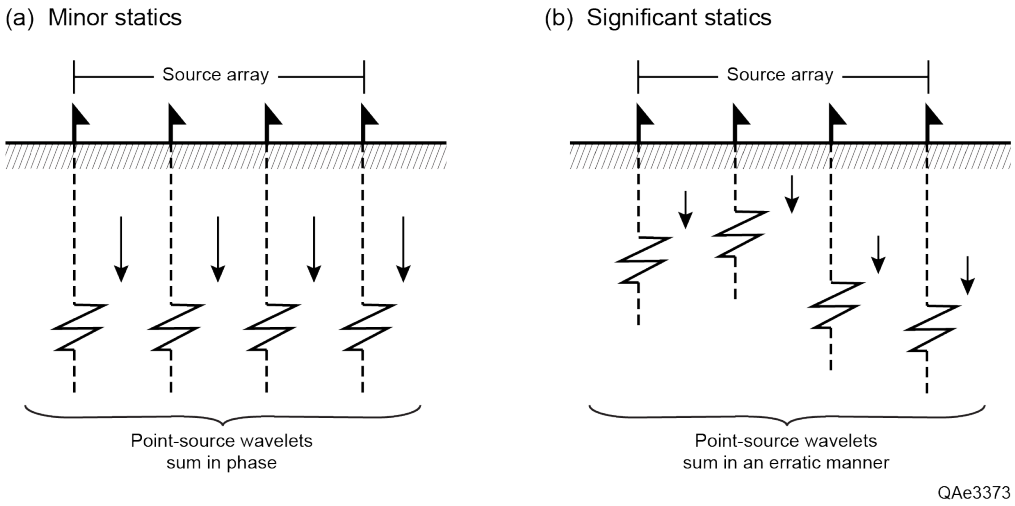

Figure 1. Effect of intra-array S-wave source static variations on illuminating direct-SV wavefields. Each flag is a point source within an array source. (a) Source array with minor intra-array static variations. (b) Source array with significant intra-array static variations. For each array, the direct-SV wavelet that illuminates deep geology is the sum of the four point-source wavelets.

EGL's current working hypothesis is that even though direct-P data produced by a large source array may not be affected by intra-array changes in P statics, direct-S data produced by that same source array may be significantly affected by intra-array variations in S-wave statics. In Figure 1, four point sources form a large-dimension source array. The propagating direct-SV wavelet created by this 4-source array is the sum of the four direct-SV wavelets produced by the four individual point sources. The array wavelet will be a copy of the point-source wavelet if there are negligible S-wave static changes across the array dimension (Figure 1a). In contrast, the array will produce a distorted illuminating wavelet if significant S-wave statics exist within the source array (Figure 1b). No intra-array source statics are involved when a single point source is used, which is the principal advantage of point sources over source arrays for both direct-S and direct-P imaging.

Because EGL desires to expand its direct-S technology to legacy seismic data, it is essential to analyze how source array size and shape affect the wavelet character and frequency content of direct-S modes. The test data illustrated and discussed in this EGL sponsor report are a step toward achieving this understanding. EGL is particularly interested in analyzing direct-P and direct-S modes when source arrays consist of three or four inline vibrators or shot holes because these source-geometries are common source arrays that are encountered in legacy seismic data.

Sources and Receivers Used to Generate Test Data

These source-test data were acquired at the Devine Test Site managed by the Exploration Geophysics Laboratory (EGL). Details about the Devine Test Site can be found in the public portion of the EGL Sponsors Web site (**http//www.beg.utexas.edu/egl/).** It is not necessary to have a user name or password to access the test-site information found at this URL address. Access to these same Web pages occurs when the term, **devine test site**, is requested of any reliable Web search engine. Descriptions of the Devine Test Site will not be presented in this report. Readers wishing to know details about the test site should use one of these Web search options and utilize the material available to the general public.

Source 1: Vibrators

Two vertical vibrators, two horizontal vibrators, and vibrator support personnel were provided by Dawson Geophysical as no-cost support of this EGL research. Each vertical vibrator was a 60,000 lb I/O AHV IV 362 model operated with a drive level of 80-percent. Each horizontal vibrator was a 54,000-lb Mertz model M18-623 operated with a hold-down weight of 30,000 lbs and a drive level of 70-percent. Operating parameters for the vertical vibrator were a 24-sec, linear-rate sweep extending from 4 to 96 Hz and a listen time of 6 sec (Figure 2). Operating parameters for the horizontal vibrators were a 12-sec, linear-rate sweep extending from 4 to 48 Hz and a listen time of 6 sec (Figure 2). Taper windows 300-ms long were used for sweeps generated by both vertical and horizontal vibrators.

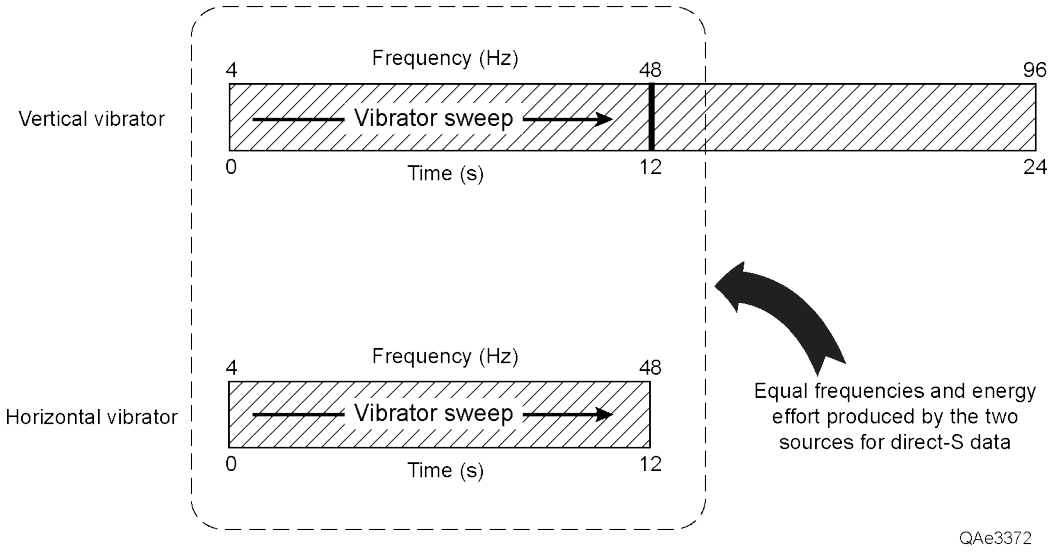

Figure 2. Sweep parameters used for the vertical vibrator and the horizontal vibrator. Long, linear-rate sweeps were used so direct-SV modes would have robust low-frequency energy content. Vertical and horizontal vibrators executed identical sweeps between 4 and 48 Hz in an attempt to ensure the direct-SV modes produced by both sources were identical over this frequency range. The vertical vibrator sweep then continued to 96 Hz.

The sweep parameters used for the 4 to 48 Hz portion of the vertical-vibrator sweep were exactly the same as the parameters used for the 4 to 48 Hz sweep of the horizontal vibrator; i.e., each baseplate vibrated for 12 sec in a linear-rate fashion between 4 and 48 Hz (Figure 2). The only difference was that the 300-ms taper window for the vertical-vibrator sweep occurred at 96 Hz, not at 48 Hz as it did for the horizontal vibrator. The equivalence of these operating parameters for the 4-to-48-Hz sweep range were an effort to ensure equal frequencies and equal energy content would exist in direct-SV data produced by the vertical vibrator and the horizontal vibrator used in these source tests. Whatever energy contribution to the illuminating SV wavefield was added by the vertical vibrator for frequencies higher than 48 Hz was left embedded in the vertical-vibrator data. No frequency filtering was done to limit the upper end of the vertical-vibrator frequency spectrum.

Source 2: Shot-Hole Explosives

For purposes of source-array tests, shot-holes were drilled to a depth of 20 ft (6 m) and loaded with a 1-kg (2.2 lb) charge. However, to analyze the effects of shot-hole depth on direct-SV modes, additional shot-holes were also drilled to depths of 150 ft (45 m), 100 ft (30 m), and 50 ft (15 m). Each of these deeper shot-holes was also loaded with a 1-kg (2.2 lb) charge. Firing caps were standard electrical type, not solid-state type. Explosives and firing caps were provided by Austin Powder, an EGL sponsor.

Receivers

Three-component (3C) VSP receivers were deployed in well 9 on the Devine Test Site to record the source-array test data presented in this report. Halliburton, an EGL sponsor, provided the wireline services, deployed the downhole sensor array, and recorded the test data. Forty-two Avalon 3C receiver stations were deployed in well 9 (Figure 3) with the shallowest receiver positioned 25 ft (7.6 m) below ground level and the remaining receiver stations spaced at vertical intervals of 50 ft (15.2 m) down to a depth of 2075 ft (632.5 m). Some of these 42 Avalon receiver stations were field-proven equipment provided by Halliburton and some were new, untested geophone packages provided by Avalon Sciences Ltd. Avalon engineers were onsite to monitor the performance of this mixture of older and newer geophone technology. The geophone array worked flawlessly.

Source-Receiver Test Geometries

Permanent walk-around and walk-away source-station patterns exist around well 9 on the Devine Test Site courtesy of U.S. Seismic Systems, Inc. (USSI), who tested new VSP receiver technology at the Devine site several times during 2014. A GPS coordinate map of these USSI source stations is displayed in Figure 3. EGL will attempt to keep these source stations permanently marked for future site users.

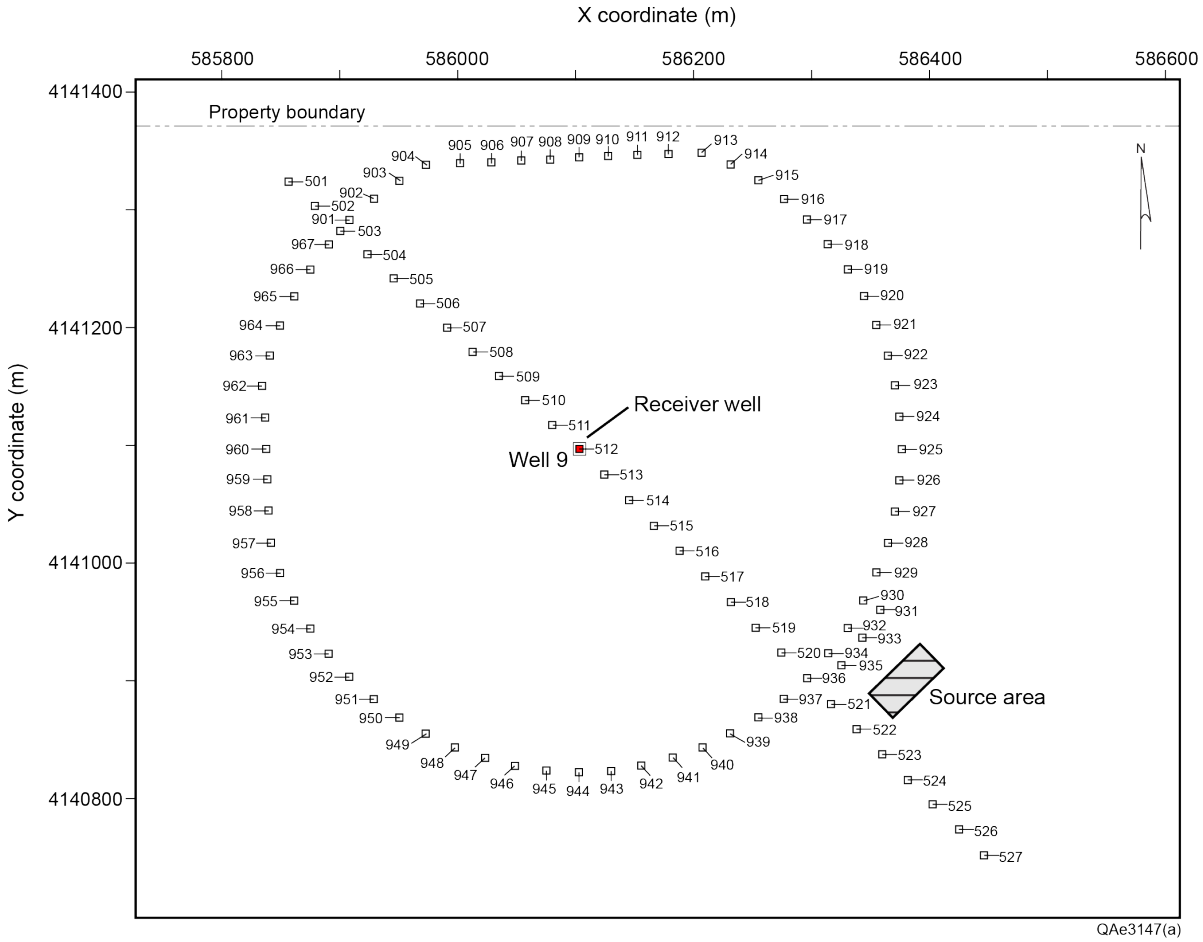

Figure 3. Walk-around and walk-away source stations established at test well 9, the receiver well used to record the source-array test data. The locations of the source-array patterns that were used in this field experiment are shown as the **Source area** labeled near the southeast intersection of the walk-around and walk-away source stations.

Heavy rainfall occurred on the Devine Test Site property immediately before our test program was initiated. Although it would have been useful to record data with vibrators positioned at several of these walk-around and walk-away source stations, that effort had to be abandoned because vibrators could not traverse several areas on the test-site property without becoming deeply mired in soft-surface areas. Thus test data were recorded only across source-

array test patterns positioned inside the rectangle labeled **Source area** at the southeast intersection of the walkaway and walk-around source stations in Figure 3.

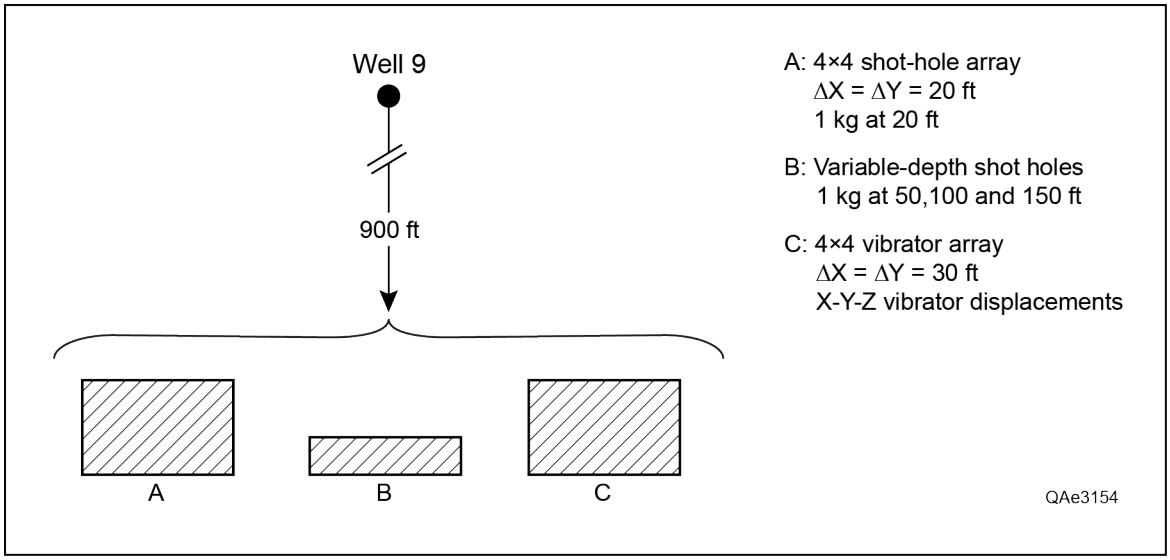

Figure 4. Zoom view of source-array test patches inside the **Source Area** shown in Figure 3.

A zoom view of the **source area** is shown in Figure 4. Three source-array patterns were constructed in close proximity inside these three source-test patches. One pattern (**A** in Figure 4) was an X-Y distribution of shot-holes, a second pattern (**B**) was a distribution of shot-holes drilled to various depths, and the third pattern (**C**) was an X-Y distribution of vibrator stations.

Details of explosive shot-hole patterns **A** and **B** are provided as Figure 5. X-Y test pattern **A** consisted of 16 shot-holes arranged in a 4 X 4 square, with shot stations spaced at intervals of 20 ft (6 m) in X and Y directions. All shot-holes in pattern area **A** were 20 ft (6 m) deep. Shot-holes C1 and C2 adjacent to pattern **A** (Figure 5) were calibration shots that were fired first to ensure the VSP data-acquisition system functioned properly.

Two identical sets of variable-depth shot-holes were constructed inside test-pattern area **B** (Figure 5) in case a data-recording error occurred when shooting one set of holes. The shot-holes in the first set of test shots are labeled 150A, 100A, and 50A, with the number indicating the depth of the explosive charge in the hole. The holes in the second set of test shots are labeled 150B and 100B. Shot-hole 100B had two separate charges: one at a depth of 100 ft and one at a depth of 50 ft. The depths of all explosive charges in these variable-depth shot-holes are identified in the table included in Figure 5.

The shot-hole drilling crew claimed that, even though the 1-kg explosive package they deployed is quite short, the shot depth was always 3 ft above the base of the shot-hole. The opinion of the driller about the depth of each explosive is used in the tabulated numbers listed in Figure 5. However, in calculations and discussions in this report, the depth of the explosive

shot will always be assumed to be 20, 50, 100, and 150 ft, the full depths of the shot-holes. As stated, shot-hole 100B (Figure 5) differed from all other shot-holes in that it was loaded with two explosives charges. One charge was at a depth of 100 ft (30 m), and one charge was at a depth of 50 ft (15 m). In this shot-hole, the deeper charge (at a depth of 100 ft) was shot first, and the shallower charge (at a depth of 50 ft) was shot last. The lithofacies descriptions listed in Figure 5 are based on comments and opinions of the shot-hole driller, not on cores or log data.

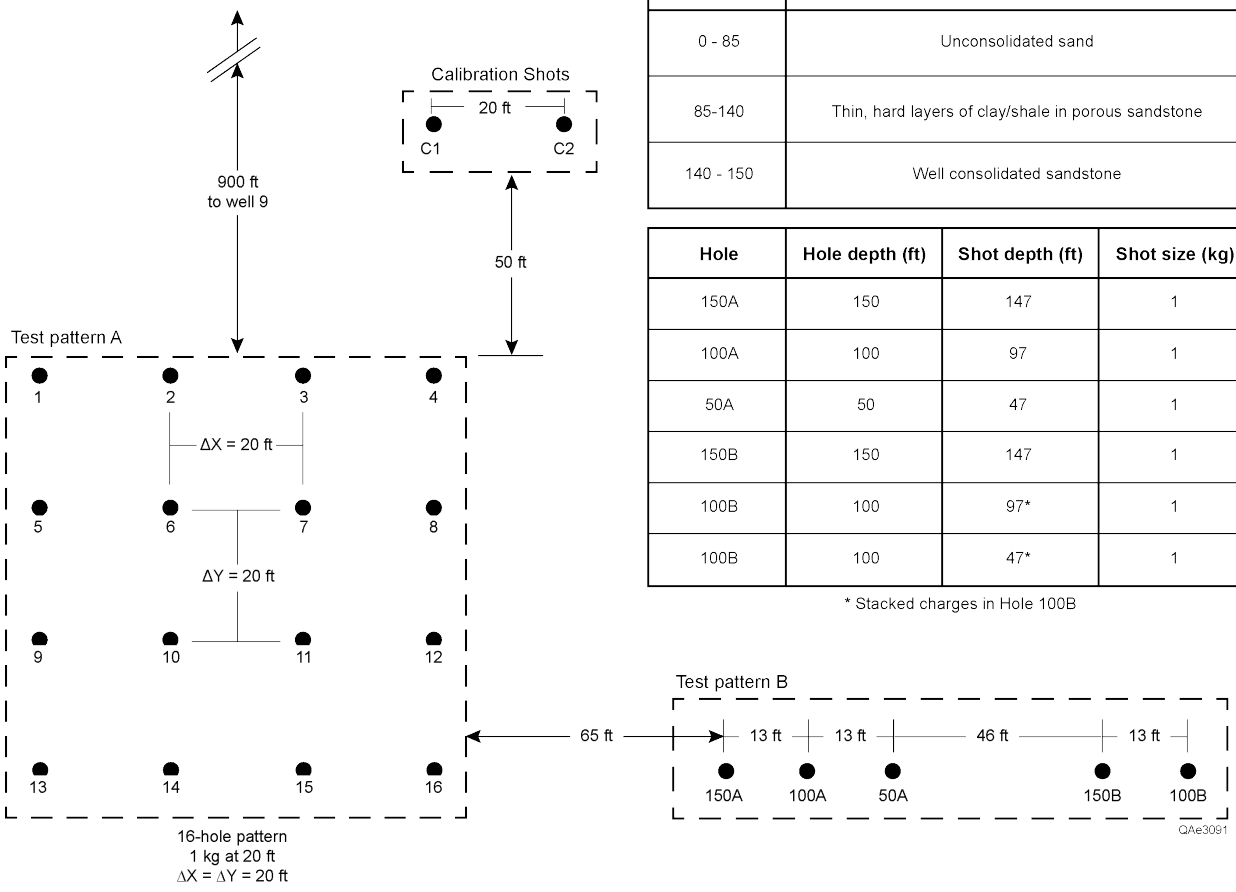

Depth (ft)	General Lithofacies
0 - 85	Unconsolidated sand
85-140	Thin, hard layers of clay/shale in porous sandstone
140 - 150	Well consolidated sandstone

Hole	Hole depth (ft)	Shot depth (ft)	Shot size (kg)
150A	150	147	1
100A	100	97	1
50A	50	47	1
150B	150	147	1
100B	100	97*	1
100B	100	47*	1

* Stacked charges in Hole 100B

Figure 5. Details of shot-hole test patterns **A** and **B**.

The details of vibrator source-array pattern **C** (Figure 4) are illustrated in Figure 6. This pattern was also a 4 X 4 square array of 16 source stations. However, these stations were spaced at intervals of 30 ft (9 m) in X and Y directions to replicate baseplate positions when vibrators are operated in the conventional field practice of being approximately bumper-to-bumper when used as array sources. When vertical-vibrator test data were collected, it did not matter how the vertical vibrator was oriented at a source station. A vertical vibrator could be oriented north, south, east, or west, and the illuminating wavefield would be identical for each orientation. However when horizontal-vibrator arrays were simulated, it was essential that

identical vibrator orientations be utilized at all source stations in order to create equal-polarity data in the illuminating wavefield produced at all source stations across the array area.

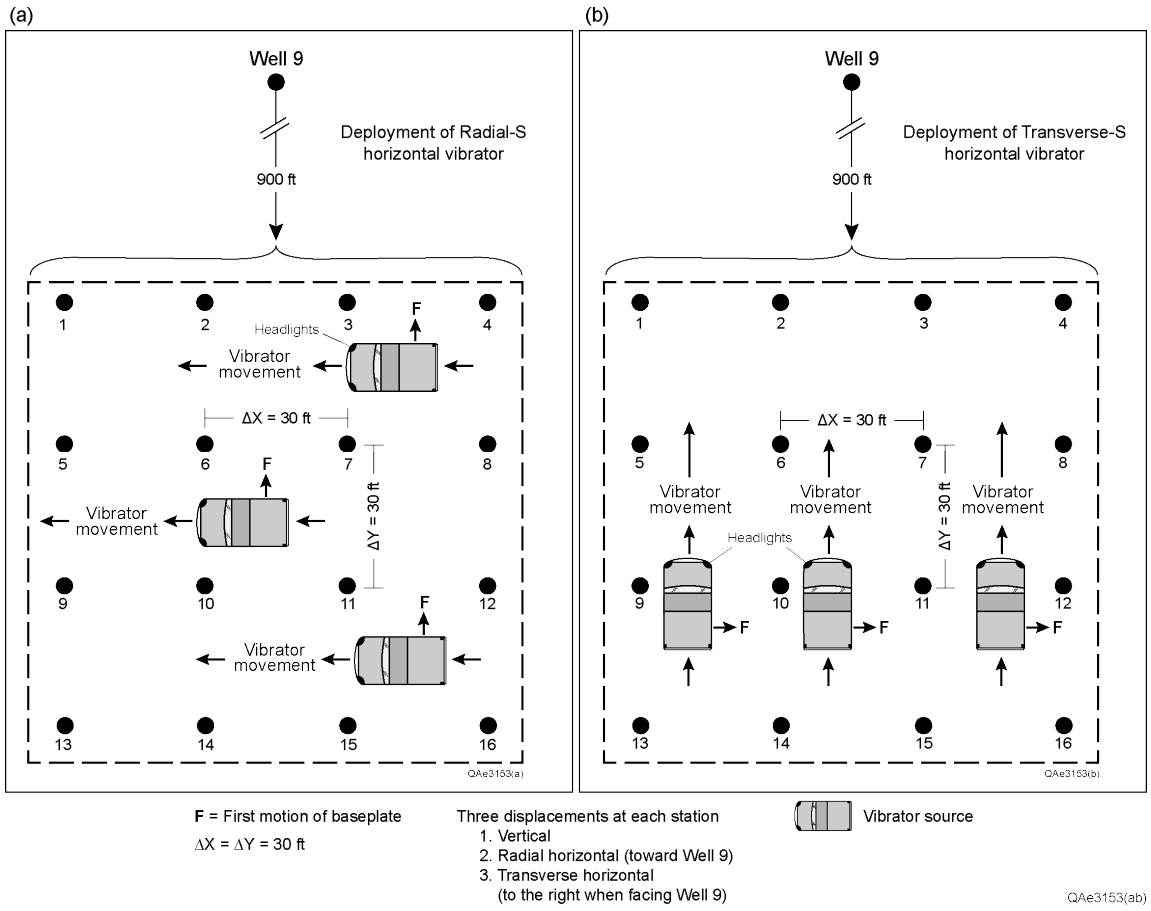

Figure 6. The 4 X 4 source pattern (patch **C** in Figure 4) used to record data generated by vertical and horizontal vibrators. The headlights of a vertical vibrator can be oriented in any azimuth direction at any of the 16 source stations. However, radial-horizontal vibrators must be oriented in the consistent azimuths defined in (a) at all 16 array stations, and transverse-horizontal vibrators must be oriented in the consistent azimuths defined in (b).

Data were recorded for two types of horizontal-vibrator arrays: (1) an array of radial-horizontal vibrators, and (2) an array of transverse-horizontal vibrators. For this test geometry, a radial-horizontal vibrator is defined as a vibrator that created a horizontal displacement that was oriented in the vertical plane that passes through the source station and the receiver well (well 9 in Figure 3). Each radial-horizontal vibrator was positioned so that the first motion of the baseplate (vector **F** in Figure 6a) was pointed toward the receiver well at each source station.

A transverse-horizontal vibrator will be defined as a vibrator that created a horizontal displacement that was oriented perpendicular to the vertical plane that passes through the source station and receiver well 9. Each transverse-horizontal vibrator was positioned so that the first motion of the baseplate (vector **F** in Figure 6b) was pointed toward the right as the

vibrator faced the receiver well at each source station. The movements of the single radial-horizontal vibrator as it traversed all 16 source stations of the 4 X 4 test pattern are illustrated in Figure 6a, and the movements of the single transverse-horizontal vibrator across the 16-station test patch are described in Figure 6b.

Primary and Secondary Direct-SV Modes Created by a Single Shot-Hole

This report focuses on direct-SV modes produced by seismic sources more than on direct-P modes produced by a source. Regarding explosive sources, EGL's claim is that a buried explosive creates a direct-SV wavefield at the exact position of the explosive charge in addition to the direct-P wavefield produced at that same position. The downgoing portion of this direct-SV wavefield will be called a **primary direct-S mode** (event **A** in Figure 7). The upgoing P and SV waves produced at the position of the buried explosion will reflect from the earth-air interface as time-delayed downgoing P and SV waves. These surface-converted SV waves will be called **secondary direct-S modes** (event **B** in Figure 7). The resulting direct-SV illuminating wavefield produced by a single buried explosive is the sum of primary direct-SV mode **A** and any secondary direct-SV modes **B** produced by mode conversion at the earth-air interface.

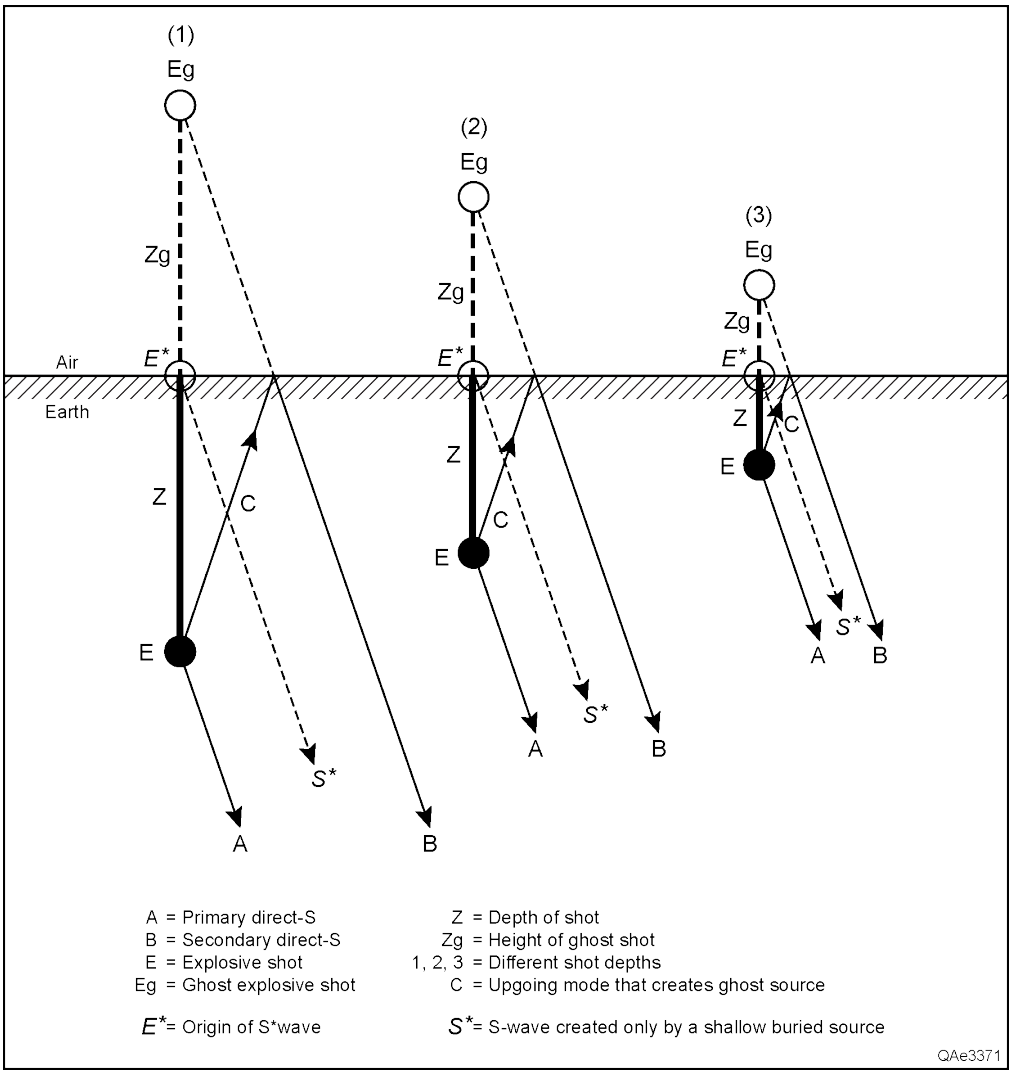

Figure 7. Primary and secondary direct-SV modes produced by a buried explosive. For simplicity, no P raypaths or P-wave modes are shown.

One objective of this source test was to record shot-hole explosive data that allowed the physics of primary and secondary SV modes generated by buried explosives to be documented and analyzed. These shot-hole test data also allowed EGL to determine if an odd S-wave called an **S*** ("**S-star**") wave could be identified (event **S*** in Figure 7). The physics of S* waves is discussed in **Appendix A** of this report. If an S* wave is present, then the downgoing SV wavefield that illuminates deep geology is the sum of S*, the primary direct-SV wave produced at the buried source, and all secondary converted-SV modes produced at the free surface.

The raypaths associated with primary and secondary direct-SV modes produced by a buried explosive shot are illustrated in Figure 7. Although a buried explosive also creates upgoing and downgoing P-wave modes, no P-wave raypaths are included in this diagram because the intent is to understand the physics of direct-SV wavefields. Also included in the figure are a raypath for the S* wave, if that wave mode exists, and the source coordinate E* where this S* wave should be created.

The time delay between a primary direct-SV mode **A** and its associated secondary direct-SV mode **B** (Figure 7) depends on the depth of the shot and what type of upgoing wavefield **C** creates the secondary direct-SV mode. Upgoing raypath **C** can be traveled by either a P wave or an SV wave, which introduces the concept that there can be two secondary downgoing P events and two secondary downgoing SV events. One secondary P event and one secondary SV event are created by the upgoing P wave at the free surface, and one secondary P event and one secondary SV event are created by the upgoing SV wave.

In contrast to this dual secondary-event concept, S* waves are based on the assumption that "only an upgoing P wave from a shallow buried source" can create a downgoing S* wave at the free surface. References to published papers where this assumption is discussed are provided in Appendix A. A second oddity of S* physics is that the secondary S* source is positioned on the earth surface directly above the buried source, not above the free surface as are ghost sources Eg in Figure 7. Because P-SV reflectivity is zero for the normal-incidence travel path from E to E*, an S* event is called a non-geometric wave, meaning it is a wave that does not conform to the raypath geometry required by Snell's law or to standard rules of wavefield reflectivity and mode conversion. Thus rather than being produced by a reflected wavefield, an S* wave is assumed to be generated when an up-going P-wave creates a short-radius bulge in the free surface. This bulge, in turn, causes a shear displacement to be generated at coordinate E*. This logic explains why a P source has to be close to the surface to produce an S* wave (Gutowski, et al., 1984).

The variable-depth shot holes labeled **Test pattern B** in the lower right of Figure 5 were used to generate data for investigating primary direct-SV and secondary direct-SV modes produced by a buried explosive. The data in Figure 8 show downgoing direct-SV wavefields generated by explosive shots at different depths. These data were recorded by the 42-station array of 3C geophones deployed in well 9 (Figure 3). These geophones were mathematically rotated so that a consistent geophone at each receiver station was oriented to record downgoing P modes traveling in the vertical plane passing through the source station and the

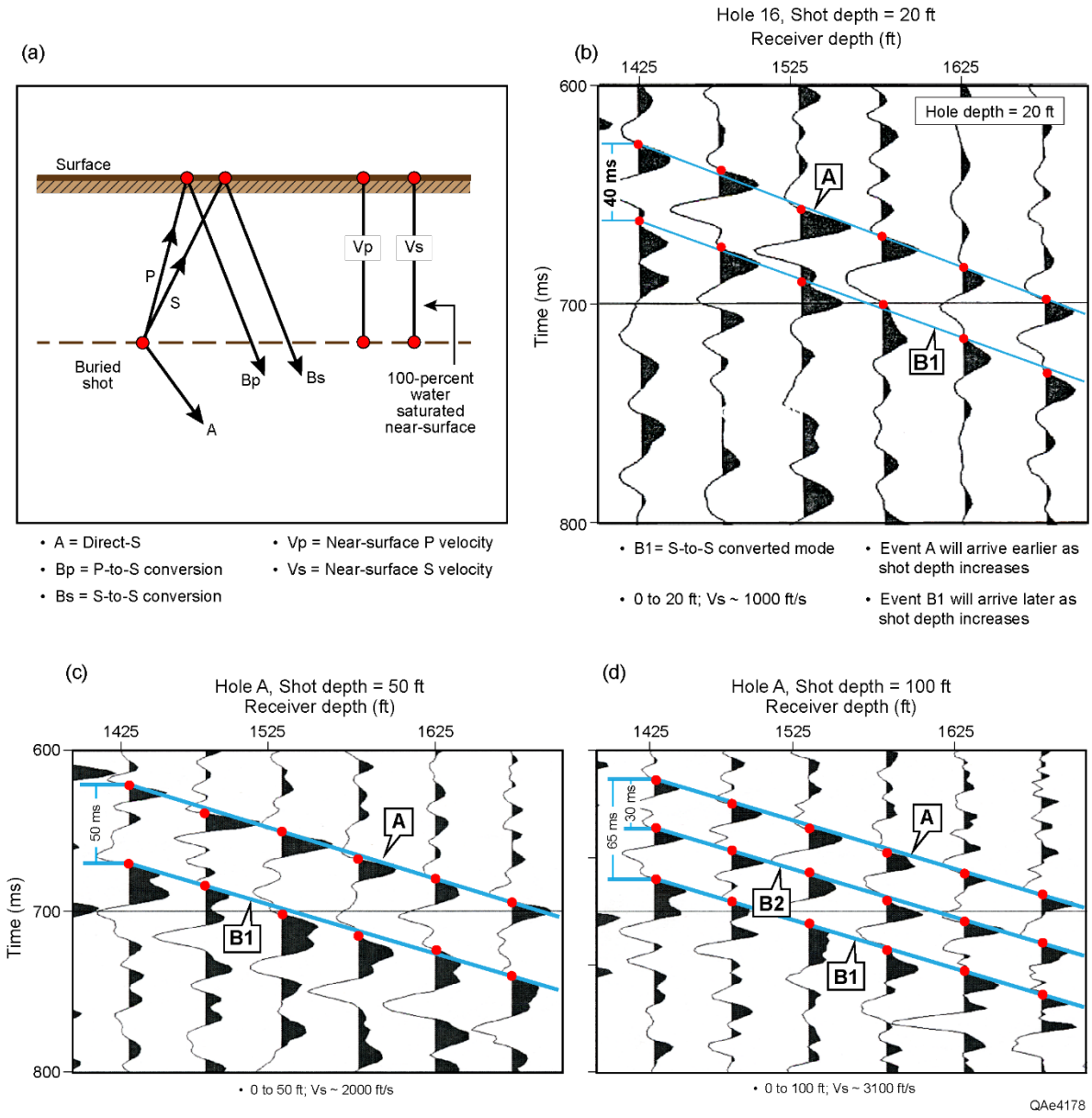

Figure 8. Primary direct-SR and secondary direct-SR modes produced by a buried explosive. (a) Diagram showing a buried explosive source and the S modes that it creates. The downhole receivers are radial geophones oriented to record downgoing SR shear waves. (b) Real-data SR modes observed when the shot depth is 20 ft. (c) Real-data SR modes observed when the shot depth is 50 ft. (d) Real-data SR modes when the shot depth is 100 ft.

receiver station, a second consistent geophone was oriented to record downgoing modes that generated **SR** (radial S) displacements oriented in this same vertical plane, and the third receiver was oriented to record **ST** (transverse S) displacements that were perpendicular to this vertical source-to-receiver plane. The data in Figure 8 represent responses of six consecutive receiver stations spanning a depth interval 1425 to 1675 ft where data recorded by rotated

geophones had optimal quality for wave mode analysis. The time window used in the data displays focuses on the downgoing direct-SR modes that were generated because the data were recorded by SR-displacement geophones oriented in the vertical source-receiver plane.

The diagram in Figure 8a illustrates the buried source environment. It is important to note that this test was done immediately after a significant amount of rain fell on the Devine Test Site. Thus porous near-surface layers across the area were fully water saturated, which results in the V_P velocity in shallow layers never being significantly slower than V_P velocity in water. The data in Figure 8b were generated by an explosive positioned at a depth of 20 ft in shot-hole16 of **Test pattern A** which was offset 65 ft from shot-hole 150A of **Test pattern B** where deeper charges were deployed (Figure 5). The receivers that recorded the data across depth interval 1425 ft to 1675 ft were geophones that were oriented in the vertical plane passing through each explosive shot and each receiver station and then tilted so that they responded to radial S-wave displacement confined to that vertical plane.

Labels **A** and **B** in Figure 7 that define primary and secondary SV modes will be used to designate primary direct-SV and secondary direct-SV modes in these real-data examples. For example, in Figure 8a, event **A** is the downgoing primary direct-SV event labeled **A** in Figure 7 that is produced at the shot depth, and events $\mathbf{B_P}$ and $\mathbf{B_S}$ are components of the converted-SV event labeled **B** (Figure 7) that is generated at the earth-air interface. The concept of event **B** is expanded in Figure 8a to indicate that when analyzing real data, an interpreter must assume there may be two possible downgoing surface-converted modes – a mode $\mathbf{B_P}$ created by the upgoing P mode from the shot and a mode $\mathbf{B_S}$ created by the upgoing SV mode from the shot.

The data in Figures 8b, 8c, and 8d show the direct-SV illumination that results when the shot depth is successively increased from 20 ft, to 50 ft, and then to 100 ft. Several principles of direct-SV illumination with buried explosives are inferred by these data.

1. There is conclusive proof that real-data event **A** is an SV mode generated directly at the shot depth. As shot depth increases, any direct-SV mode produced at the position of a buried charge will move to earlier arrival times for a fix downhole receiver because the source-to-receiver distance is reduced as shot depth increases. That decreasing arrival time behavior is exactly what is observed for event **A**, with **A** arrival time in Figure 8c (shot depth = 50 ft) reduced by approximately 4 ms (from 628 ms to 624 ms at receiver depth 1425 ft) compared to Figure 8b (where shot depth is 20 ft), and then reduced by an additional 5 ms in Figure 8d (from 624 ms to 619 ms at receiver depth 1425 ft) as shot depth increases to 100 ft. This decreasing arrival time of event **A** with increasing shot depth is also well demonstrated by examining the positions of the **A** wavelet at receiver depth 1675 ft relative to the 700-ms timing line labeled in Figures 8b, 8c, and 8d. An interpreter must conclude that these examples are real-data evidence that a buried explosive generates a primary direct-SV mode exactly at the position of the buried charge. Thus illuminating direct-SV wavefields generated by a buried explosive cannot be explained as being only converted-SV modes produced at the earth-air interface as some geophysicists claim.

2. There is compelling evidence that robust secondary direct-SV modes are produced at the earth-air interface above a buried shot. In contrast to the primary direct-SV mode **A**, a surface-converted mode moves to later arrival times, not to earlier times, as shot depth increases because the travel path from shot to surface lengthens as shot depth increases. For example, note that event **B1** in Figure 8c moves to later arrival times for a shot depth of 50 ft (where **B1** is approximately 50 ms later than event **A**) compared to where mode **B1** appears occurs when the shot depth is 20-ft (Figure 8b, where **B1** is approximately 40ms later than event **A**), and then moves to even later arrival times in Figure 8d when shot depth increases to 100 ft (where **B1** is approximately 65 ms later than event **A**).

3. Contrary to the popular assumption that secondary direct-SV modes are produced by P-to-SV conversion at the earth surface, the secondary direct-SV mode produced in these test data are produced by an upgoing SV mode, not by an upgoing P mode. Specifically, the 40-ms delay between events **A** and **B1** in Figure 8b implies that mode **B1** is mode $\mathbf{B_S}$ of Figure 8a created by the upgoing direct-SV from the shot. If converted-mode **B1** was produced by the upgoing P from the shot, then a V_P of approximately 5000 ft/s that is required for fully saturated near-surface layers would result in a time delay of only 4 ms for the upgoing P to traverse the 20-ft distance to the surface. This short travel time would then require the average V_S velocity across the top 20 ft of the earth to be no faster than 550 ft/s in order to create the required 36 ms of travel-time delay on the downward path. A V_S velocity as slow as 550 ft/s across the top 20-ft of strata at the Devine Test Site is not realistic. However, if it is assumed that secondary direct-S mode **B1** is created by the upgoing SV from the shot, then the average V_S velocity in the top 20 ft of the near-surface needs to be approximately 1000 ft/s to satisfy the real-data time delay of 40 ms, which is a more realistic V_S velocity assumption for shallow strata across the Devine Test Site. Event **B1** in Figure 8c is this same SV-to-SV converted mode **B1** when the shot depth increases to 50 ft. The time delay (50 ms) between **A** and **B1** for a 50-ft shot depth implies the average V_S velocity in the top 50 ft of the near surface is approximately 2000 ft/s, which is also a reasonable value. When the shot-depth increases to 100 ft (Figure 8d), the time delay of 65 ms between primary direct-SV mode **A** and secondary direct-SV event **B1** indicates B1 is a converted SV-SV mode generated at the earth surface that propagates with an average V_S velocity of 3100 ft/s.

4. Secondary direct-SV modes can be created at interfaces other than the earth-air interface. An example is event **B2** in Figure 8d. No combination of realistic near-surface V_P and V_S velocities allow this event to be a converted-SV mode generated at the earth surface by an upgoing SV or an upgoing P. The 30-ms time delay between **B2** and primary direct-SV event **A** does not allow even a one-way SV travel time when V_S = 3100 ft/s as SV-SV mode **B1** implies is the average V_S velocity would be at that depth. Thus event **B2** was created at some interface closer to the shot that the earth surface. The shot-hole drilling crew stated this shot hole differed from other shot holes they drilled across the test pattern in that it encountered a hard sandstone layer about

2 ft thick at a significant depth, but they did not document the depth of this sandstone. For the time being, event **B2** is assumed to be related to an interface associated with this unknown hard-sandstone interval.

In summary, these variable-depth explosive shots confirm that the illuminating SV wavefield produced by a buried explosive consists of: (1) a primary direct-SV that originates directly at the position of the buried shot, (2) a SV-to-SV converted mode (a secondary direct-SV mode) produced at the earth surface, and (3) possible converted modes created at unknown subsurface surfaces. There is no obvious evidence of an S* mode. However, it is possible that the mysterious S* mode discussed in Appendix A could be present but is camouflaged by secondary direct-SV modes **B1** and **B2**.

Simulating Source Arrays and Measuring Intra-Array Source Statics

The fundamental purpose of this source test was to collect data that would indicate how direct-P and direct-SV illuminating wavefields produced by a point source are modified when two or more point sources are operated as an array source. This comparison between point-source illumination and array-source illumination is of particular interest when considering the possibility of extracting SV-P data from legacy P-wave data. Most legacy P-wave data will be recorded with array sources, particularly if the energy sources are vertical vibrators. Thus it is necessary to get a sense of how direct-SV illumination produced by an array of vertical-displacement sources differs from the direct-SV illumination produced by only one point-source within that array.

The basic concept that will be evaluated is illustrated in Figure 1. Although both direct-P and direct-SV intra-array source statics will be evaluated, it is the behavior of SV statics within the area covered by an array source that will be of particular interest. This analysis will consider shot-hole arrays first and then expand to consider arrays of vertical and horizontal vibrators. For each set of source data, the analysis is limited to displays of illuminating wavelets that allow readers to visually see effects of intra-array statics on wavelet origin time and to compare variations in wavelet waveshapes for point sources and array sources.

Direct-P and Direct-SV Modes Produced by Single and Arrayed Shot-Holes

The data used to compare direct-P and direct-SV illuminating wavefields generated by buried explosives were collected across test patch **A** shown in Figures 4 and 5. All shot-holes inside this array were 20-ft (6-m) deep and were loaded with a 1-kg charge.

Direct-P Modes Produced by Point-Source Explosives

Figure 9 shows the direct-P wavelets generated at each shot-hole across test patch **A** and recorded with a properly rotated 3C geophone at a depth of 1525 ft in well 9. This source-receiver geometry provides true body-wave illuminating wavelets that image deep geology. Shot-hole stations are identified by the circled number at the top of each wavelet panel. These numbers are listed in the same row and column sequence order as the station numbers shown in test pattern **A** in Figure 5. The wavelet generated at source station 11 is arbitrarily chosen as a reference wavelet that represents the direct-P illumination wavelet that should be produced by each buried-explosive point source within the test patch. This wavelet is labeled **Reference** in Figure 9 to aid in wavelet comparisons across the test patch. The arrival time of a selected phase point on this direct-P reference wavelet is shown as the dashed line that traverses each horizontal rack of source-station wavelets. The interpreted arrival time of this wavelet phase for each direct-P arrival is shown by the arrow placed on each time-shifted wavelet. The time shift (in ms) of this phase point between each station wavelet and reference wavelet 11 is written in the rectangular box on each wavelet panel. This time shift indicates the effects of intra-array statics.

Visual inspection of Figure 9 shows that all 16 direct-P wavelets produced across shot-hole pattern **A** have a consistent waveshape. The illuminating P wavelets differ only in small static time delays of 4-ms or less. Because it is important for a seismic source to produce a consistent-shape illuminating wavelet across a study area, a single buried explosive is an excellent choice for a seismic source to use for P-wave imaging.

Direct-P Modes Produced by Arrays of Shot Holes

Examination of the static time shifts posted on Figure 9 shows that shot-hole pattern **A** segregates into two P-static domains that will be referred to as **D1** and **D2**. Static domain **D1** is the half-space of pattern **A** where shot-holes 1 through 8 are positioned. All P statics in domain **D1** are positive with values ranging from +2ms to +4ms (Figure 9). Static domain **D2** is the half-space containing shot-holes 9 through 16. In contrast to domain **D1**, all P statics in domain **D2** are zero or have negative values as large as -3ms (with the exception of the +1ms static at shot-hole 10). Although these static time shifts are not large, they are distinctive in that the static shifts in domains **D1** and **D2** differ in algebraic signs.

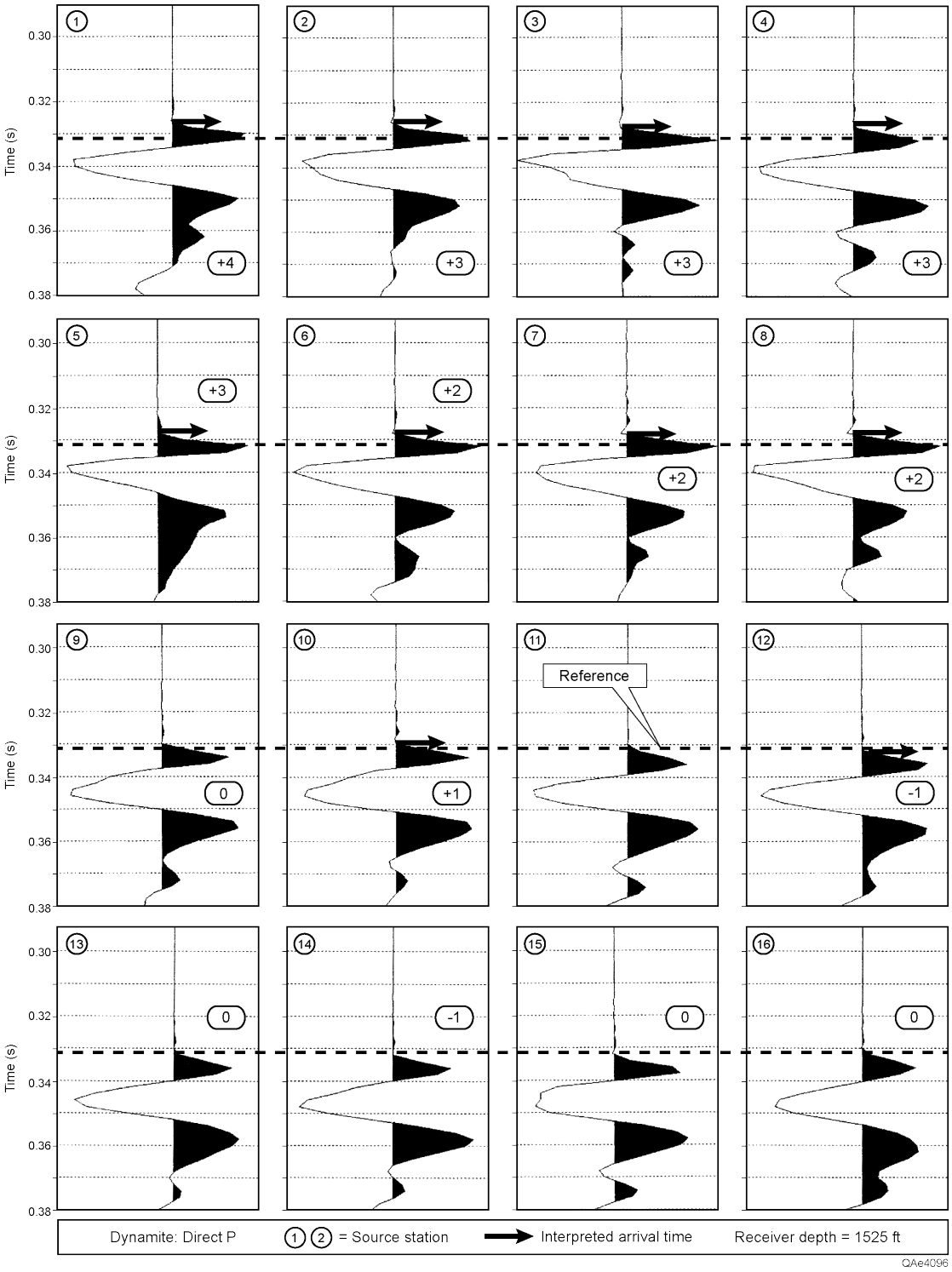

Figure 9. Direct-P mode produced by a buried explosive at each of the 16 test shot-holes in test patch **A**. The wavelet generated at station 11 is used as a **Reference**. The arrival time of this reference-wavelet phase is shown as the dash line that traverses each horizontal rack of wavelets. The interpreted arrival time of this phase is shown by an arrow on time-shifted wavelets. The time shift (in ms) between each wavelet and reference wavelet 11 is written in the box on each wavelet panel.

Source arrays composed of 2, 3, or 4 shot-holes would yield an illuminating P wavelet equivalent to a point-source P wavelet if all shot-holes in the array were confined to domain **D1** (shot-holes 1 to 8) where P statics at adjacent shot-holes differ by only 1 ms. However, if the shot-holes extended into both domains **D1** and **D2**, adjacent shot-hole P statics could be as large as 5 ms (shot-holes 8 and 12 for example). The summation of two wavelets shifted by 5 ms may result in a composite waveshape that differs more than desired from the waveshape of the point-source P wavelet produced at either shot-hole.

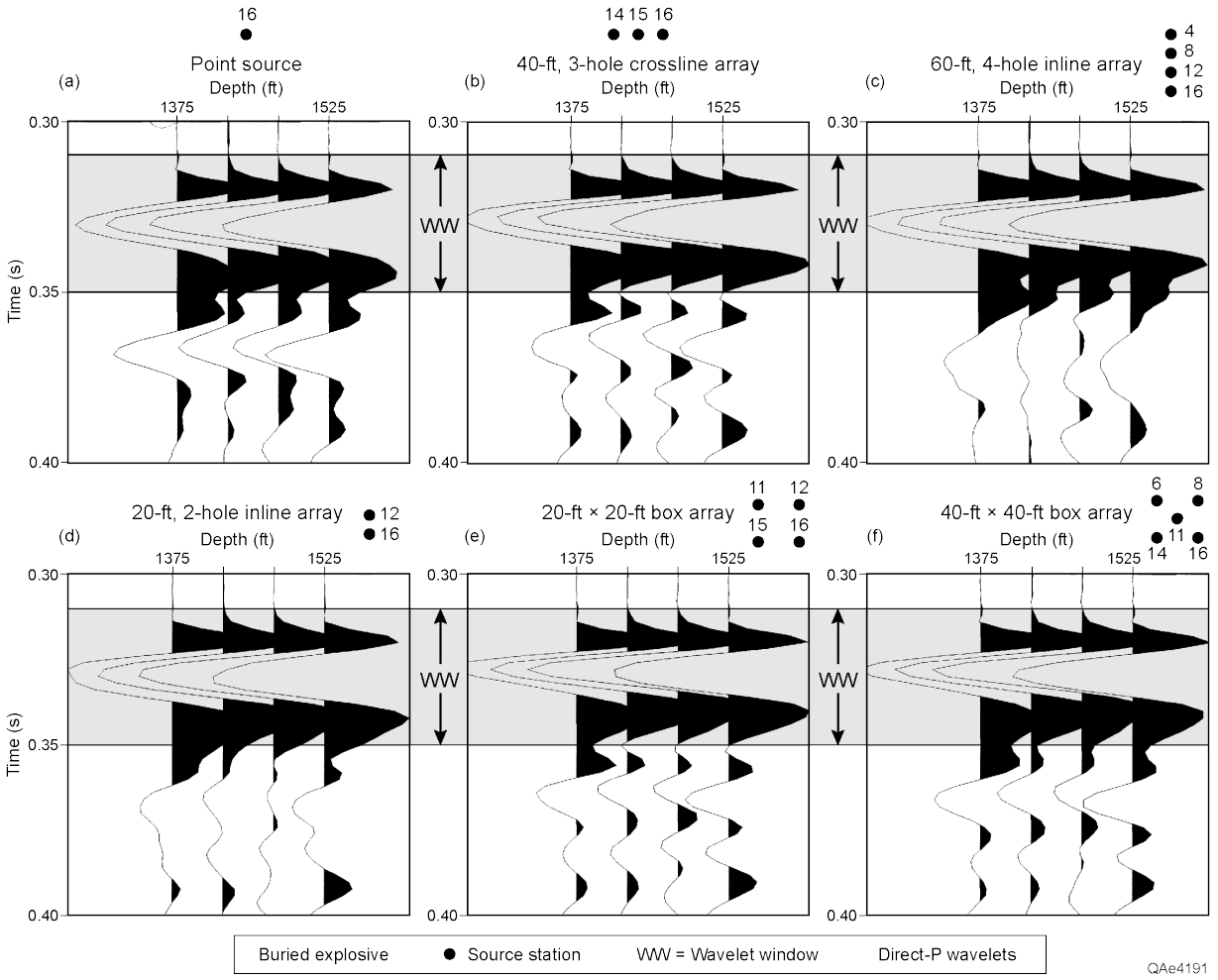

Figure 10. Direct-P modes produced by (a) a single shot at station 16 and by arbitrary arrays of shot holes (b through f). The numbered dots refer to specific shot-holes identified in Figure 5. **WW** is the wavelet window.

Examples of the variations in direct-P illuminating wavelets that can be produced by different arrays of shot-holes inside test area **A** are shown in Figure 10. Each dot in the dot pattern accompanying each data panel is a specific shot-hole, and the number beside a dot identifies which shot-hole in test patch **A** (Figure 5) is utilized. These examples compare the

direct-P wavelet generated by a point-source explosion (Figure 10a) with direct-P wavelets generated by various arrays of shot holes (Figures 10b through 10f). The depths of the receiver stations where the illuminating wavelets produced by each source array were recorded are labeled across the top of each data panel. There are only minor differences in the principal-energy portions of these six sets of illuminating wavelets, which indicates that, at this site, buried explosives are a good P-wave source regardless of whether the source is a single shot-hole or an array of shot-holes.

Direct-SR Modes Produced by Point-Source Explosives

For these test data, a direct-SR mode is defined as the direct-S response generated by a test source and recorded by a rotated sensor positioned in the vertical plane that passes through the source station and the receiver station. The direct-SR wavelets generated at each source station within shot-hole pattern **A** and recorded with a properly rotated 3C geophone at a depth of 1525 ft in well 9 are displayed as Figure 11. Shot-hole stations are identified by the circled number on each wavelet panel. These station numbers are arranged in the same order as the station numbers shown in test pattern **A** in Figure 5. The illuminating SR wavelet generated at source station 11 is used as a reference wavelet to represent the direct-SR illumination wavelet that should be produced by each buried-explosive across the test patch. This wavelet is labeled **Reference** in Figure 11. The arrival time of a selected phase point on this reference wavelet is shown as the dash line that traverses each horizontal rack of four source-station wavelets. The interpreted arrival time of this phase point for each time-shifted wavelet is shown by a bold arrow. The time shift (in ms) of this phase point between each wavelet and the **Reference** wavelet is written in the box on each wavelet panel.

With the exception of the direct-SR wavelet produced at shot-holes 1 through 4, all of the direct-SR modes have a reasonably consistent waveshape. Examination of the static time shifts posted on Figure 11 shows that shot-hole pattern **A** segregates into two SR-static domains that will be referred to as **D1** and **D2**. These two SR-static domains are the same as the two P-static domains identified when discussing Figure 9. SR-static domain **D1** is the half-space of pattern **A** where shot-holes 1 through 8 are positioned. All SR statics in domain **D1** are positive with values ranging from +5 ms to +12 ms. SR-static domain **D2** is the half space containing shot-holes 9 through 16. In contrast to domain **D1**, all SR statics in domain **D2** are zero or “almost” zero. The SR static values in these two domains are distinctive in that they not only differ both in algebraic sign but have significantly different magnitudes.

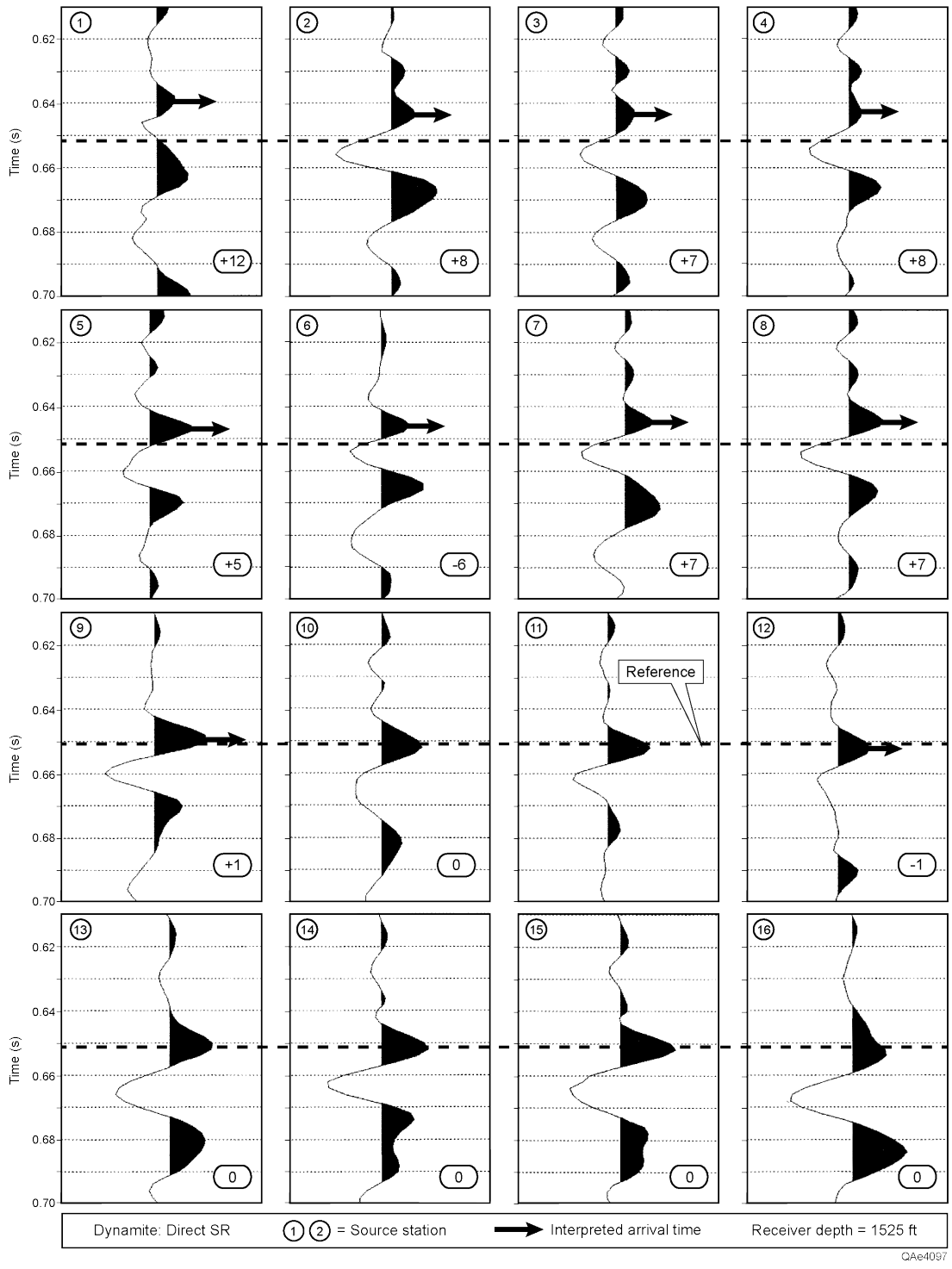

Figure 11. Direct-SR wavelets produced by a buried explosive at each of the 16 shot-holes across source array **A**. The wavelet generated at station 11 is used as a **Reference** wavelet. A black-peak phase point on this **Reference** wavelet is selected as a time reference (dashed line). The arrival time of this phase point is indicated by an arrow on time-shifted wavelets. The time shift (in ms) of this phase point between each wavelet and the **Reference** wavelet is written in the box on each panel.

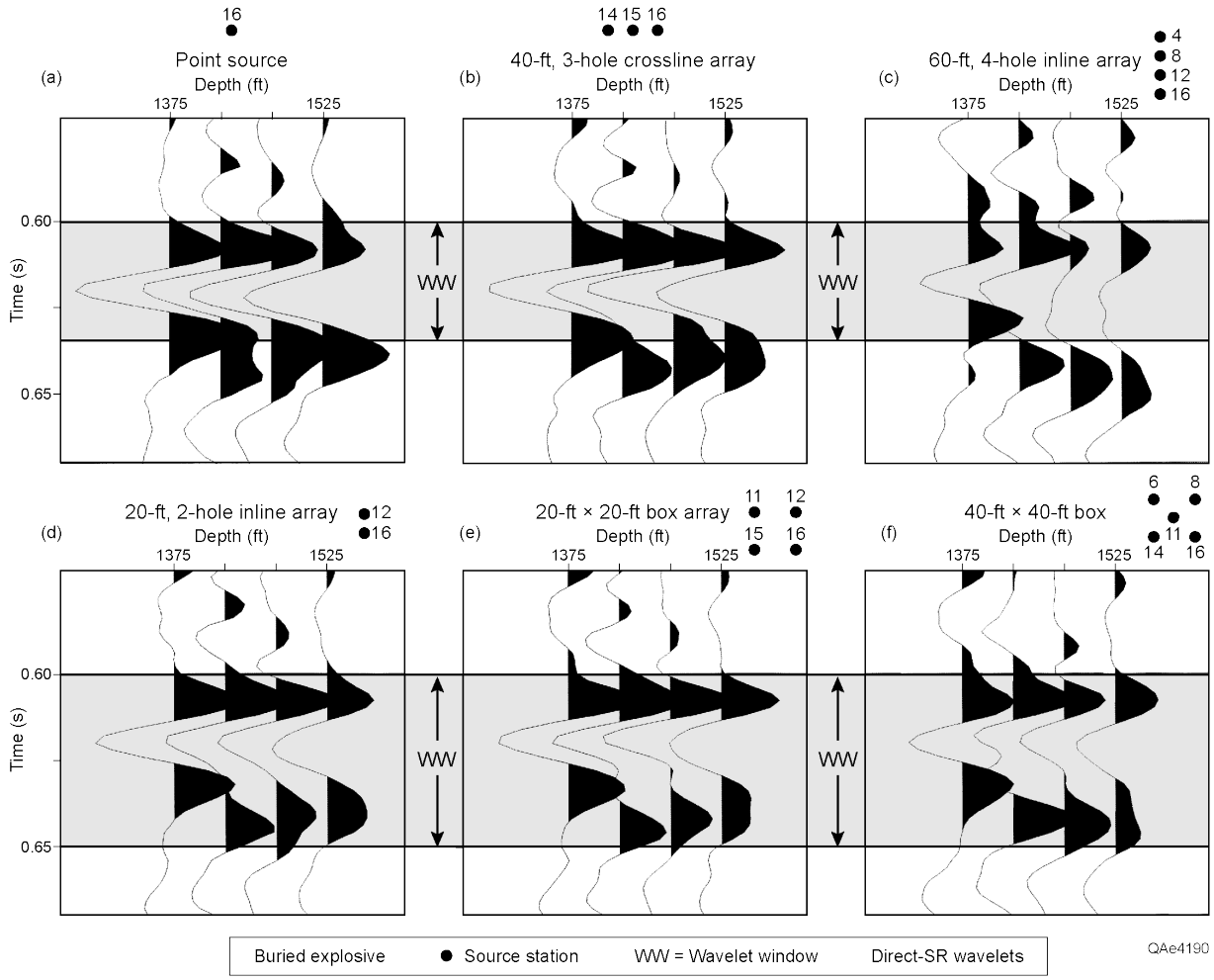

Figure 12. Direct-SR modes produced by (a) a single shot at station 16 and by selected shot-hole arrays (b through f). Numbered dots correspond to number shot-holes in Figure 5. **WW** is the wavelet window.

Direct-SR Modes Produced by Arrays of Shot Holes

Illuminating SR wavelets produced by source arrays of 2, 3, or 4 shot-holes can have a wide range of waveshapes depending on where the shot-hole pattern is located within test patch **A**. Examples of the variations in direct-SR illuminating wavelets that can be produced by different arrays of shot-holes are shown in Figure 12. These examples compare direct-SR wavelets generated by a point-source explosion (Figure 12a) with direct-SR wavelets generated by the same shot-hole arrays used in Figure 10. The specific shot-holes that form each source array are identified by the numbered dot pattern accompanying each data panel. The number beside each dot identifies which shot-hole in patch **A** is used to create each shot-hole array. The depths of the receiver stations where the illuminating wavelets produced by each source were recorded (1375 ft to 1525 ft) are labeled at the top of each data panel. There are only minor differences in the principal-energy portions of point-source wavelets (Figure 12a) and large-

array wavelets when all shot-holes in the array are confined to static domain **D2** (Figure 12b). However, if an array involves shot-holes in SR-static domains **D1** and **D2**, then the illuminating wavelet becomes more distorted than desired (Figure 12c). An important principal exhibited by these wavelet comparisons is that a single buried-explosive, not arrays of buried explosives, are preferred for S-wave imaging of geologic targets. Intra-array S statics can definitely cause sub-optimal illuminating direct-SR wavelets to be produced by shot-hole arrays.

Direct-ST Modes Produced by Point-Source Explosives

In this source test, a direct-ST mode is defined as the direct-SV response recorded by a 3C VSP sensor that is positioned perpendicular to the vertical plane passing through a source station and a receiver station. The direct-ST wavelets generated at each shot-hole and recorded with a properly rotated 3C geophone at a depth of 1575 ft in well 9 are displayed as Figure 13. Shot-hole stations are identified by the circled number on each wavelet panel and are shown in the same sequential order as the station numbers identified across test pattern **A** in Figure 5. The illuminating ST wavelet generated at source station 11 is used as a **Reference** to represent the direct-ST mode produced by each buried-explosive charge in the test array. The arrival time associated with a selected phase (the apex of the black wavelet peak at station 11) of this **Reference** wavelet is shown as a dash line that traverses each horizontal rack of four source stations. The interpreted arrival time of this selected wavelet phase for each shot is shown by the arrow added to each wavelet. The time shift (in ms) of this phase point between each wavelet and **reference** wavelet 11 is written in the square box on each wavelet panel.

With the exception of the direct-ST illumination produced at shot-holes 1, 4, and 12, all of the direct-ST wavelets have a reasonably consistent waveshape. Note the intra-array ST-source statics are different than the intra-array SR-wave statics in Figure 11; with the differences in SR-static and ST statics at the 16 source stations differing by less than ±5 ms except for the wavelet generated at station 12. The ST statics segregate the shot-hole test patch into the same two static domains **D1** and **D2** shown by the P-wave statics in Figure 9 and by the SR statics in Figure 11. In the half-space of the test patch occupied by shot-holes 1 through 8, the ST source static is always positive. In contrast, across the half-space spanning shot-holes 9 through 16, the ST source static is negative, except for a small positive static at source station 10.

The fact that almost all direct-ST wavelets have a consistent waveshape again implies a single shot-hole explosive is a good source to use for S-wave reflection seismology. The significant ST statics across test pattern **A** indicate arrays of shot-holes should be avoided if possible when the objective is to utilize SV-P data or any S-wave mode produced by a buried-explosive.

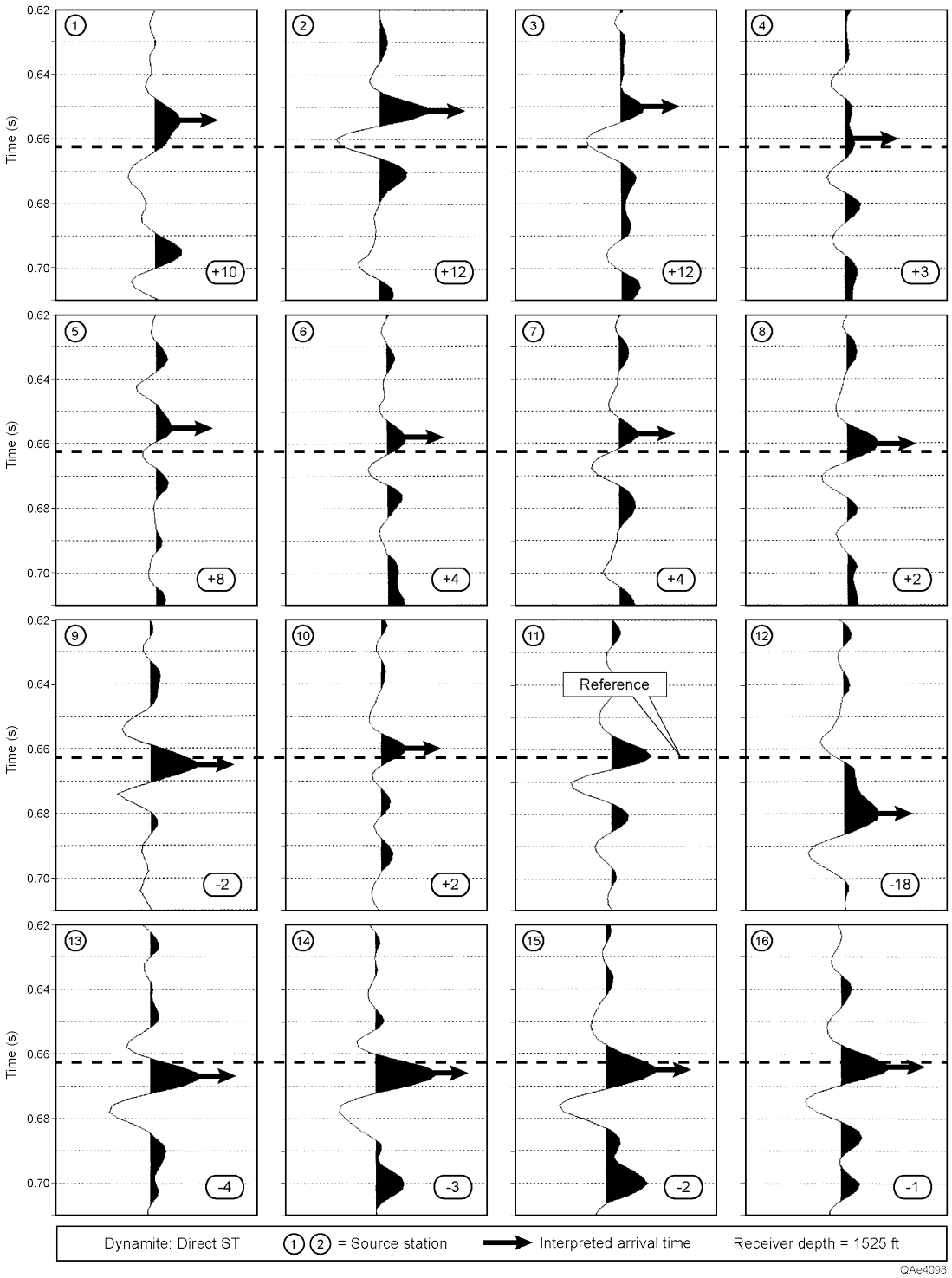

Figure 13. Direct-ST wavelets produced by a buried explosive at each test hole. The wavelet generated at station 11 is used as a **Reference**. A black peak on this wavelet is selected as a time reference. The arrival time of this phase point is marked on each wavelet as a tic bold arrow. The time coordinate of the **Reference** point is shown by the dash line. The time shift (in ms) of this phase point between each wavelet and the **Reference** wavelet is written in the box on each wavelet panel.

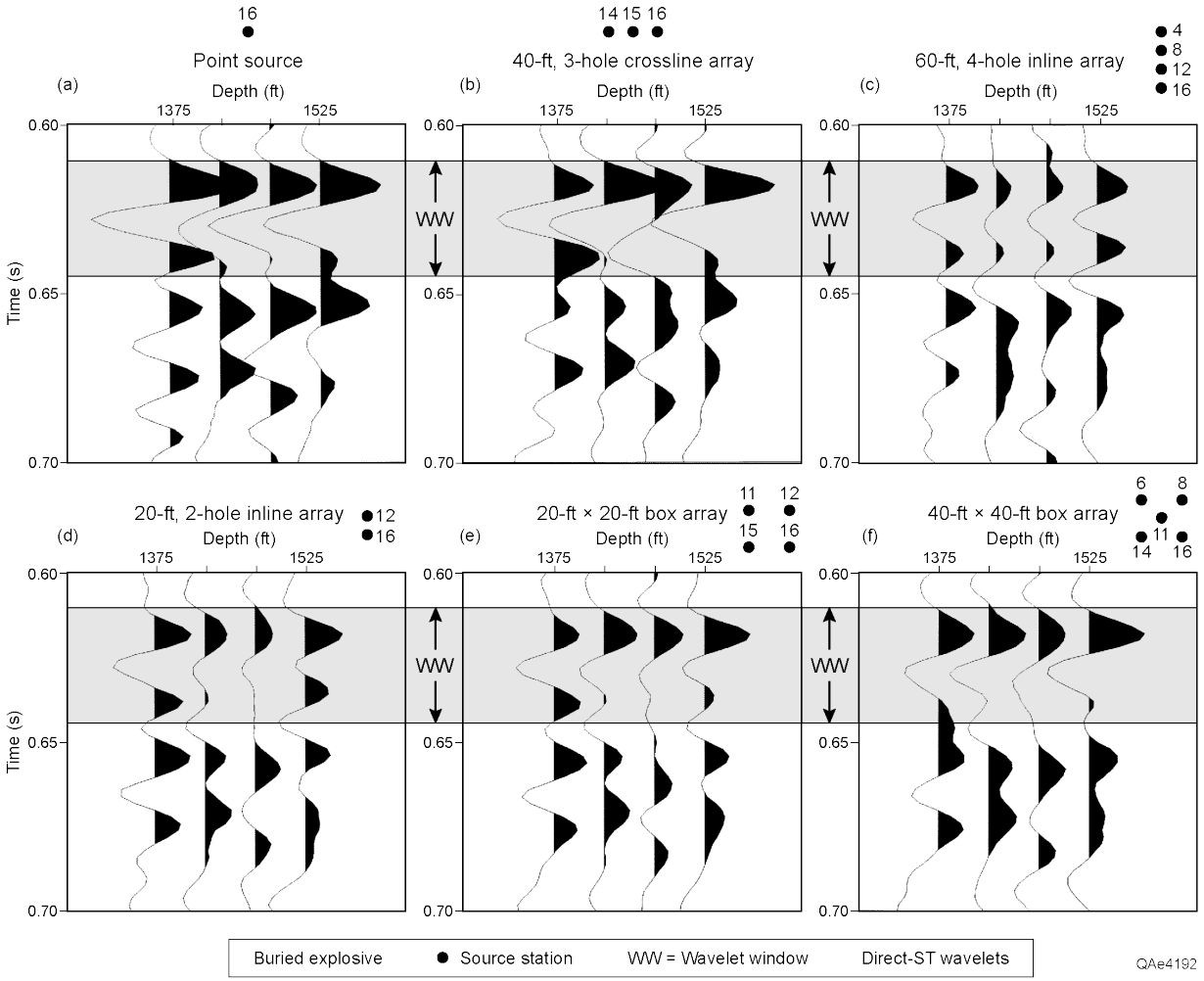

Figure 14. Direct-ST modes produced by (a) a single shot at station 16 and by shot-hole arrays of various sizes and geometries (b through f). Each numbered dot corresponds to the same numbered shot-hole in Figure 5. **WW** is the wavelet window.

Direct-ST Modes Produced by Arrays of Shot Holes

Examples of the variations in direct-ST illuminating wavelets that can be produced by different arrays of shot-holes inside test area **A** are shown in Figure 14. These examples compare direct-ST wavelets generated by a point-source explosion (Figure 14a) with direct-ST wavelets generated by shot-hole arrays (Figures 14b through 14f). The specific shot-holes that form each source array are identified by the numbered dot pattern above each data panel. Each numbered dot corresponds to the same numbered shot-hole in Figure 5. The depths of the receiver stations where the illuminating wavelets produced by each source were recorded

(1375 ft to 1525 ft) are also labeled on each data panel. There are only minor differences in the principal-energy portions of point-source wavelets (Figure 14a) and large-array wavelets when all shot-holes in the array are confined to ST static domain **D2** (Figure 14b). However, if an array involves shot-holes in ST-static domains **D1** and **D2**, then the illuminating wavelet becomes more distorted than desired (Figure 14c). An important principal exhibited by these wavelet comparisons is again that point sources, not array sources, are preferred for S-wave imaging of geologic targets with buried-explosive sources.

Direct-P and Direct-SV Modes Produced by Single and Arrayed Vibrators

One portion of this source-test experiment involved data generated by vertical and horizontal vibrators positioned at each of the 16 source stations inside the 4-station X 4-station test patch illustrated in Figure 6. The objective was to determine the effects of intra-array statics on illuminating wavelets produced by vibrator arrays of variable dimensions and geometries. Even though these test data indicate the nature of intra-array source statics at only the Devine Test Site, several principles of intra-array statics can be deduced that apply to vibrator data generated in many basins.

Direct-P Modes Produced by a Single Vertical Vibrator

Although the objective of this report is to illustrate and document the nature of direct-SV wavefields produced by seismic sources, it is important to also investigate the nature of direct-P modes produced by popular P-wave seismic sources to establish a baseline for judging similarities and differences between direct-P and direct-SV modes produced by these sources. Thus the first step in discussing the direct modes produced by a vertical vibrator is to first illustrate the direct-P modes produced by the vertical vibrator that was used in this Devine Test Site study.

The direct-P mode generated at each of the 16 source stations by the test vertical vibrator are shown in Figure 15. These data were recorded by a 3C geophone at a depth of 2075 ft. The illuminating P wavefield produced at source station 11 (Figure 6) was arbitrarily selected as a reference to compare with direct-P modes produced at other source stations in the 16-station array. The station-11 wavelet is labeled **Reference**. The dash line drawn across each P wavelet shows the arrival time of a selected peak on the **Reference** wavelet. The amount by which the arrival time of this phase point is shifted at each vibrator is labeled on each wavelet panel in units of milliseconds. These time shifts represent the P-wave source static for a vertical-vibrator source at each station across the (4-station) X (4-station) vibrator test patch.

The direct-P mode has a consistent waveshape at all 16 source stations. Although the P static ranges from -5 ms to +5 ms across the 16-station patch, differences between static shifts at adjacent station points are small, usually only 1 or 2 ms. There are many ways to use these point-source vibrator data to construct direct-P illuminating wavelets by hypothetical arrays of vertical vibrators. For example if an array of two vertical vibrators is deployed, the illuminating wavelets produced by a 2-vibrator array at stations 9 and 10 would add in almost perfect phase agreement (only a 1 ms shift between the two source wavelets). However, if these same vibrators were positioned at stations 9 and 13, the summed wavelet would be distorted by the 6 ms static difference between the two direct-P modes produced at these two source stations. In each of these cases, the vibrator separation is fixed at 30 ft, but the differences in the illuminating composite wavelet can be significant.

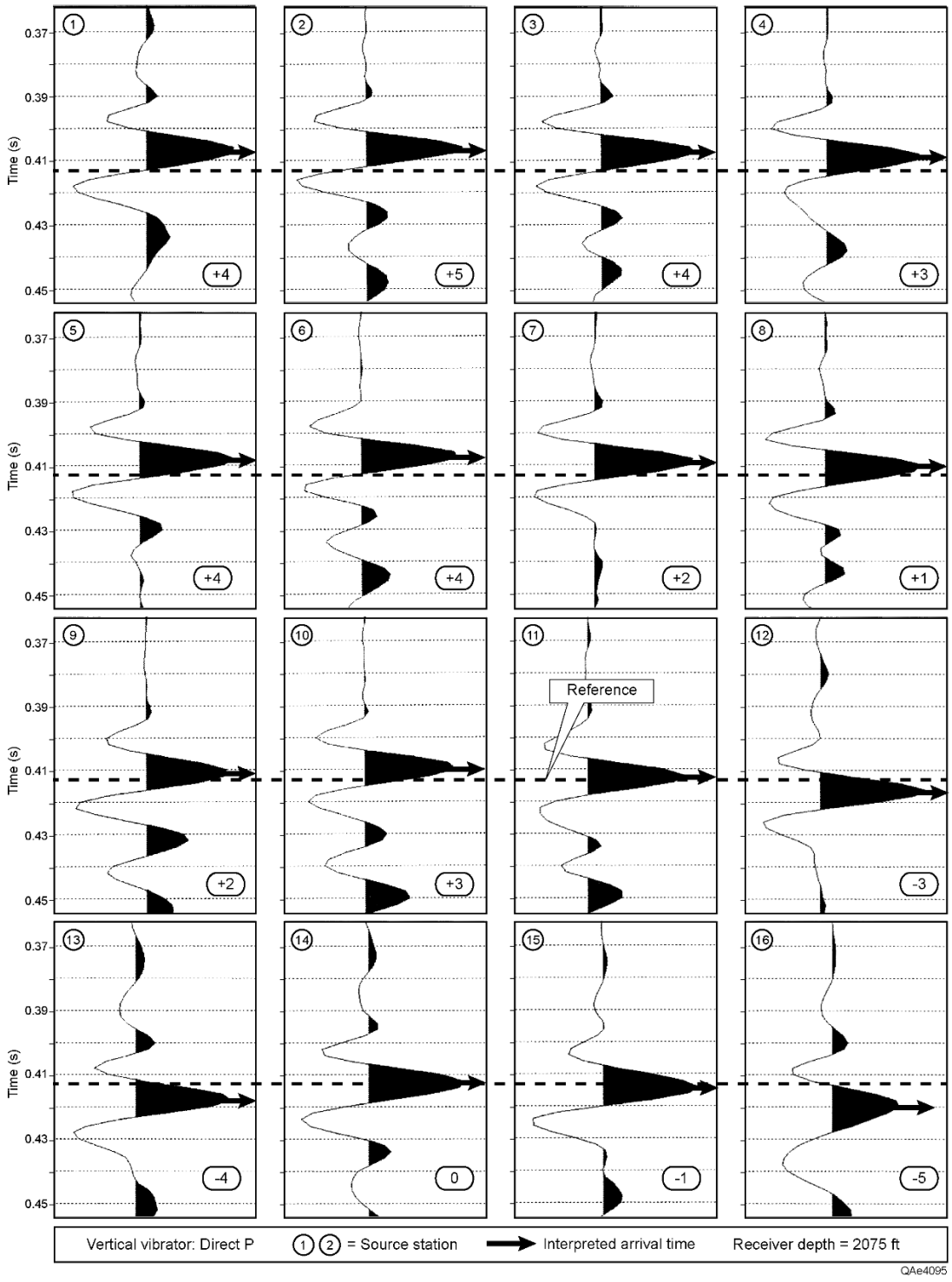

Figure 15. Direct-P wavelets generated by a vertical vibrator at each of the 16 source stations and recorded by a 3C geophone at a depth of 2075 ft. The source station where each direct-P mode was generated is identified by the circled number beside each wavelet. The direct-P mode produced at station 11 is chosen as a **Reference** wavelet. The intra-array P-wave static time shift between station 16 and each of the other source stations is labeled in the box beside each wavelet.

The principal established for buried explosive sources is demonstrated again by these vertical-vibrator data. That is, a single vertical-vibrator is an excellent P-wave source just as a single shot-hole is. This conclusion is based on the observation that a single vertical vibrator creates consistent-shape illuminating wavelets even when wavelets at some source stations have static shifts of several milliseconds.

Direct-P Modes Produced by an Array of Vertical Vibrators

Examination of the static time shifts posted on Figure 15 shows that vibrator test-pattern **C** (Figure 6) segregates into two P-static domains similar to what is observed at shot-hole test pattern **A**. These two static domains will again be referred to as **D1** and **D2**. Static domain **D1** is the half-space of pattern **C** where vertical-vibrator stations 1 through 8 are positioned (Figure 6). All P statics in domain **D1** are positive with values ranging from +1 ms to +5 ms. Static domain **D2** is the half space containing shot-holes 9 through 16. In contrast to domain **D1**, P statics in domain **D2** tend to be negative. The P static values in these two domains are distinctive in that, with the exception of stations 9 and 10, they differ in algebraic sign. As a result, illuminating P wavelets produced by arrays of 2, 3, or 4 vertical vibrators can have a variable waveshapes depending on where the array is located within the test patch. Some source-array options that can be made within test pattern **C** are exhibited in Figure 16.

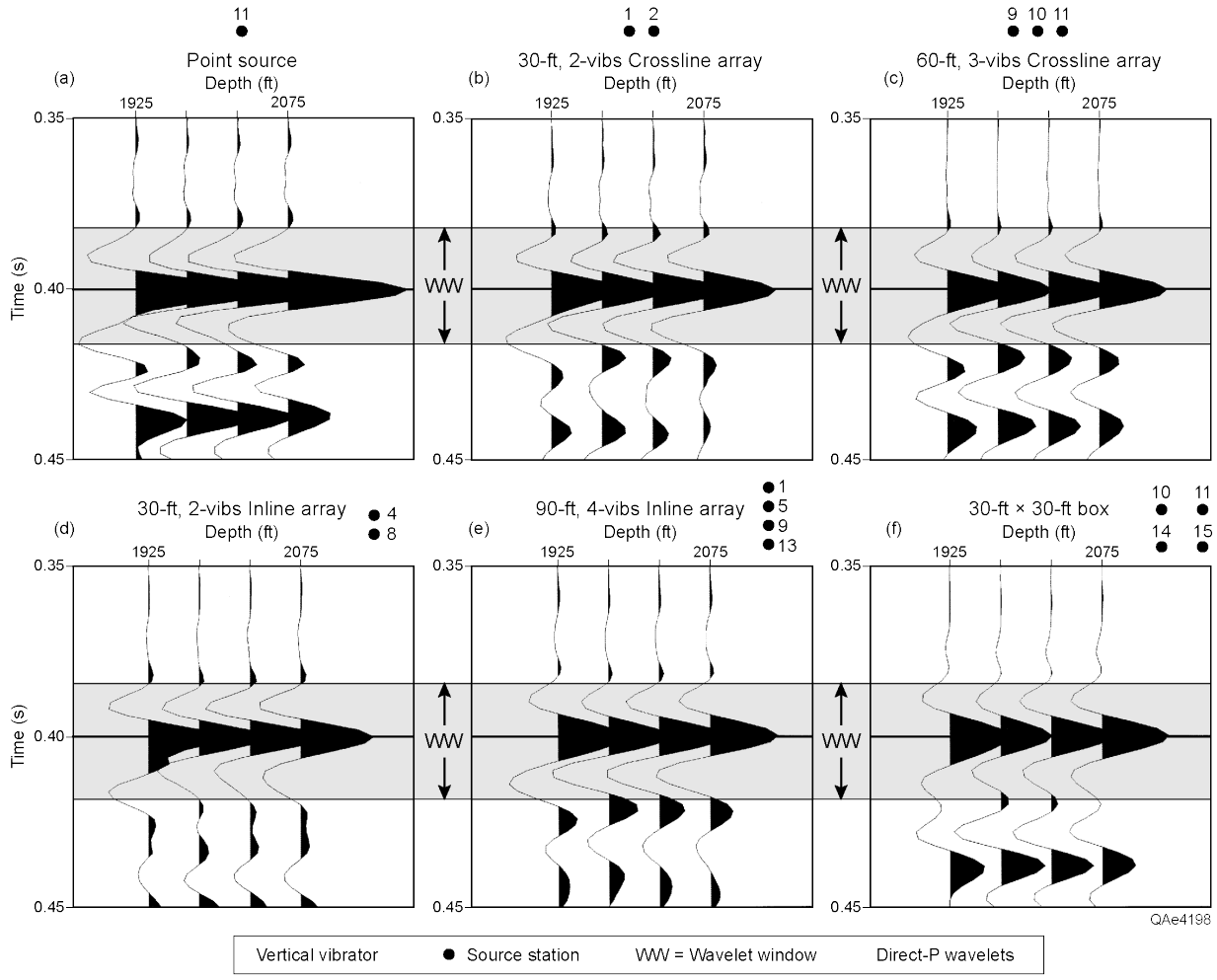

Figure 16. Direct-P modes produced by (a) a single vertical vibrator at station 16 and by arrays of vertical vibrators (b through f). The numbered dots represent vibrator station numbers in Figure 6. **WW** is the wavelet window.

These examples compare P wavelets generated by a single vertical vibrator (Figure 16a) with P wavelets generated by various arrays of vertical vibrators (Figures 16b through 16f). The specific vibrator stations that form each source array are identified by the numbered dots accompanying each set of wavelets. The depths of the receiver stations where the illuminating wavelets produced by each source were recorded (1925 ft to 2075 ft) are labeled on each data panel. There are only minor differences in the principal-energy portions of point-source wavelets and large-array wavelets inside wavelet window **WW**. An important principal exhibited by these wavelet comparisons is that vertical-vibrator arrays are often as good as a single vibrator for P-wave imaging of geologic targets. This is an encouraging finding for purposes of performing SV-P data processing with legacy vertical-geophone data generated by vertical-vibrator sources.

Direct-SR Modes Produced by a Single Vertical Vibrator

After subsurface 3C geophones are mathematically rotated to record downgoing direct-P and direct-SV modes produced by a seismic source, direct-SV modes will be observed on two of the rotated receivers. One receiver is the S sensor that is positioned in the vertical plane that passes through the source and receiver stations (which is called the SR mode in this report), and the second receiver is the S sensor that is perpendicular to this vertical plane (which will be called the ST mode). The direct-SV energy recorded by each of these sensors is controlled by the nature of S-wave splitting that exists at the data-measurement site.

The direct-SR mode generated by a vertical vibrator at each source station and recorded at a depth of 2075 ft are shown in Figure 17. The illuminating SR wavefield produced at source station 11 (Figure 6) was selected as a reference wavelet to compare with SR wavefields produced at other source stations in the 16-station array. The dash line drawn across each SR wavelet shows the arrival time of the black-peak phase for the illuminating SR **Reference** wavelet produced at station 11. The position of this reference phase on the direct-SR wavelet produced at all other vertical-vibrator source stations is marked with a bold arrow. The amount by which this reference phase point is shifted at each source station relative to the reference-phase wavelet is labeled on each wavelet panel in units of milliseconds. The time shift between the dash line and the arrow at each source station represents the SR static shift at that source station.

An encouraging characteristic of these direct-SR wavelets is that, with the exception of the wavelets produced at stations 8 and 9, they show that a vertical vibrator produces illuminating SR wavelets that have reasonably consistent waveshapes at all source stations. This consistent waveshape behavior of an illuminating SR wavelet is essential for making high-quality S-wave images. A second positive attribute of these vertical-vibrator direct-SR wavelets is that the SR static is not unacceptably large at most source stations. This intra-array SR static behavior implies SR data processing may not be excessively difficult when vertical vibrators are used as illuminating sources.

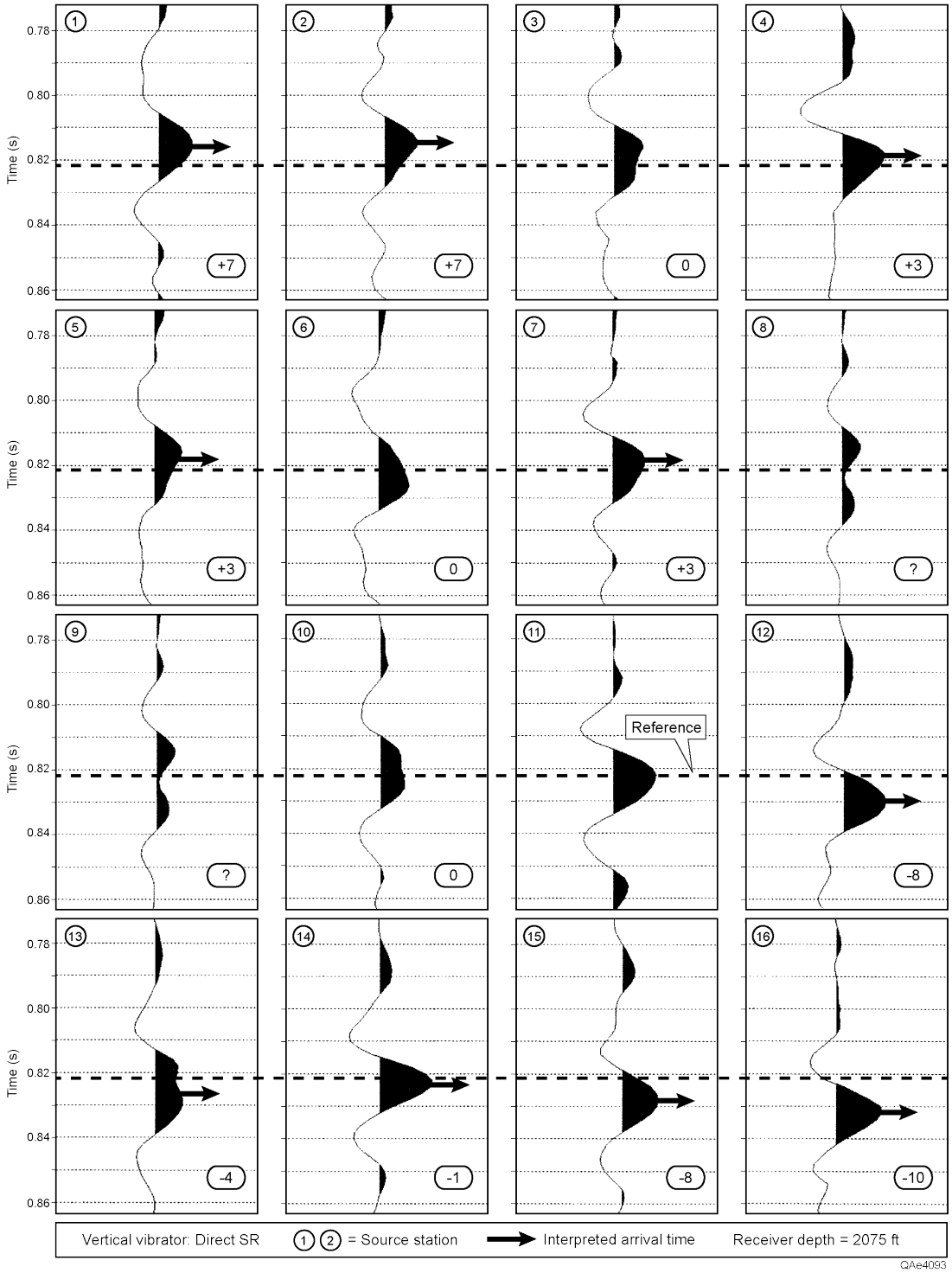

Figure 17. Direct-SR modes generated by a vertical vibrator at the 16 test stations in source patch **C** (Figure 6) and recorded by a geophone at a depth of 2075 ft. Source station location is identified by the circled number beside each wavelet. The SR wavelet produced at station 11 is chosen as a **Reference** wavelet. The intra-array SR-wave static time shift between station 11 and each of the other source stations is labeled in the box on each wavelet panel.

Direct-SR Modes Produced by an Array of Vertical Vibrators

The effects that source arrays can have on SR illuminating wavelets are illustrated in Figure 18. Point-source SR wavelets are displayed in Figure 18a, and SR wavelets produced by arbitrary arrays of vertical vibrators are shown in Figure 18b through 18f. Most of the imaging wavelets produced by each source array compare favorably with the ideal imaging wavelet of a point-source vibrator (Figure 18a). For example, the box array in Figure 18f produces SR imaging wavelets that are essentially equivalent to the ideal wavelets in Figure 18a. The bottom-line conclusion is that SR imaging with vertical vibrator sources is quite viable. Although large arrays result in usable SR wavelets at the Devine Test Site, it is still advisable to use only a single vertical vibrator if possible. A general conclusion is that the consistency of the illuminating direct-SR wavelets produced by various source array options of vertical vibrators is a welcome finding for purposes of processing legacy P-wave data for SV-P imaging.

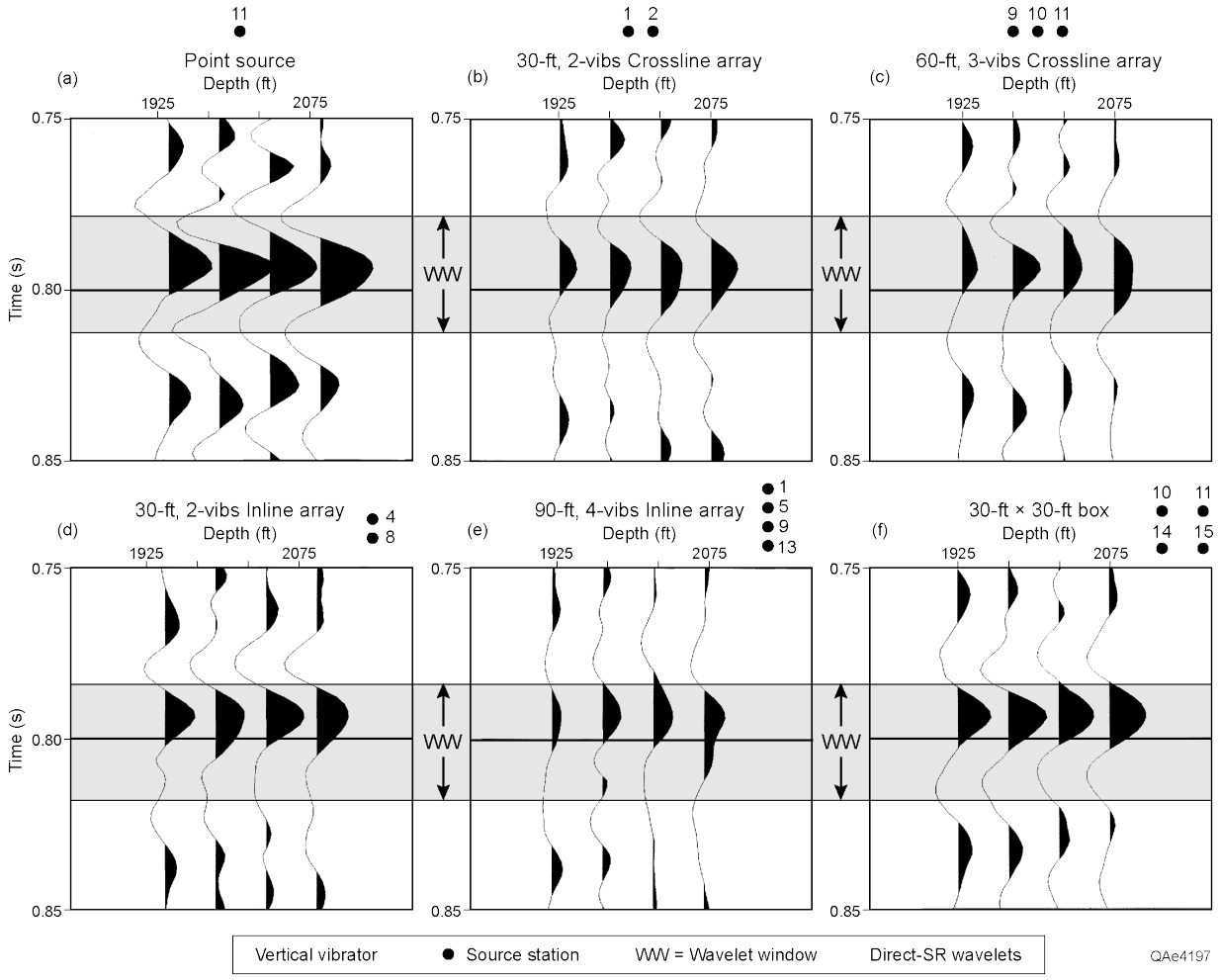

Figure 18. Direct-SR modes produced by (a) a single vertical vibrator at station 11 and by arrays of vertical vibrators (b through f). Numbered dots correspond to numbered vibrator stations in Figure 6. **WW** is the wavelet window.

Direct-ST Modes Produced by a Single Vertical Vibrator

The direct-ST first arrival generated at each of the 16 source stations by a vertical vibrator are shown in Figure 19. The illuminating ST wavefield produced at source station 11 was chosen as a **Reference** to compare with ST wavefields produced at other source stations across the 16-station array. The dash line drawn across each ST wavelet shows the interpreted arrival time for the illuminating direct-ST wavelet produced at station 11. The amount by which this direct-ST **reference** time is shifted at a source station relative to the wavelet phase identified by the arrow added to each wavelet, and the amount of time shift is labeled on each wavelet in units of milliseconds. Each of these ST-wave time shifts represents the ST static shift for the direct-ST mode produced at a source station.

At first glance, it appears the ST wavelets have low energy and small amplitudes. This appearance is caused by the fact that the ST-wavelet data file was corrupted, and the wavelet assigned to source station 7 was not a direct-ST wavelet but was a repeat of the direct-SR wavelet produced at station 7 (Figure 17). Only this one source station (#7) had an incorrect ST wavelet. The peak/trough amplitudes of this direct-SR wavelet are greater than the amplitudes of the corresponding direct-ST wavelets by a factor of approximately 2, and this larger SR-wavelet amplitude controls the display gain used for the total data panel in Figure 19. Thus the wavelet shown in source panel 7 should be ignored as indicated by the "X" drawn across the panel. When the remaining wavelets are examined, it is apparent that they all have a consistent waveshape. A valid conclusion is that the ST illuminating wavelets produced by a vertical vibrator are quite acceptable for direct-ST reflection imaging.

Direct-ST Modes Produced by an Array of Vertical Vibrators

The effects that source arrays can have on ST illuminating wavelets are illustrated in Figure 20. Point-source ST wavelets are displayed in Figure 20a, and source-array wavelets are shown as Figures 20b through 20f. The array in Figure 20e involves the summation of wavelets that have a difference in ST statics of 13 ms, which is a severe misalignment of wavelets. Even so, the imaging wavelet has a favorable but lower amplitude waveshape comparison with the ideal imaging wavelet of a point-source vibrator (Figure 20a). The box array in Figure 20f produces SR imaging wavelets that are essentially equivalent to the ideal wavelets in Figure 20a. The bottom-line conclusion is that ST imaging with vertical vibrator arrays should be viable. Although large arrays result in usable ST wavelets at the Devine Test Site, it is still advisable to use only a single vertical vibrator for S-wave reflection seismology if possible.

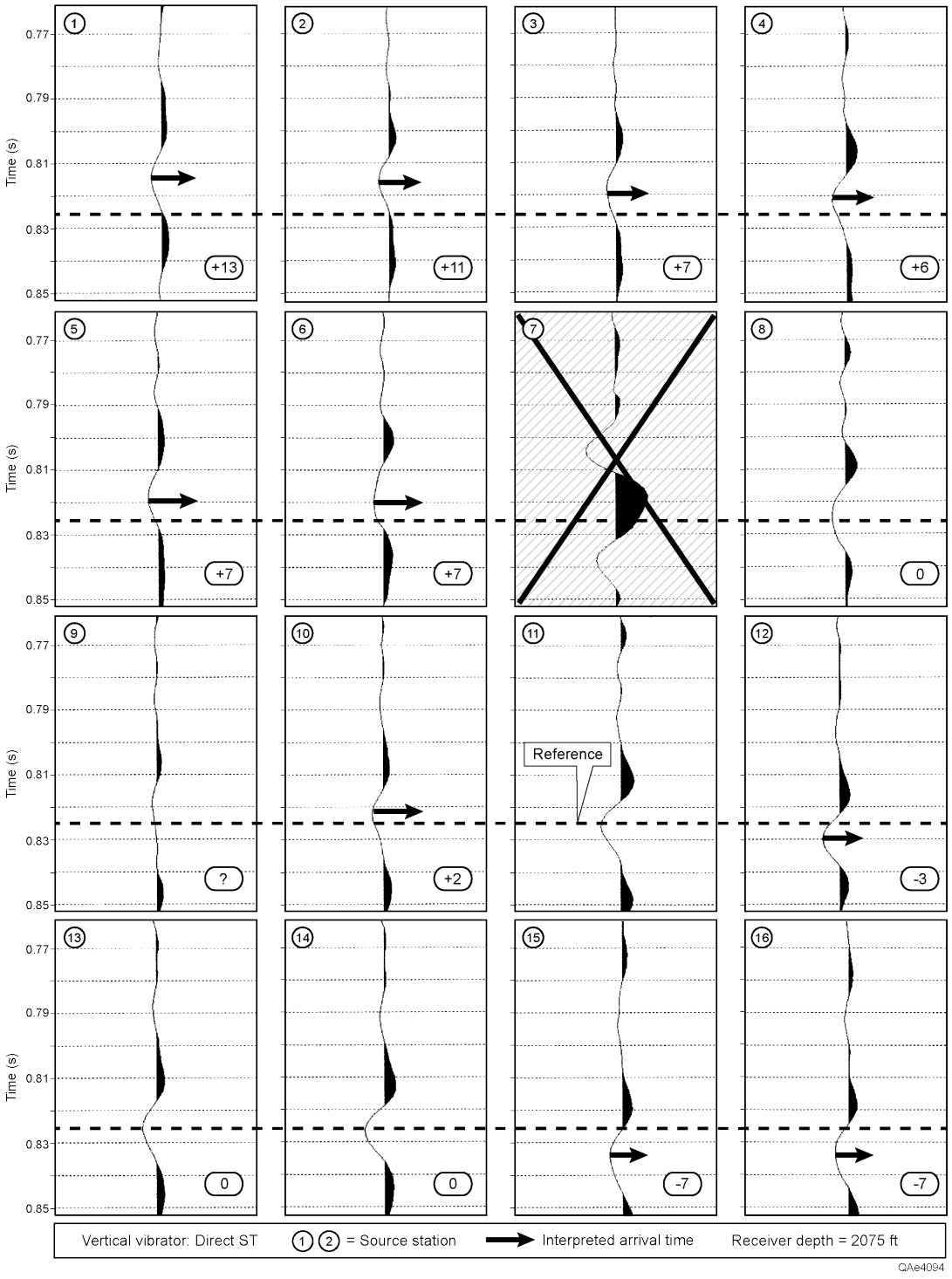

Figure 19. Direct-ST wavelets generated by a vertical vibrator at each source station across source patch **C** (Figure 6) and recorded at a depth of 2075 ft. The source station where each direct-ST mode was generated is identified by the circled number beside each wavelet. The ST wavelet produced at station 11 is arbitrarily chosen as a **Reference** wavelet. The intra-array ST-wave static time shift between station 11 and each of the other source stations is labeled in the box beside each wavelet. The wavelet shown for station 7 is discussed in the text.

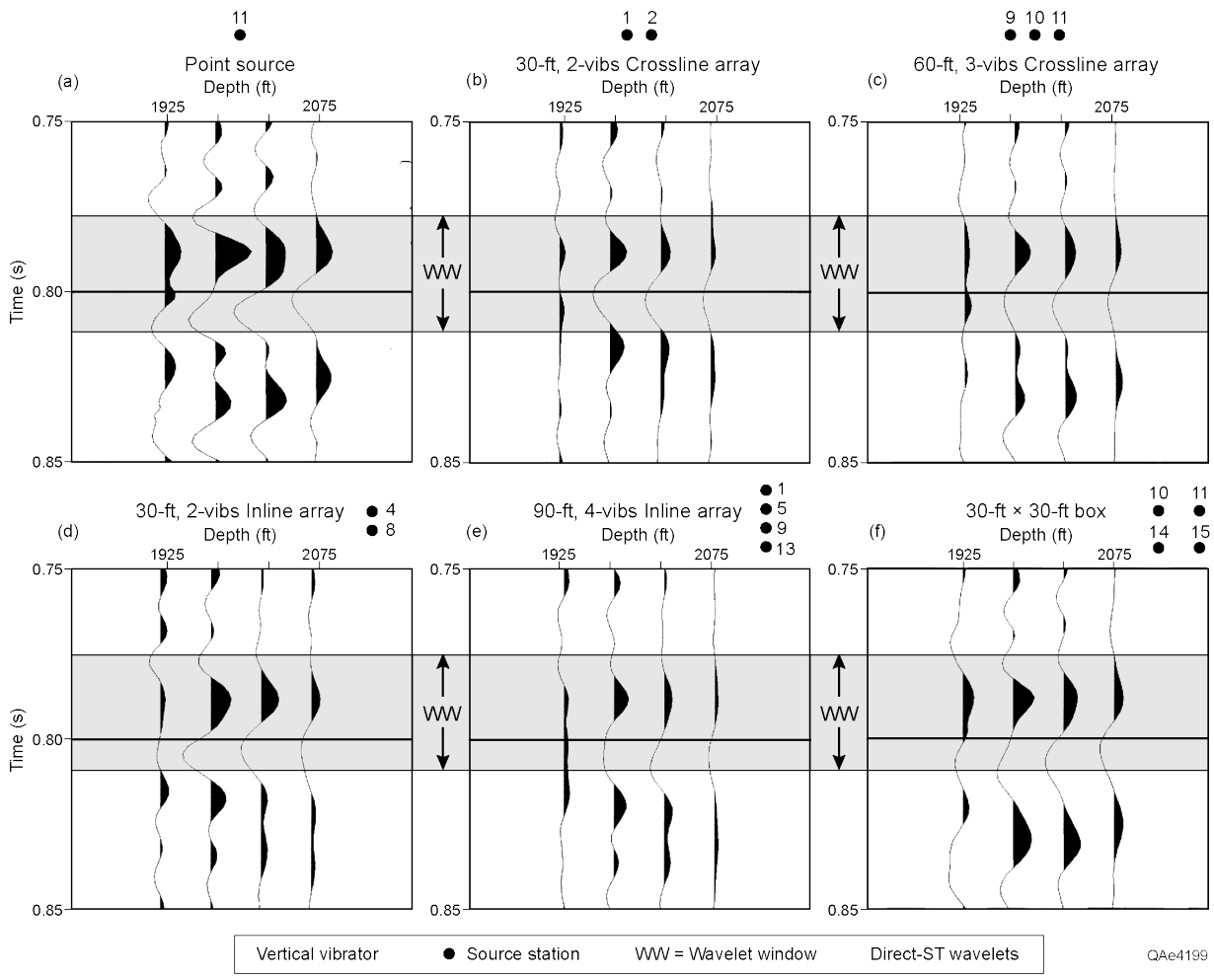

Figure 20. Direct-ST modes produced by (a) a single vertical vibrator at station 16 and by arrays of vertical vibrators (b through f). Numbered dots correspond to numbered vibrator stations in Figure 6. **WW** is the wavelet window.

Direct-SR Modes Produced by a Single Radial-Horizontal Vibrator

The direct-SR modes generated by a radial-horizontal vibrator at each of the 16 source stations are shown in Figure 21. The sensor that recorded these data was at a depth of 1975 ft. The illuminating SR wavefield produced at source station 11 was selected as a reference to compare with direct-SR modes produced at other source stations in the array. The dash line drawn across each SR wavelet shows the arrival time of the **reference** phase point selected for the direct-SR wavelet produced at station 11. The amount by which this reference-phase time shifts (as shown by the bold arrow) at each source station is labeled on each wavelet in units of milliseconds. Each of these direct-SR time shifts represents the SR source static shift that delays or advances the direct-SR mode at each source station.

This data display is important because it allows direct-SR illuminating wavelets produced by a radial-horizontal vibrator to be compared with the direct-SR wavelets produce by a vertical vibrator (Figure 17). In the authors' opinion, the direct-SR wavelets produced by the vertical vibrator have waveshapes that are just as consistent as the SR wavelets produced by the radial-horizontal vibrator and definitely have better resolution than do the radial-horizontal vibrator wavelets. Even though care was taken to ensure that the same amount of energy was generated by the vertical and horizontal vibrators over the frequency range 4 to 48 Hz (Figure 2), the vertical-vibrator SR wavelets are more compact than the corresponding SR horizontal-vibrator wavelets because frequencies higher than 48 Hz are embedded in the illuminating SR wavefield radiating from each vertical-vibrator source station. This conclusion about wavelet resolution can be reached by visual examination of the wavelets in Figures 17 and 21. The principal black peaks in the vertical-vibrator wavelets usually span 18 to 20 ms (Figure 17); whereas, the principal peaks of the horizontal-vibrator wavelets often span 25 to 30 ms (Figure 21).

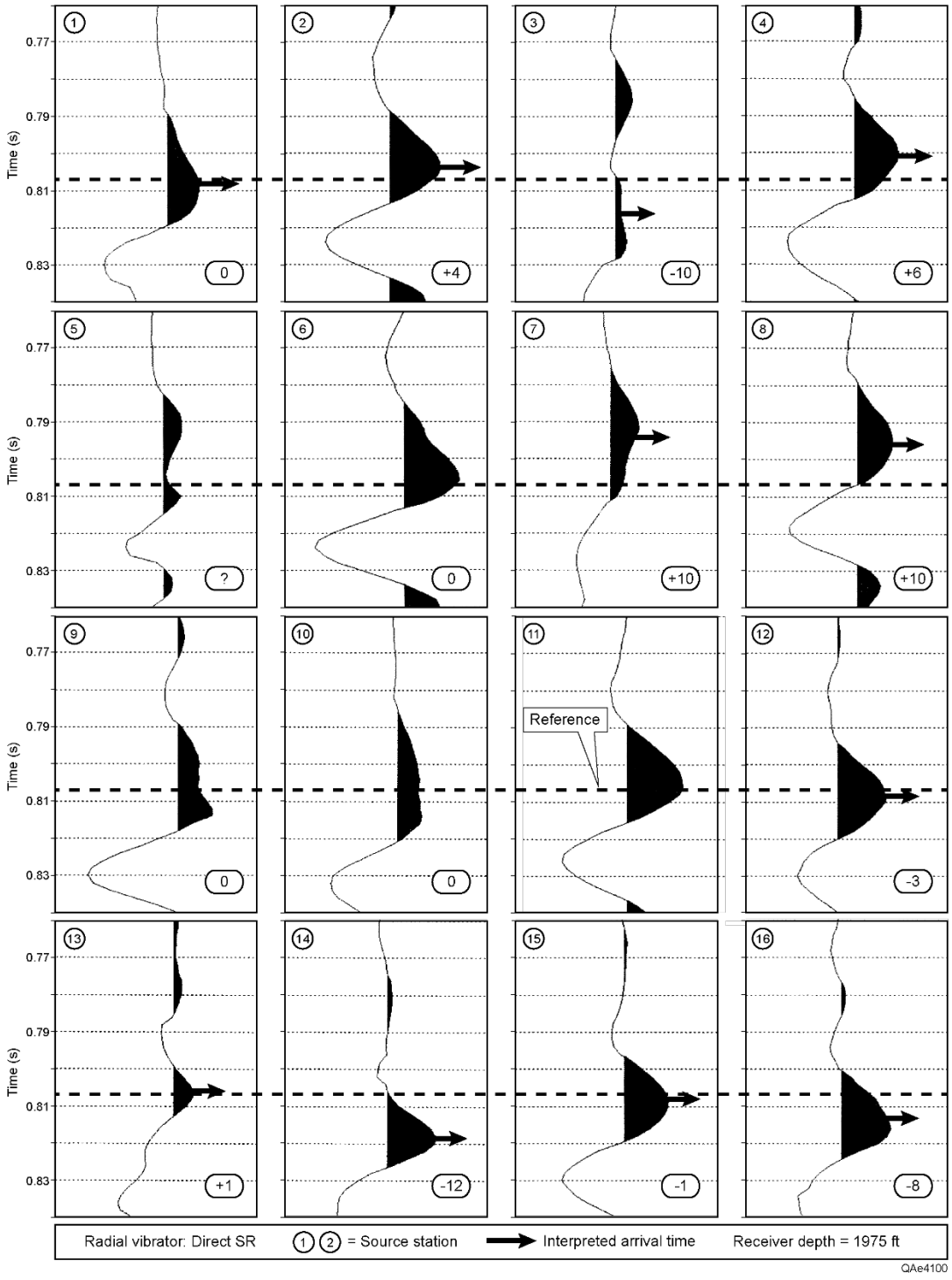

Figure 21. Direct-SR wavelets generated by a radial-horizontal vibrator and recorded by a 3C geophone at a depth of 1975 ft. The source station where each direct-SR mode was generated is identified by the circled number on each wave panel. The SR wavelet produced at station 11 is the **Reference** wavelet. The intra-array SR-wave static time shift (in ms) between station 11 and each of the other source stations is labeled in the box beside each wavelet.

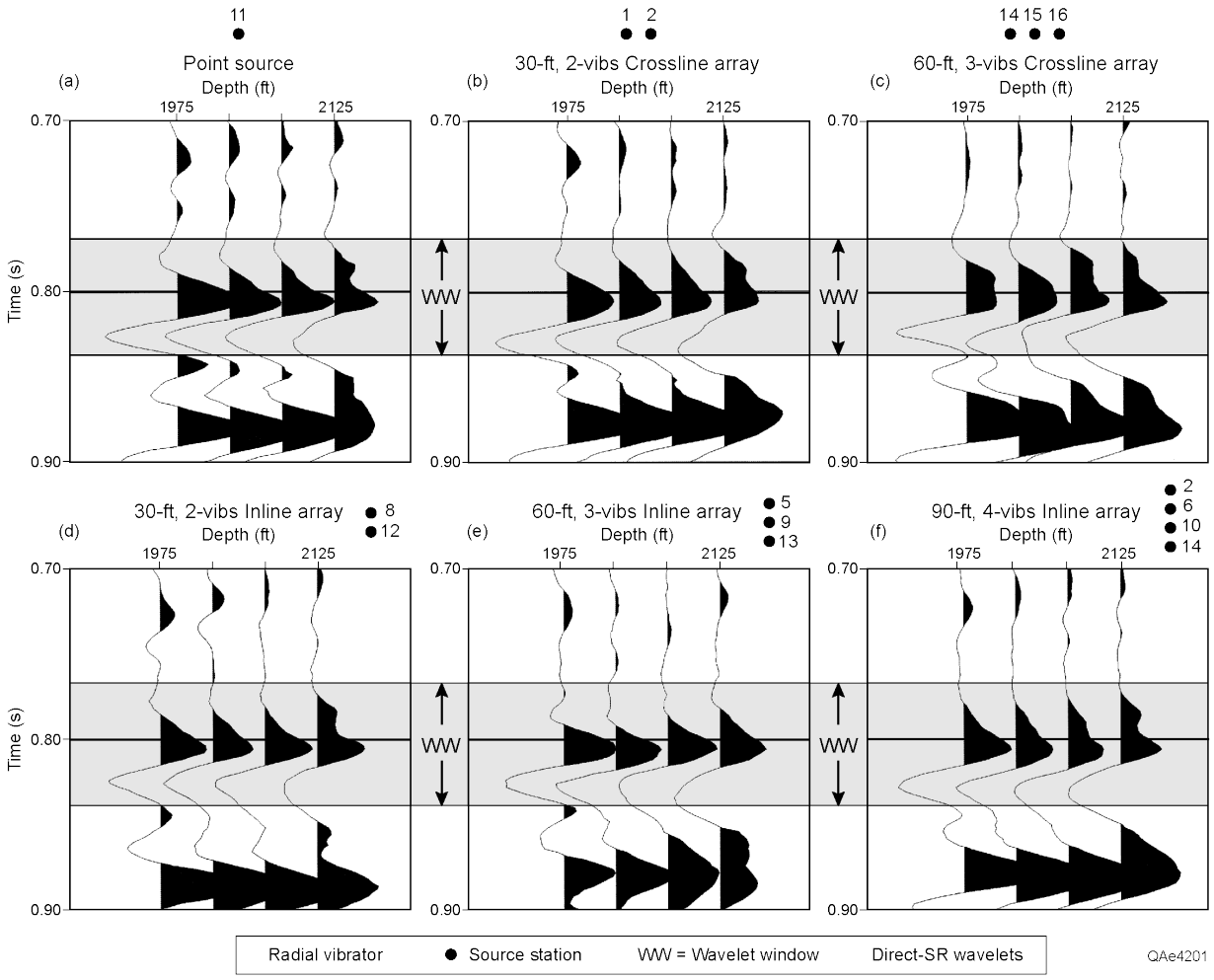

Figure 22. Direct-SR modes produced by (a) a single radial-horizontal vibrator at station 16 and by arrays of radial-horizontal vibrators (b through f). Numbered dots correspond to the same numbered vibrator station in Figure 6. **WW** is the wavelet window,

Direct-SR Modes Produced by an Array of Radial-Horizontal Vibrators

SR illuminating wavelets produced by different arrays of radial-horizontal vibrators are illustrated in Figure 22. SR wavelets are shown that are produced by a single radial-horizontal vibrator and by inline and crossline linear arrays of 2 to 4 radial-horizontal vibrators. The array in Figure 22d includes wavelets that have intra-array statics of 13 ms (stations 8 and 12, Figure 21), which is a significant misalignment of wavelet phase. Even so, the composite imaging wavelet has a rather good correlation with the ideal imaging wavelet of a point-source vibrator (Figure 22a). The inline 4-station array in Figure 22f involves wavelets with an intra-array static of 16 ms (Figure 21), but it also produces SR imaging wavelets that are essentially equivalent to the ideal wavelets in Figure 22a. The bottom-line conclusion is that SR imaging with arrayed radial-horizontal vibrators could be done in this test area. However, prudent field practice

would be to use only a single radial-horizontal vibrator if possible. An important fact illustrated by these test data is: ***the direct-SR wavelets produced by arrays of vertical vibrators (Figure 18) are equal in quality to the illuminating direct-SR wavelets produced by equivalent arrays of radial-horizontal vibrators (Figure 22).***

Direct-ST Modes Produced by a Single Radial-Horizontal Vibrator

The direct-ST modes generated across the 16-station test patch by a radial-horizontal vibrator are displayed on Figure 23. The transverse geophone that recorded these data was at a depth of 1975 ft. The illuminating ST wavefield produced at source station 11 was again selected as the **Reference** to compare with direct-ST modes produced at other source stations across the 16-station array. The dash line drawn across each ST wavelet shows where this **Reference** phase point should be, and the arrow shows where the **Reference** phase point actually is at each source station. The amount by which the station-11 **Reference** phase time differs from the time coordinate of the equivalent phase point for a direct-ST wavelet produced at source station N represents the ST source static at station N. This shift in the arrival time of the reference phase point is labeled on each wavelet panel.

These direct-ST wavelets are stable in the sense that the dashed reference-phase line intersects a prominent black peak on the wavelet produced at each source station. One implication is that ST static estimations should not be excessively difficult at the Devine Test Site if the illuminating ST wavelets are generated by a single radial-horizontal vibrator.

Direct-ST Modes Produced by an Array of Radial-Horizontal Vibrators

Figure 24a shows a small window of illuminating direct-ST wavelets produced by a radial-horizontal vibrator operating as a point source, the ideal type of direct-S source. This illuminating wavefield can be compared to the illuminating wavefields produced by various arrays of radial-horizontal vibrators in Figures 24b through 24f. All illuminating wavefields are high quality and essentially identical, which implies that arrays of radial-horizontal vibrators can be used in the area local to the Devine Test Site. However, the fundamental principle that a point-source is the better type of source to use in S-wave imaging should still be imposed if a single horizontal vibrator will generate sufficient signal-to-noise at this location.

An important observation is that the direct-ST wavelets produced by arrays of vertical vibrators (Figure 20) are reasonable approximations of the high-quality direct-ST wavelets produced by arrays of radial-horizontal vibrators (Figure 24). Comparison between wavelets produced by these two different vibrators is handicapped because of the wavelet scaling issue discussed for the data displayed in Figures 19 and 20.

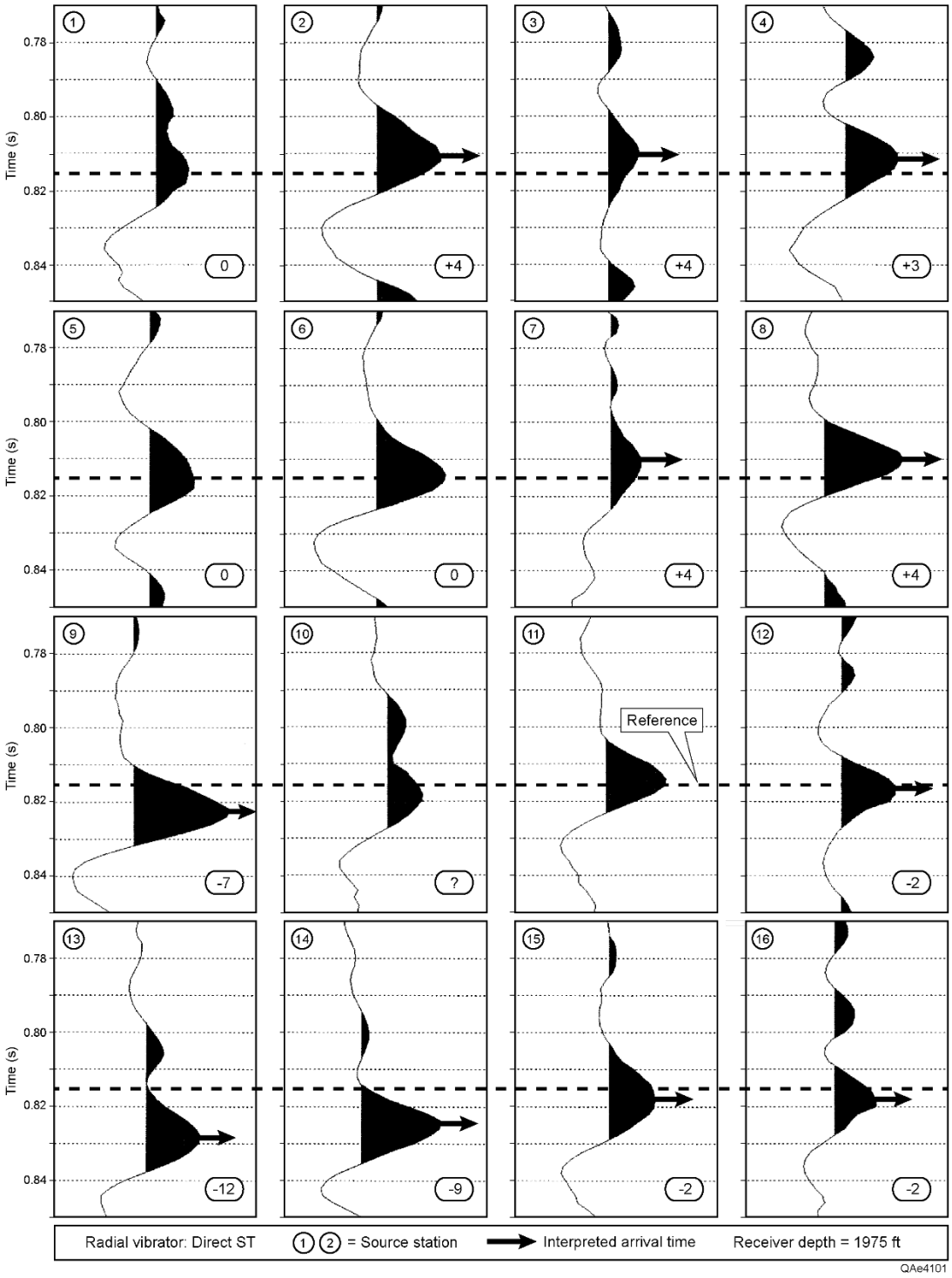

Figure 23. Direct-ST wavelets generated by a radial-horizontal vibrator at each of the 16 source stations of test patch **C** (Figure 6) and recorded by a 3C geophone at a depth of 1975 ft. The source station where each direct-ST mode was generated is identified by the circled number on each panel. The ST wavelet produced at station 11 is arbitrarily chosen as a **Reference** wavelet. The intra-array ST-wave static time shift between station 11 and each of the other source stations is labeled in the box beside each wavelet.

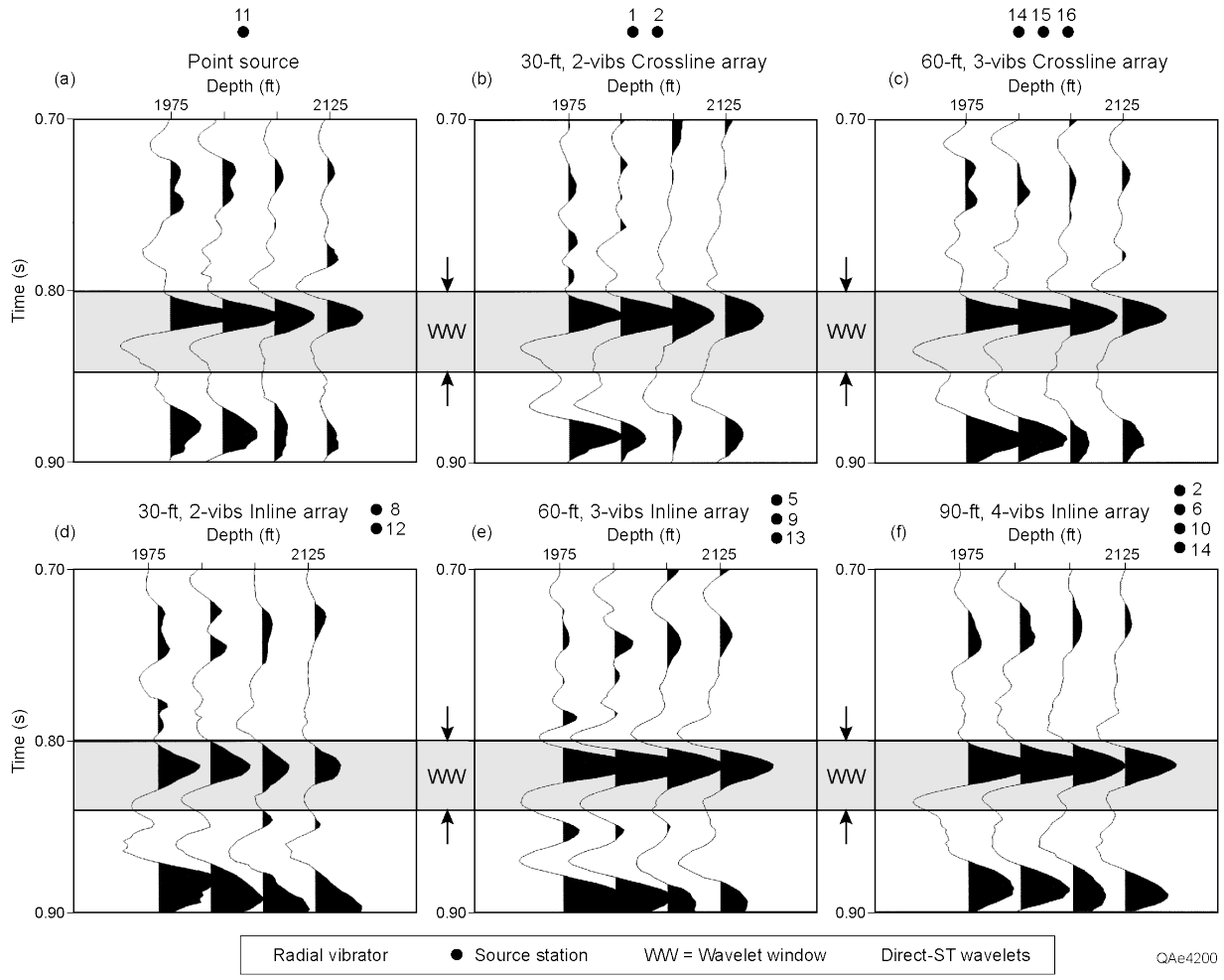

Figure 24. Direct-ST modes produced by (a) a single radial-horizontal vibrator at station 11 and by arrays of radial-horizontal vibrators (b through f). Numbered dots identified the numbered vibrator stations in Figure 6 that were used to form each source array. **WW** is the wavelet window.

Direct-SR Modes Produced by a Single Transverse-Horizontal Vibrator

The direct-SR mode generated at each of the 16 source stations by a transverse-horizontal vibrator are shown in Figure 25. The radial geophone that recorded the data was positioned at a depth of 1075 ft. The direct-SR illuminating wavelet produced at source station 11 was selected as the **Reference** wavelet to compare with direct-SR wavelets produced at other source stations in the (4-station) X (4-station) test patch. The dashed line crossing each SR wavelet shows where the arrival time of the **Reference** phase point should be positioned. The arrow on each wavelet shows where the **Reference** phase point actually is. These interpreted **Reference** times (arrows) are chosen so that there will be the smallest possible SR source static at each transverse-horizontal vibrator station. This interpretation philosophy may result in a biased view of the magnitude of SR source statics for this transverse-horizontal vibrator source.

As a general observation, the wide range of SR wavelet shapes is not desirable. The **Reference** wavelet at source station 11 is a reasonable approximation of a zero-phase wavelet that would be expected to be produced by a vibroseis source. A similar "almost" zero-phase wavelet was generated at source station 4, and perhaps at station 5. These three direct-SR wavelets (stations 4, 5, and 11), provide hints that the leading peak of each wavelet in the time window spanning 0.51 to 0.54 sec does not have a consistent shape and amplitude. The shape of this first peak of the direct-SR wavelet shows highly irregular character in all other source wavelets and complicates picking reliable reference times across the 4 X 4 station array. Examples of double-peak waveshapes that were troublesome are the wavelets produced at stations 6, 7, 9, 13, 14, and 15. For most of these examples, the arrival time was picked near the center of the leading double-peak feature (e.g. station 9) or on the dominant peak of the 2-peak pair (e.g. station 15).

The amount by which SR reference time at station N is shifted relative to the **Reference** time established at station 11 is labeled in the box accompanying each wavelet. This time shift number is expressed in units of milliseconds. This shift in phase-reference time for each SR-wavelet will be assumed to represent the SR source-static associated with the illuminating SR mode produced at each source station.

Direct-SR Modes Produced by an Array of Transverse-Horizontal Vibrators

The wide range of SR waveshapes produced by a transverse-horizontal vibrator (Figure 25) implies arrays of transverse-horizontal vibrators will often not be a desirable source option. This fact is demonstrated by the array-generated illuminating SR wavelets exhibited in Figure 26. The illuminating SR wavefield generated by a single transverse vibrator and recorded by deep geophones is shown in Figure 26a. These point-source data have a consistent-shape SR wavelet. In contrast, the accompanying wavelets produced by source arrays range from terrible (Figures 26b and 26c) to excellent (Figure 26e).

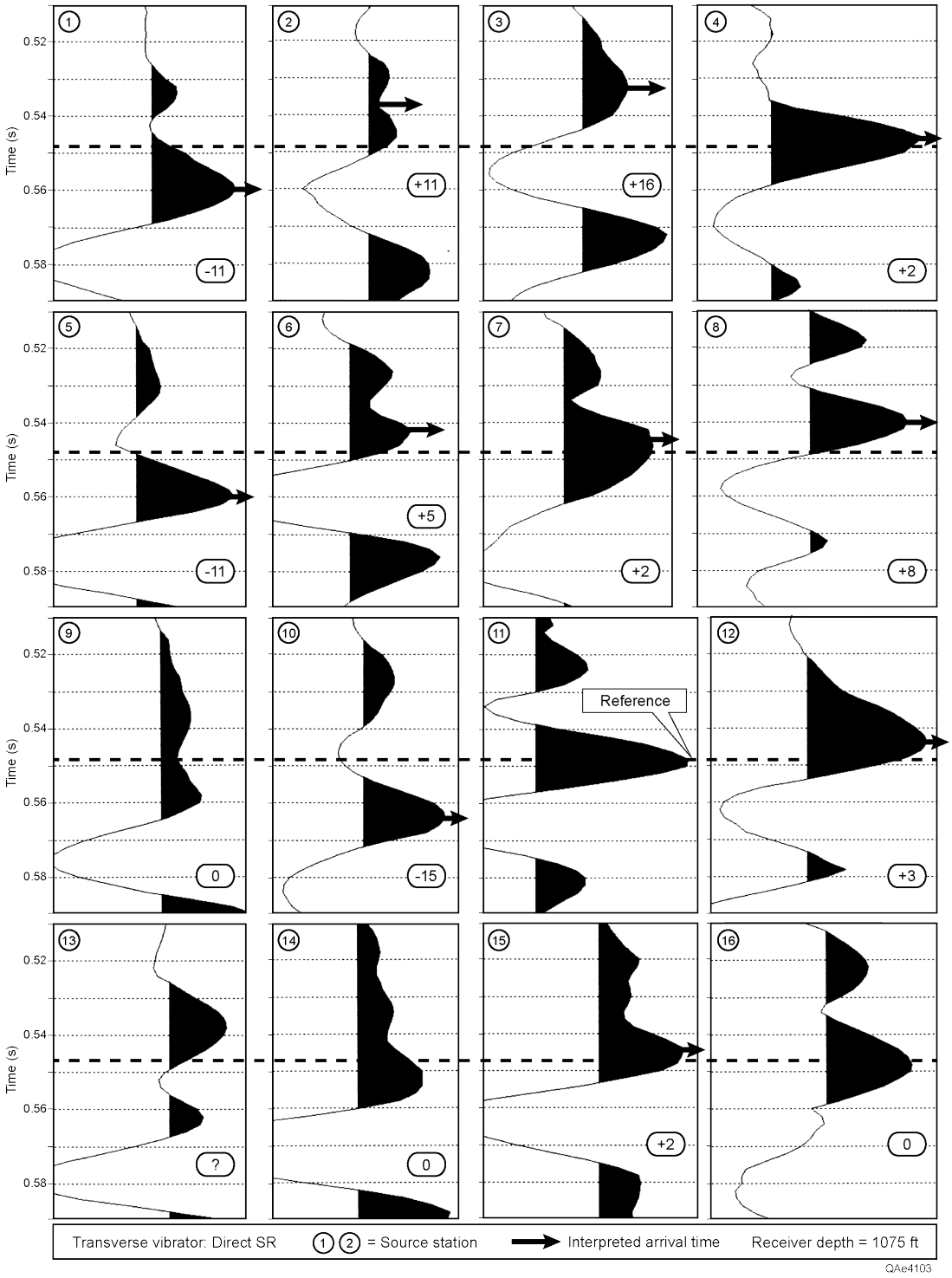

Figure 25. Direct-SR modes generated by a transverse-horizontal vibrator at each of the 16 source stations and recorded by a rotated radial-S geophone at a depth of 1075 ft. The location of each source station is identified by the circled number on each panel. The SR wavelet produced at station 11 is the **Reference** wavelet. The intra-array SR static time shift between station 11 and each source station is labeled in the box accompanying each wavelet.

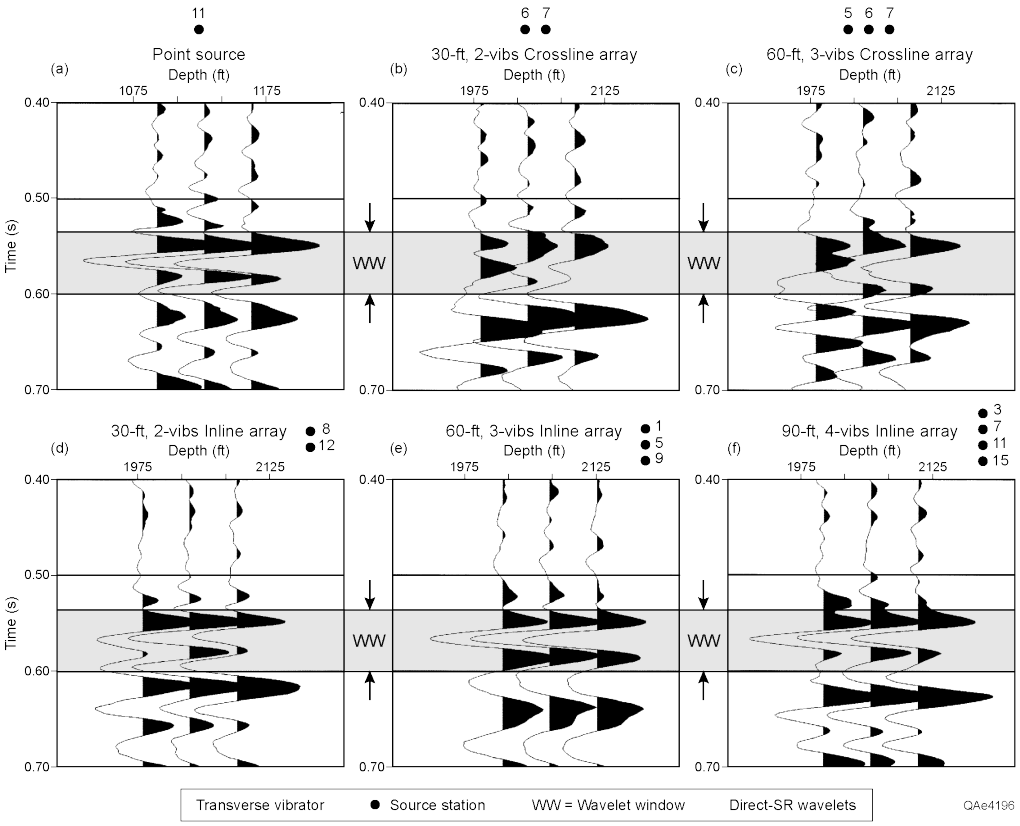

Figure 26. Direct-SR modes produced by (a) a single transverse-horizontal vibrator at station 11 and by arrays of transverse-horizontal vibrators (b through f). Numbered dots refer to numbered vibrator stations in Figure 6. **WW** is the wavelet window.

A frustrating aspect of attempting to construct acceptable arrays of transverse-horizontal vibrators is that there is no correlation between array size and the quality of the illuminating direct-SR wavelets. For example, wavelets produced by a 60-ft array (Figure 26c) are no worse than the wavelets produced by a 30-ft array (Figure 26b). If a 30-ft array is unacceptable, the only option is to use a single transverse-horizontal vibrator. If a 2-vibrator array produces an inappropriate illuminating wavefield, certainly 3-vibrator and 4-vibrator arrays would also be unacceptable. Thus these test data again provide evidence that a point source is the preferred source for S-wave analysis of prospects.

An important observation is - ***the illuminating direct-SR wavelets produced by arrays of vertical vibrators (Figure 18) are superior to the illuminating direct-SR wavelets produced by arrays of transverse-horizontal vibrators Figure 26).*** This observation may not be a general principle that applies to all prospects, but it certainly applies to these test data acquired at the Devine Test Site.

Direct-ST Modes Produced by a Single Transverse-Horizontal Vibrator

The direct-ST mode generated at each of the 16 source stations by a transverse-horizontal vibrator are shown in Figure 27. The data were recorded by a geophone positioned at a depth of 1075 ft.The illuminating ST wavelet produced at source station 11 is the **Reference** wavelet that will be used to compare with direct-ST wavelets produced at other source stations in the (4-station) X (4-station) test patch. The dashed line drawn across each ST wavelet shows where the selected phase-point arrival time for the illuminating ST wavelet associated with source station 11 should be. The arrow drawn on each wavelets shows where that arrival time is actually located.

As a general observation, the wide range of ST wavelet shapes is not desirable. The illuminating wavelet produced at several source stations is not representative of a zero-phase wavelet that should be produced by a vibrator. Examples of this departure from zero-phase character would be the wavelets produced at stations 3, 4, 5, and 12. The variable shapes of the illuminating wavelets will complicate determining ST statics at many transverse-horizontal vibrator source stations.

The selection of the point on each wavelet where the phase-reference time should be (the arrows) is arbitrary. For wavelets having a leading double-peak rather than single-peak feature, the arrival time was picked either near the center of the double-peak (as at station 4) or at the apex of the dominant peak of the 2-peak pair (as for station 5). Some data processors would pick difference phase points than what are exhibited in Figure 27. The amount by which the selected ST **Reference** time at station N is shifted relative to the **Reference** time established at **Reference** station 11 is labeled in the box accompanying each wavelet. This time shift number is expressed in units of milliseconds. This shift in phase-reference time for each ST-wavelet will be assumed to represent the ST source-static associated with the transverse-horizontal vibrator illuminating ST mode produced at each source station.

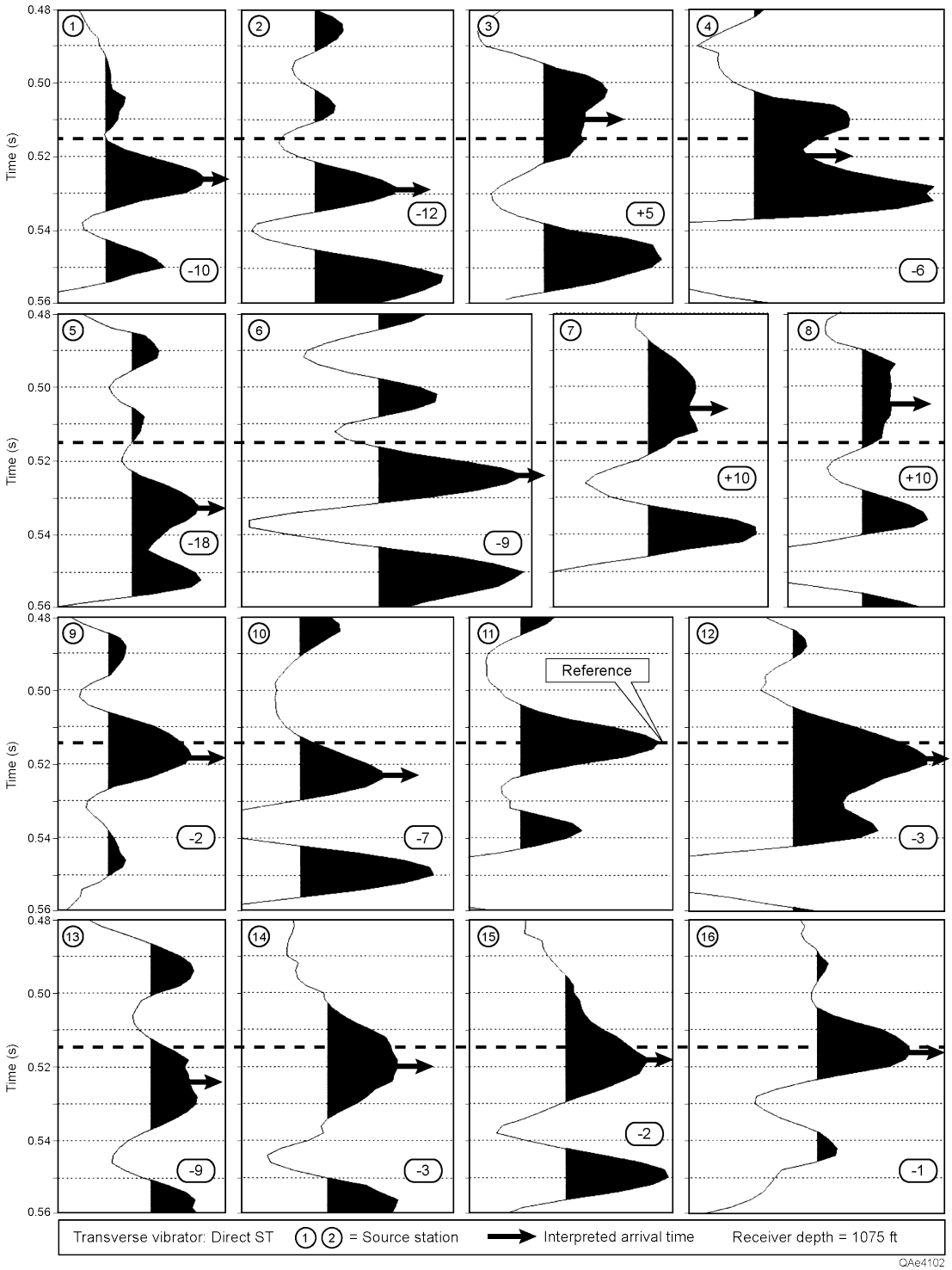

Figure 27. Direct-ST wavelets generated by a transverse-horizontal vibrator at each source station across test patch **C** (Figure 6) and recorded at a depth of 1075 ft in. The source stations where each direct-ST mode was generated are identified by the circled numbers. The ST wavelet produced at station 11 is the **Reference** wavelet. The intra-array ST source-static at each source stations is labeled in the box on each wavelet panel (in ms).

Direct-ST Modes Produced by an Array of Transverse-Horizontal Vibrators

The same combinations of source stations used to compare SR wavelets produced by a point source and source arrays of transverse-horizontal vibrators (Figure 26) are used here to compare ST wavelets (Figure 28) for the same vibrators. The point-source ST wavelets (Figure 28a) have more side lobes than the SR wavelets (Figure 26a), which is undesirable. We conclude that none of the direct-ST illuminating wavelets in Figure 28 are acceptable. Again, a key observation is – ***the direct-ST wavelets produced by vertical vibrators (Figure 20) are better for imaging purposes than are the direct-ST wavelets produced by the transverse-horizontal vibrators (Figure 28).***

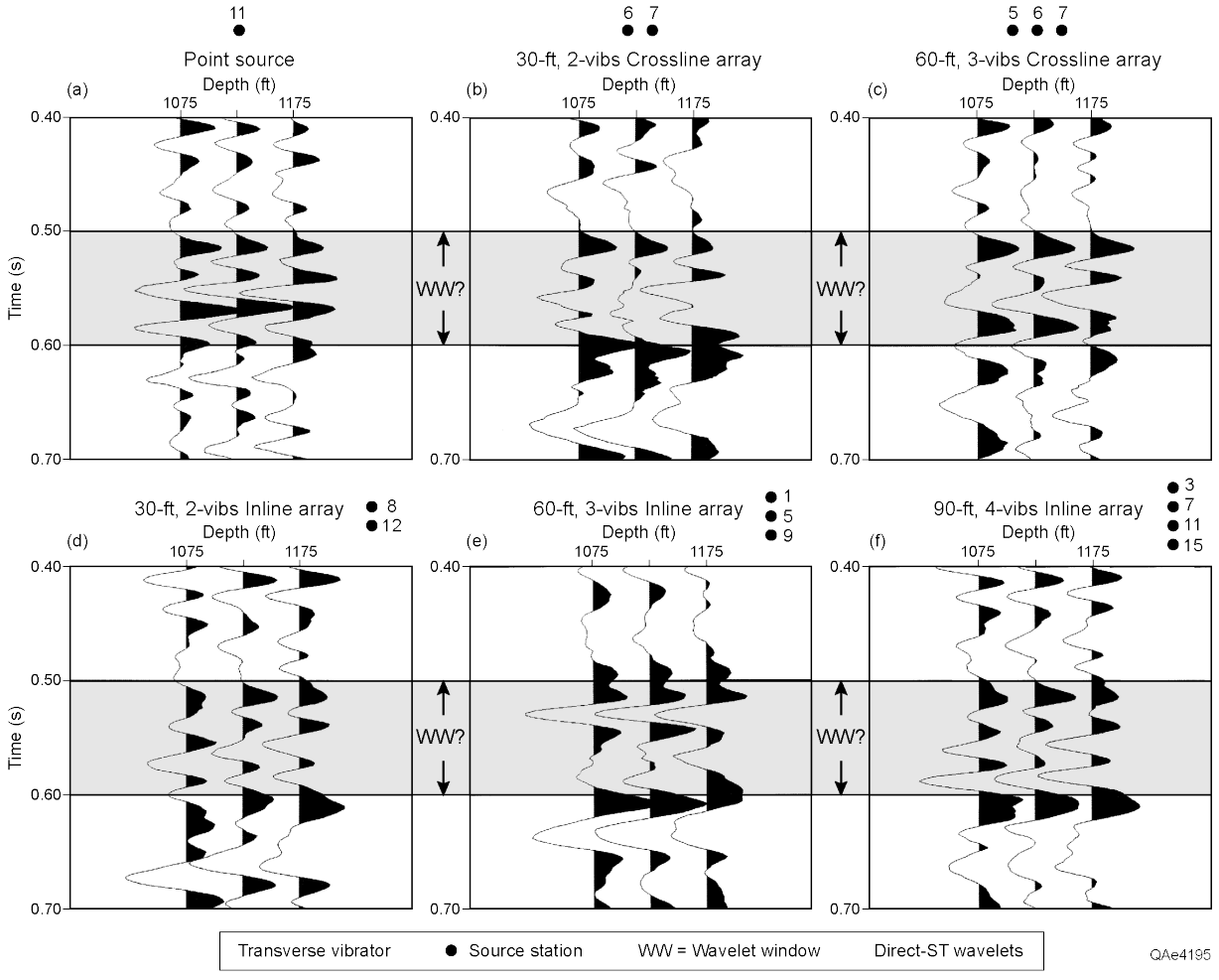

Figure 28. Direct-ST modes produced by (a) a single transverse-horizontal vibrator at station 11 and by arrays of transverse-horizontal vibrators (b through f). Numbered dots define the numbered vibrator stations in Figure 6 that were used to construct each array of transverse-horizontal vibrators. **WW** is the wavelet window.

Appendix A: The Elusive S* Wave

Introduction

The subject of S* (pronounced "S-star") waves sometimes arises when people discuss S waves produced by buried explosives. Many geophysicists have not heard of S* waves, and some who have, often do not know what these waves are. EGL's interest in S* waves is driven by the fact that some geophysicists claim:

1. A buried explosive does not produce direct-S waves but only direct-P waves, and

2. S waves that appear in buried-explosive data are converted-SV modes generated by P-wave conversion at the free surface above a buried explosive and include S* waves if the shot is close to the earth's surface (below the earth-air interface by less than one-half of the dominant wavelength of the direct-P wavelet).

Because the only sources that can create S* waves are buried sources positioned near the earth's surface, these waves, if they exist, should be present in data generated by shallow shot-hole explosives used to explore for oil and gas. No one has ever proposed that S* waves are associated with surface-based sources such as vertical vibrators and vertical impacts. In fact, theoretical studies show that only a pure-P point source positioned a short distance below a free surface will generate S* waves (Daley and Hron, 1988; Fertig, 1984; Fertig and Krajewski, 1989; Kim and Behrens, 1986). This term "**pure-P**" refers to a source that generates only P waves and absolutely no S waves. Because the source-array test data discussed in this report involve data produced by buried explosives, it is appropriate to determine if S*waves exist in the source test data collected at the Devine Test Site.

The Origin of the S* Wave Concept

The concept of S* waves was introduced by Hron and Mikhailenko (1980) in an oral paper presented at the 1980 meeting of the European Association of Engineers and Geophysicists (EAEG). The material presented in their oral paper was then published for wider distribution (Hron and Mikhailenko, 1981). This 1981 paper discusses the mathematical modeling that generated these new S* shear waves. No real seismic data were shown to verify their S* numerical calculations.

Figure A1a shows the source model that Hron and Mikhailenko used, and Figures A1b and A1c show Fertig's (1984) version of P and S wavefields calculated for this model. The earth medium used in the modeling was homogeneous, and the only interface was a free surface above a buried pure-P source. This pure-P point source was placed at position **A** at a shallow depth of λ/8 (15 meters in this model), where **λ** is the dominant wavelength of the propagating direct-P wavelet produced by the buried source. A series of N receivers buried at a depth of 3λ (360 meters) extended away from the source. Both vertical and horizontal displacements were

calculated at each receiver location along this buried receiver profile. The analytical solution (Figures A1b and A1c) showed a downward propagating direct-P wave (labeled **P**) and also a downward-traveling P wave that reflected from the free surface (labeled **pP**). In this notation, a lower-case **p** indicates the upgoing P wave produced by the buried pure-P source. These **P** and **pP** waves combine to form the total downgoing P wavefield.

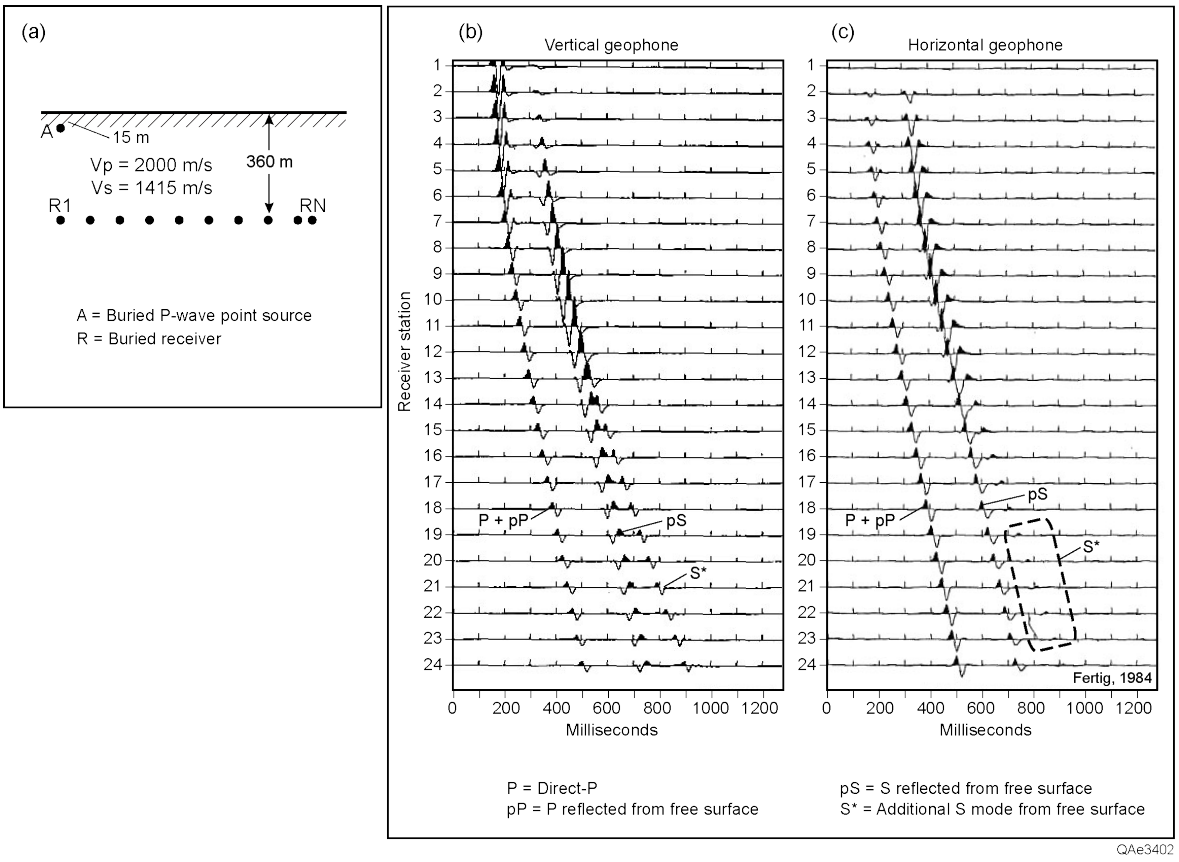

Figure A1. (a) Earth model showing the positions of a buried point source **A** and a buried profile of receiver stations (**R1** through **RN**). Source **A** is allowed to generate only P waves. (b) Calculated response of vertical geophones along the receiver profile. (c) Calculated response of horizontal geophones along the receiver profile. Although the wiggle traces in (b) and (c) are presented as a vertical array of receivers, the receiver stations were a horizontal profile (a). Modified from Fertig, 1984.

When a "pure-P" source assumption is used in S* numerical modeling, the only S waves that can appear in the calculations are forced to be converted-SV modes produced by upgoing P waves at the free surface above the buried source. The converted-SV mode produced by the pure-P source in Fertig's 1984 work is labeled **pS** in Figure A1. However, a second, unexpected S-wave with peculiar properties accompanied this **pS** wave in this "pure-P source" modeling approach. This new S wave is labeled **S***in Figures A1b and A1c. The **pS** and **S*** waves illustrated in Figure 1 are taken from Fertig's (1984) paper. His modeled S modes are identical to the S*

results introduced by Hron and Mikhailenko (1980, 1981). Puzzling questions about this proposed S* mode that need to be considered are:

1. Why does the **S*** wavelet propagate with a slower velocity than the converted **pS** wavelet? The earth model was assigned a homogeneous V_S velocity, but only the **pS** mode propagates with that assigned velocity (Figure A1b).

2. Why does the S* velocity become slower with increasing propagation distance while the **pS** mode maintains a constant velocity (Figure A1b)?

Numerical Modeling of S* Waves

Several researchers became fascinated about S* waves following the initial, model-based revelation of their existence by Hron and Mikhailenko (1981). The S* references in this report are limited to the key papers (Daley and Hron, 1988; Daley, 2002; Fertig, 1984; Fertig and Krajewski, 1989; Gutowski, et al., 1984, Kim and Behrens, 1986, Lash, 1985).

An important assumption imposed on numerical calculations of S* waves is that the buried source radiates only P waves. This critical assumption is emphasized in Figure A1a. The buried source is simply not allowed to generate any direct-S waves. To quote Fertig (1984), "*The main assumption throughout the paper is the existence of a point-source which produces only compressional waves*". In EGL's opinion, this source assumption is a serious error that does not apply to real seismic reflection data created by real buried explosives and disagrees with EGL's buried explosive test results documented in Figures 11 through 14 of the main text.. Any numerical modeling done to simulate real seismic data should allow a buried source to radiate both direct-P and direct-S waves.

Daley (2002) did an investigation of the paper by Hron and Mikhailenko (1981) that started this S* interest and showed that the saddle point approximations used in that initial modeling work were inappropriate, and he repeated the modeling with "improved" definitions of the required saddle points. However, Daley's new modeling yielded essentially the same S* result that was reported in the initial modeling by Hron and Mikhailenko. This investigation by Daley appears to be the last published numerical modeling research that focuses on the elusive S* wave. Daley (2002) summarized the physics of numerically modeled S* waves with the following observations, which are illustrated in graphical form in Figure A2:

1. An S* wave originates at a point E* located directly above a buried pure-P source at the earth-air interface (Figure A2a, A2b).

2. S* energy propagates away from origin point E* at takeoff angles that exceed angle θ* defined as $\theta^* = \sin^{-1}(V_S/V_P)$. In this expression, θ* is measured from the vertical axis that passes through the buried source E and point E* where the S* mode originates.

3. An S* wavelet is linearly polarized in the vertical plane at a right-angle to its raypath. This polarized displacement causes vertical-geophone responses to be large, and horizontal-geophone responses to be small, at far-receiver offsets (Figure A1b, A1c).

4. The amplitude of an S* wave decays linearly over short travel distances away from source point E* and then decays exponentially as travel distance increases. Thus an S* wave has the properties of an **evanescent wave**, which by definition, means an S* wave will not be effective for imaging deep geologic targets because of its rapid loss of energy as it propagates away from the interface where it was created.

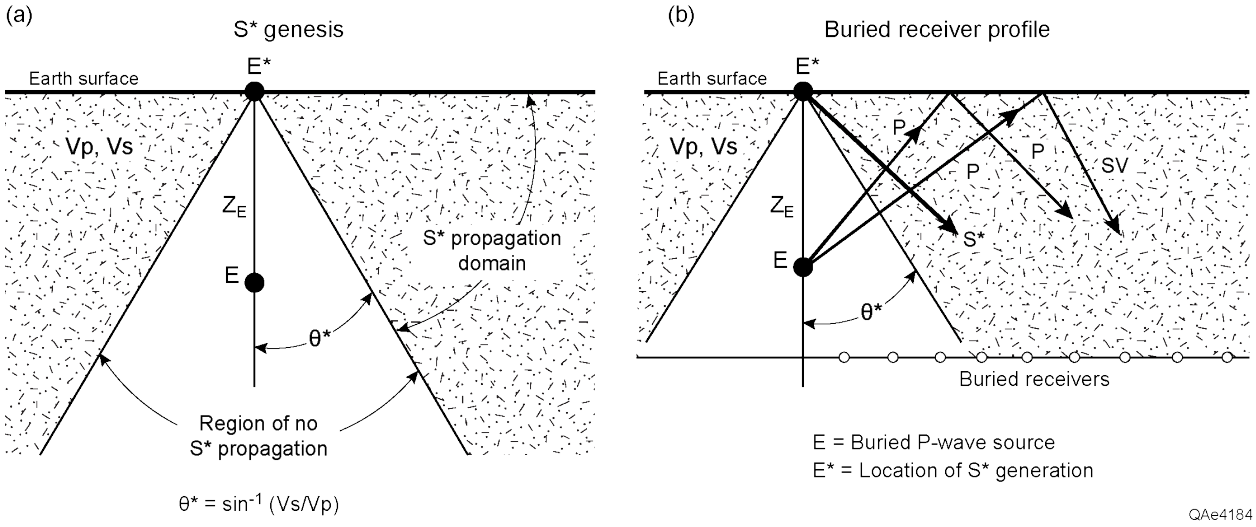

Figure A2. Principles of S* generation and propagation. From Daley, 2002.

Real Data Verification of S* Waves

Although several researchers have performed numerical modeling procedures that show the presence of an S* wave, the odd conditions required to create S* waves makes some geophysicists skeptical that such a wave exists. These "odd" requirements are:

1. The buried source must be close to the free surface at depths less than λ/2, where λ is the dominant wavelength in the wavelet that propagates upward from source station **E** (Figure A2).

2. The source must generate only P waves.

3. The S* mode is created at the earth surface directly above a buried pure-P source. Because no P-to-SV reflection occurs for a normal-incidence P wave, S* is called a **non-geometrical wave**, meaning that its genesis violates the raypath geometry required by Snell's law and the mathematics of P-to-SV reflectivity at normal incidence.

These requirements lead to the common assumption that S* is created only when a buried pure-P source is close enough to the earth-air interface to cause a rapid bulge in the free surface, which in turn results in a significant shear displacement. Although this conclusion is based on reasonable logic, the existence of S* waves cannot be accepted by most geophysicists until the waves are observed in real data generated by a real source. There are two ways to approach this objective of observing S* wave with real data:

1. Perform physical modeling in a laboratory using a simple wave-propagation medium and miniature sources and receivers, or

2. Record seismic test data in real rocks using real seismic sources and receivers.

Summaries of investigations that have used each approach are now presented.

Physical Modeling of S* Waves

The first, and the only conclusive, proof that S* waves exist in real data was produced by a series of physical modeling experiments by Kim and Behrens (1986). The view these researchers stated in their paper before they undertook their experiments was *"it appeared to not be easy – probably even impossible – to satisfy the theoretical requirements for the generation of the S* wave in a physical experiment"*. In their experiment, these researchers used piezo-electric sources and receivers embedded in a Plexiglas sheet to study P and S wave propagation. Their experiments thus involved a real wave-propagation medium, real wavelets generated by a real source, and real data recorded with real receivers. More importantly, these researchers had the correct perspective about the types of wave-modes that should be produced by buried explosive as indicated by the following quotes from their paper:

1. *One of the reasons for the difficulty of physically measuring S* waves lies in constructing a purely compressional point source: common explosive sources produce considerable shear-wave radiation.*

2. *The major effort in proving experimentally the existence of the S* wave focused on constructing a transmitter with a minimized shear-wave radiation.*

These statements indicate Kim and Behrens (1986) knew buried explosives produced both direct-P and direct-S modes. Their concept coincides with EGL's fundamental premise; i.e., all real land-based seismic sources, whether vertical-displacement type, horizontal-displacement type, buried, or surface-based, generate both direct-P and direct-S body wave modes. No real land-based seismic source generates only direct-P modes (or only direct-S modes).

Kim and Behrens (1986) were able to create a proper S* physical model because they succeeded in constructing a source that was a close approximation to a pure-P source. The standard source they used in their laboratory tests created direct-P and direct-S waves that had approximately equivalent amplitudes (Figure A3a). The direct-P and direct-S radiation lobes

illustrated in this figure have the same geometrical shapes as the direct-P and direct-S radiation lobes EGL has determined for buried explosive in tests at our Devine Test Site (Hardage and Wagner, 2014d). However, for all buried explosive sources that EGL has tested at the Devine Test Site, the amplitude of the direct-S radiation has always been greater than the amplitude of the direct-P radiation by a factor of approximately 5X (Figure A3b) and has never been so small as to be judged to be "equivalent" to direct-P amplitude as was the piezo-electric source used by Kim and Behrens. One can assume that the stiffness coefficients of the near-surface layer in which a buried explosive is positioned are the principal factors that control the P-to-S energy ratio of the illuminating direct-P and direct-SV modes produced by that source. This assumption needs to be verified by appropriate field tests.

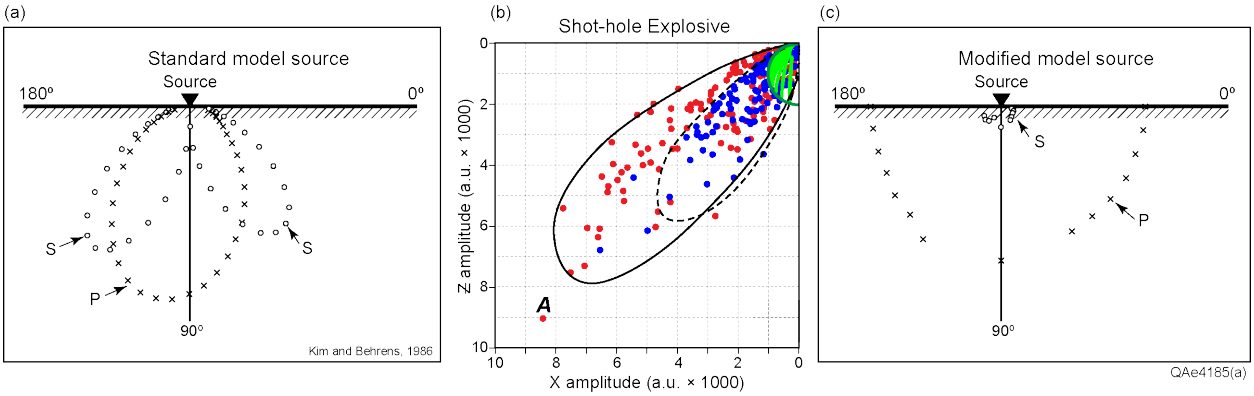

Figure A3. Comparisons of direct-P and direct-S radiation patterns produced by a piezo-electric source used in physical modeling and by a real buried explosive. (a) The standard piezo-electric source Kim and Behrens (1986) used in their laboratory to simulate seismic wave-propagation physics produced direct-P and direct-S radiation lobes with approximately equivalent amplitudes. This source could not be used to study S* waves because it was not a pure-P source. (b) Radiation patterns EGL has measured for buried explosive sources at the Devine Test Site show that direct-S modes produced by real buried explosives have amplitudes that are larger than direct-P amplitudes by a factor of 5X or larger (Hardage and Wagner, 2014d). (c) A modified version of the piezo-electric source in (a) that succeeded in reducing direct-S amplitudes to be approximately 10X smaller than direct-P amplitudes. This source reasonably approximates a pure-P source and was assumed to be appropriate for laboratory studies of S* waves (Kim and Behrens, 1986).

Kim and Behrens (1986) were able to alter their standard laboratory source so that it produced direct-S modes that had amplitudes that were approximately 10X smaller than the amplitudes of its radiated direct-P modes (Figure A3c). They proceeded with their physical modeling by assuming that this revised source was as close to being a pure-P source as they could construct. A third quote from Kim and Behrens (1986) regarding this modified source is, "*with this source the experimental detection of the S* wave arrival became possible*".

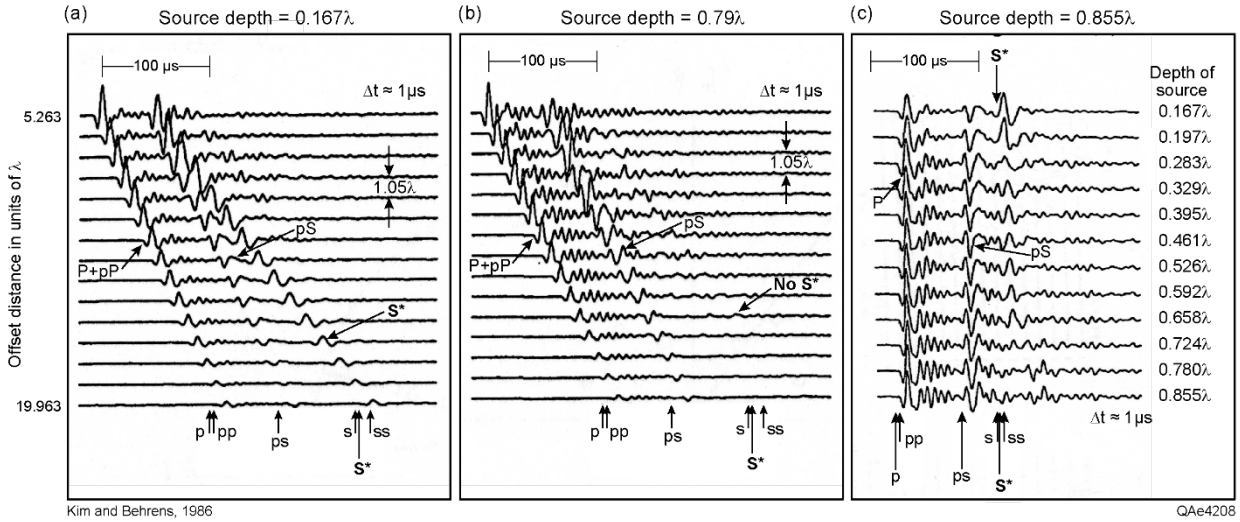

Figure A4. (a) Physical model data generated by a shallow source (depth = 0.167λ) and recorded by an offset profile of shallow receivers. (b) Data generated by a deeper source (depth = 0.79λ) and recorded by the same receiver profile. (c) Effect of source depth on S* energy. Source depth is measured in terms of λ, the dominant wavelength of the direct-P wavelet produced by the buried source. The receiver is fixed at a shallow depth as the source depth is varied. S* amplitude decreases as the source moves deeper, and the S* wave disappears into background noise when the source reaches a depth of approximately 0.7λ below the free surface. Modified from Kim and Behrens, 1986.

Key experimental data acquired by Kim and Behrens (1986) with their "quasi pure-P" source are illustrated in Figure A4. The data in Figure A4a were observed when the source was located a distance of only 0.167λ below the free surface of their 2D Plexiglass-sheet model. At a deeper depth of 0.79λ, the source generated the data shown in Figure A4b. An S* mode was observed only when the buried "pure-P" source was close to the free surface (Figure A4a). It is important to note the arrival times of events that Kim and Behrens (1986) labeled on their measurements. These events have the following meanings:

- **P**: direct-P wave radiating from the source,
- **pP**: downgoing P-wave reflected from the free surface as a P-to-P reflection,
- **pS**: downgoing S-wave reflected from the free surface as a P-to-SV converted mode produced by the upgoing **p** mode,
- **S**: direct-S mode from the source. This event is not present in the model data because a special pure-P source was used. The labeling shows where the direct-S mode should be observed,

- **sS**: downgoing S wave reflected from the free surface as an SV-SV converted mode produced by the upgoing **s** mode. This event is not present in the model data because a special pure-P source was used. The labeling shows where this mode should be observed, and

- **S***: the unique S mode created at the earth surface only if a buried pure-P source is near the free surface.

Kim and Behrens (1986) added labels to their data to indicate the arrival-time coordinates of wave modes that would have been observed if they had used their standard source that generated both direct-P and directs-S modes. The positions of these arrival times indicate some important concepts:

1. An S* wave is a real shear-wave mode embedded in a family of S-wave modes comprised of a direct-S mode and all possible converted-SV modes that reflect from the free surface above a buried pure-P source. No longer can critics claim S* is only an oddity of numerical modeling.

2. In real buried-source data, the upgoing P wave produced by a real source will no doubt create an S* wave at the earth surface, but it will be impossible to segregate this S* wave from the overlapping source-generated S-wave modes that accompany it. This statement is true only if the real buried source is closer than $\lambda/4$ to the free surface. If the source is farther than $\lambda/4$ from the earth-air interface, no (or only a weak) S* wave will be observed in real seismic data, but source-generated S waves will still be present.

3. Although an S* wave and a direct-S wave are distinct S-wave modes, one wave cannot be distinguished from the other in real S-wave data generated by buried explosives because the explosive shot has to be close to the free surface to produce S*. The time delay between the genesis of the direct-S and S* modes will be too small to recognize that there are two individual overlapping S-wave modes (Figures A4b, A4c).

4. It is not correct to claim that buried explosives do not create a direct-S mode, nor is it correct to say that what appears to be a direct-S mode produced by a buried explosive is an S* wave produced at the free surface.

The critical requirement stated in principles 2 and 3 above - that a buried source has to be close to the free surface to generate an S* wave – was verified by a second experiment done by Kim and Behrens (1986) specifically for the purpose of investigating the relationship between the amplitude of an S* wave and the depth of a buried source. Their measurements are shown in Figure A4c. These physical-model data confirm earlier numerical-model predictions that the amplitude of an S* wave diminishes as source depth increases, and that no effective S* wave is generated when the distance of the source below the free surface approaches λ, the dominant wavelength of the direct-P wavelet produced by the source. Thus an evanescent wave like S*

cannot be observed as a deep body wave that is useful for reservoir characterization, which was the focus of the Devine Test Site source experiments.

For our Devine Test Site data, we will use the simple equation $\lambda = V_P/f_{dom}$ to estimate the dominant P wavelength λ associated with the buried-explosive data we recorded. In this equation, V_P is the P-wave velocity of the upgoing P mode in the interval between the source and the free surface, and f_{dom} is the dominant wavelength in the upgoing P wavelet. Analysis of our test data indicates V_P is approximately 6000 ft/s in the near surface at our Devine Test Site and that f_{dom} for the buried-explosive test data used in this report is approximately 30 Hz. Thus we can assume λ = 200 ft. Based on this assumption, the 20-ft shot-holes that we utilized in our tests involved buried explosives that were close enough to the earth surface to generate S* waves. Probably the explosive shots at depths of 50 ft also produced S* waves. However, data acquired when the buried explosive was at depths of 100 ft and 150 ft should not contain S* waves. The important research finding is that we cannot point at any specific event in any of the buried explosive data we recorded and conclude that the event is an S* wave.

Large-Scale Investigations of S* Waves Using Real Explosives

Lash (1985) was the first it appears to do a real-data, seismic-scale experiment to investigate if S*waves exist. Lash was an investigator who was ahead of his time in some of his thinking and field test methods. For example, he was one of the early U.S. geophysicists to use VSP procedures in the 1980's to study the physics of P and S modes that propagate away from seismic source stations. Using VSP logic probably caused Lash to do the S-wave field test he described in his 1985 paper. The results of Lash's field test are illustrated in Figure A5. He deployed seven inline vertical arrays of buried receivers and detonated small explosive caps, buried a depth of 1 ft, near the top of each receiver well so he could measure the downgoing P and S radiation patterns produced by the buried explosives. He then applied reciprocity of source and receivers to describe his experiment as the 13 vertical receiver arrays in Figure A5a that are centered on a single source station. Our recent and ongoing source tests at the Devine Test Site are a modern version of Lash's approach to measuring source radiation patterns.

Lash (1985) concentrated on displaying data interpretation results in his paper and showed only a few selected samples of his recorded test data, which is unfortunate. It would be interesting to view more of his actual test data and compare those data with our test data from the Devine Test Site. Shown in Figure A5a, in addition to the source-receiver test geometry, is the basic interpretation that Lash made of his test data. Poor data quality did not allow data to be interpreted in zones **A** and **E** labeled on the figure. The fundamental research finding was that Lash could observe downgoing S energy in only the two shaded zones **B** and **D**. Because he could not observe S waves in the vertical cone **C** shown directly below the buried explosive, Lash concluded he "might be" seeing the S* exclusion zone defined by exclusion angle θ* defined in Figure A2.

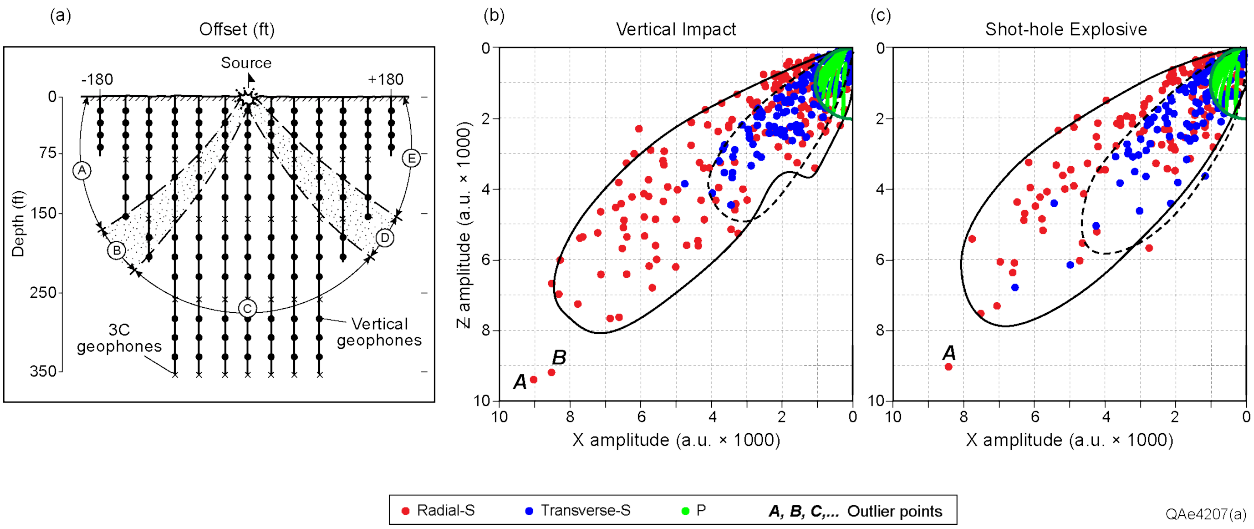

Figure A5. (a) Diagram showing how Lash (1985) arranged his seven receiver wells relative to the seven zero-offset source stations he deployed in order to interpret his test data. Because he observed radiated S energy in zones **B** and **D** but observed no S waves in the inverted cone area labeled **C**, Lash suggested that zone **C** "might be" the S* exclusion zone shown in Figure A2. Thus he concluded an S* wave "might" be present even though he could not show physical evidence of such a mode. (b) P and S radiation patterns produced by a vertical impact source. (c) P and S radiation patterns created by buried explosives in EGL field tests. The S radiation patterns in (b) and(c) show the same S-wave exclusion zone that caused Lash to assume S* waves may be present for his buried explosive test (a), yet no has ever claimed that a surface-based source (vertical vibrator or vertical impact) can create an S* wave.

We are still challenged to measure reliable S-wave amplitudes at near-vertical takeoff angles from source stations just as Lash was. However, the source-test data that we have shared with EGL sponsors cause us to conclude that Lash was observing the same S-wave radiation patterns that our Devine test data show. Our Devine test data verify that S-wave radiation patterns generated by all vertical-displacement sources, not just by buried explosives, have a reduction in S-wave radiation in the near-vertical take-off direction. Specifically, EGL's description of direct-P and direct-S radiation from a shallow (6 m) buried explosive are shown as Figure A5c and should be compared with Lash's interpretation in Figure A5a. Our test data show that "yes, there is a reduction in S radiation strength in a vertical take-off cone". However the strength of the direct-S radiation inside this reduction cone is still approximately the same as the strength of the direct-P radiation inside that S-wave reduction cone. We have documented these S-wave radiation patterns in a series of EGL sponsor reports (Hardage and Wagner, 2014a, 2014b, 2014c, 2014d).

If Lash had included surface-based sources (either vertical vibrators or vertical impacts) in his test, he would have observed the same exclusion zone **C** extending below the source station as he observed for his buried explosives. For example, the direct-P and direct-S radiation from a vertical impact source are shown as Figure A5b and should be compared with Figure A5a. Based

on this comparison, any advocate of the S* mode will have to reason why the exclusion zone observed for a buried explosive implies the existence of S* waves but the exclusion zones associated with surface-based sources do not (because a fundamental requirement of S* physics is that an S* source must be buried at a shallow depth).

To Lash's credit, he questioned in his paper if he was really seeing S* waves. However, he unfortunately used the term "S*" throughout his paper, which has caused some geophysicists to conclude that the existence of S* waves was being verified by his real field data. In fact, Lash makes no such claim and concludes his paper by stating "*synthetic records used to produce S* waves are needed to analyze source S-waves found on field records*". This statement is an acknowledgement that Lash could not point to any specific feature of his field-scale test data and state "there is an S* wave".

To our knowledge, no other real-data field tests have been done to verify whether S* waves exist in seismic exploration data generated by buried explosives. EGL's position on whether this elusive S wave is present in real, explosive-source seismic data is that, "yes, the upgoing P wave produced by a buried explosive should produce an S* wave at the free surface above the buried source if the source is sufficiently close to the surface". However that S* wave cannot be identified in the family of direct-S waves and secondary, free-surface, converted SV waves that are also produced by a buried explosive. An S* wave, when it exists, is simply a welcomed contributor to the total S wavefield that illuminates geology in real seismic data produced by shallow shot-hole explosive sources. It needs to be emphasized that no one has ever proposed that surface-based sources (vibrators and impact sources) will generate an S* mode or that an S* wave behaves as a body wave that images deep geology.

Perhaps the best commentary about the S* mode is a poem that was used as a concluding observation in the S* paper by Gutowski, el al. (1984). This poem immediately follows this paragraph and serves as a conclusion for Appendix A. The poet was not identified in the published paper, but co-author Don Wagner of this EGL report was also a co-author of the Gutowski et al. (1984) paper. Wagner recalls that the poetic conclusion to their 1984 paper was written by Sven Treitel, one of the most talented scientists who has worked in the field of reflection seismology research.

ODE TO *S**

(by Sven Treitel?)

S* is a strange wave yet most classic
and occurs in the particular case
where the source is *P* and spherically symmetric
lying but a wavelength from the surface.

The medium is an elastic half-space
the surface of course must be free.
We may consider the inhomogeneous case
but then the boundary conditions must agree.

A seismometer is placed far away
and is located considerably deep.
All the better to attenuate the Rayleigh wave
through which, hopefully, ***S**** will peep.

And now we excite the *P* source
close to the surface free.
A shear arrival then appears with great force
right where we expect nothing to be.

From careful study of rays we know
this arrival cannot appear.
Nongeometrically therefore it must grow
from the surface when *P* induces shear.

Upon this confused stage comes Freeman
dispensing geophysical advice sage and sound
"The explanation lies on the sheets of Reimann
and the contours of *p* all around."

For when de Hoop contours *p* are inflected
and these inflections press close to a pole
nongeometric waves from boundaries are diffracted
and like ***S**** play a role.

You see, ***S**** is not the only strange event,
and when the contours of de Hoop are tweaked
a host of nongeometric waves are sent
to ensure geophysical employment is peaked.

Gutowski, et al., 1984 QAe3898

Appendix B: Stiffness Coefficients Local to Source Stations

Introduction

The photographs shown in this appendix were taken within, and local to, the area of the Devine Test Site that was used to simulate vibrator source arrays. A diagram of this vibrator test area is shown as Figure B1. Source stations labeled **A**, **B**, **C**, **D**, and **E** across the source-station area are locations where photographs were taken that will be used to illustrate variations in soil stiffness coefficients associated with this vibrator test patch.

A single vertical vibrator and a single horizontal vibrator were deployed sequentially across the 4 X 4 array of 16 point-source stations shown in Figure B1. The vertical vibrator was an I/O Model AHV IV 362 weighing 60,000 lbs that was operated at an 80-percent drive level. The horizontal vibrator was a Mertz Model M18-623 weighing 54,000 lbs that was operated with a hold-down weight of 30,000 lbs and a drive level of 70 percent. Each vibrator moved across the 16-station source array pattern so that the separation between adjacent pad positions was 30 ft (9 m) in both X and Y directions. The baseplates of vertical and horizontal vibrators were positioned at the same baseplate coordinates at each of the 16 source stations within the array test area. The pad separations of 30 ft (9 m) used in these tests are separations that inline vibrators will have if they are positioned bumper-to-bumper, which is the most common vibrator positioning used by seismic data-acquisition contractors when deploying arrays of vibrators.

Each vibrator used Pelton vibrator control electronics, which should ensure that a reasonably consistent ground-force was created for each vibrator sweep at each source station. It will be assumed that a constant-magnitude vertical ground-force was applied by the vertical vibrator at each pad print because this Pelton electronics was used to control vibrator performance. Likewise it will be assumed that this same Pelton vibrator control caused a consistent-magnitude horizontal ground-force to be applied by the horizontal vibrator at each of the 16 source stations. **This assumption of a constant-magnitude ground-force at each source station is fundamental for translating soil distortions at vibrator pad imprints into conclusions about elastic properties of the near-surface at those vibrator stations.**

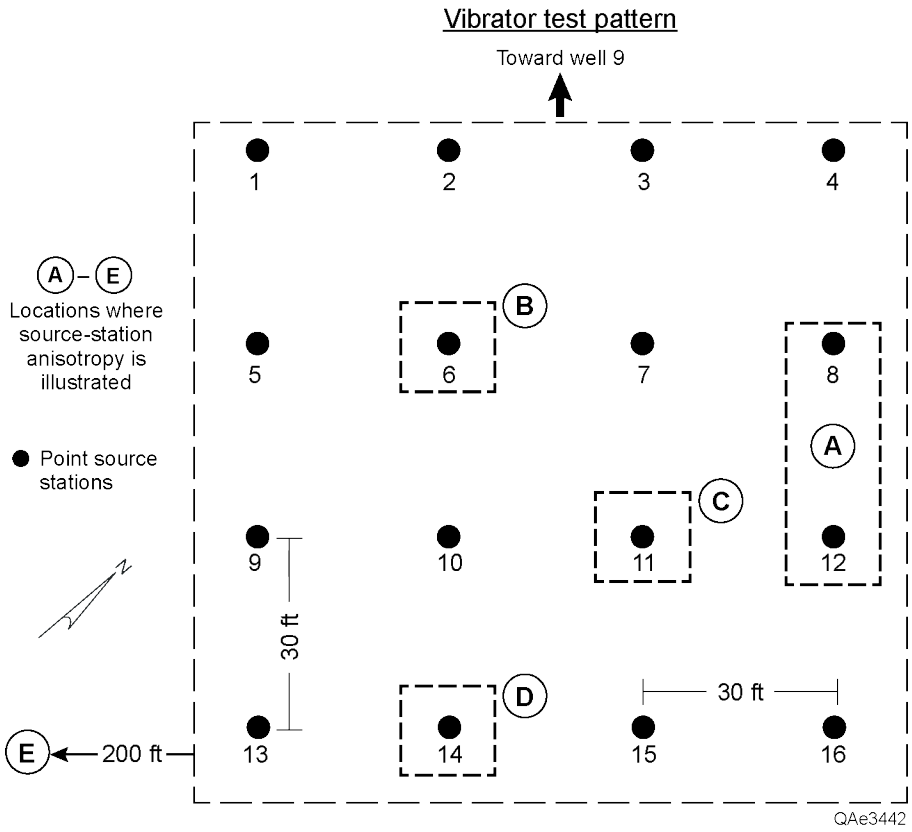

Figure B1. Vibrator-array test pattern consisting of 16 uniformly spaced source stations. Anisotropic features associated with specific vibrator baseplate positions are labeled **A, B, C, D, E**. These source-station labels will be used in photographs that follow.

Location A

Two views of surface-soil elasticity at location **A** (Figure B1) are shown in Figure B2. The depressions in the surface show soil indentations created by the baseplate of the vertical vibrator used to generate test data at point-source stations 8 and 12. The indentation at pad print 8 (Figure B2a) is obviously shallower than the indentation at pad print 12 (Figure B2b). Applying the assumption that the vibrator phase-lock electronics caused equal-magnitude ground forces to be applied at each pad location, the stiffness coefficients of the soil at location 12 must be smaller magnitude than the corresponding stiffness coefficients at location 8 only 30 ft (9 m) away. Thus we see visual evidence that significant changes in soil elasticity often occur over short distances in the immediate vicinity of seismic source stations.

These spatially varying elastic properties introduce two effects into the physics of direct-P and direct-S wavefields produced at each pad print within this 16-station test pattern. The first effect is that different elastic constants at point-source stations 8 and 12 will cause the near-surface V_P and V_S propagation velocities at these two locations to be different. These short-distance velocity variations in near-surface strata may cause measurable static time shifts in direct-P and direct-S wavefields to be produced at these two vibrator stations. Depending on

the magnitudes in the changes of elastic stiffness coefficients, these intra-array differences in static delays may be negligible or significant.

The second effect is that azimuthal anisotropic wavefield behaviors can be immediately introduced into the P and S illuminating wavefields that propagate away from vibrator stations that are “local” to such variations in surface-layer elasticity. It is difficult to decide when the distance from a vibrator pad print to a change in near-surface elastic properties is “local” to that source station and when it is not. However, it seems prudent to assume that azimuthal anisotropy effects will immediately appear in propagating wavefields when contrasts in near-surface elastic properties are inside a hemisphere of radius $\lambda/4$ centered on a source station, where λ is the dominate wavelength in the illuminating wavelet that propagates away from that source station. One outcome of this near-station anisotropy is that the direct-P and direct-SV displacements propagating in azimuth direction Θ_1 may be different magnitudes than the direct-P and direct-SV displacements propagating in azimuth direction Θ_2.

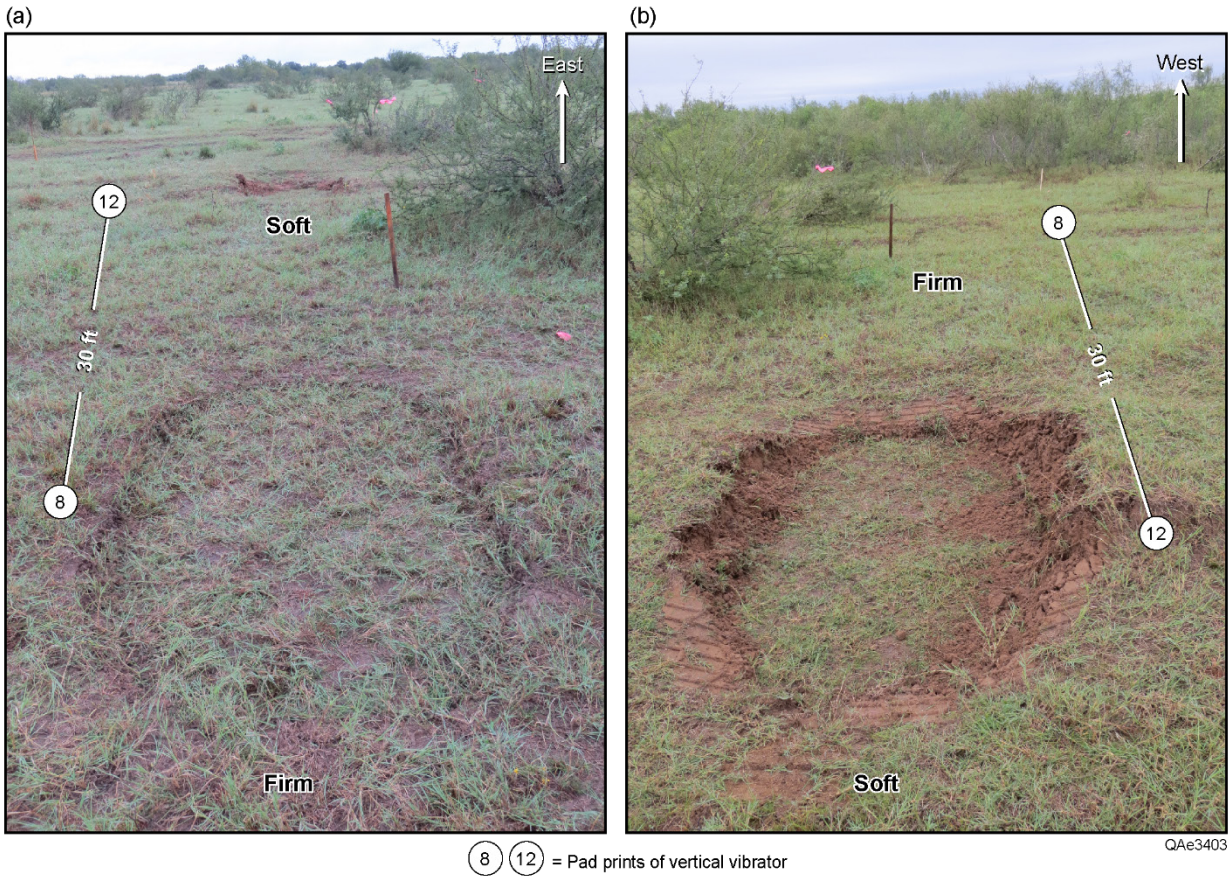

Figure B2. Two views of location **A** identified in Figure B1. (a) View looking southeast. (b) View looking northwest. Vibrator baseplates were positioned at intervals of 30 ft (9 m) in X and Y directions across this test-array pattern. Features **8** and **12** are pad imprints produced by the vertical vibrator that generated test data at point-source stations 8 and 12, respectively.

Location B

Location **B** (Figure B1) illustrates source-station anisotropy produced by local vegetation. As has been stated, vibrators were positioned in this source test so that successive pad prints were separated 30 ft (9 m) in both X and Y directions. In real seismic field operations, consistent station spacings are maintained at all source points across a seismic survey area if at all possible. Deviations from this constant-pad-separation practice occur only when forced by significant barriers such as trees, large rocks, fences, abrupt changes in surface slope, etc. This same field-practice philosophy was used in the Devine source-test program. In this source-test program, vibrator pad positions were consistently spaced at separation distances of 30 ft (9 m) and were not adjusted to avoid vegetation such as the mesquite bushes shown in Figure B3. At this vibrator position, one corner of the baseplate was atop a cluster of mesquite bushes. The roots of these bushes create a different stiffness in the near-surface than what is represented by the stiffness coefficients surrounding the remainder of the base plate where there is only shallow-rooted grass. This variation in stiffness coefficients should extend to the base of the mesquite root system and create azimuthal anisotropy over a significant vertical take-off angle range. Thus azimuthal anisotropy is present in the immediate vicinity of this vibrator station, and this anisotropy will introduce azimuthal anisotropic effects in the P and S wavefields produced at this baseplate location.

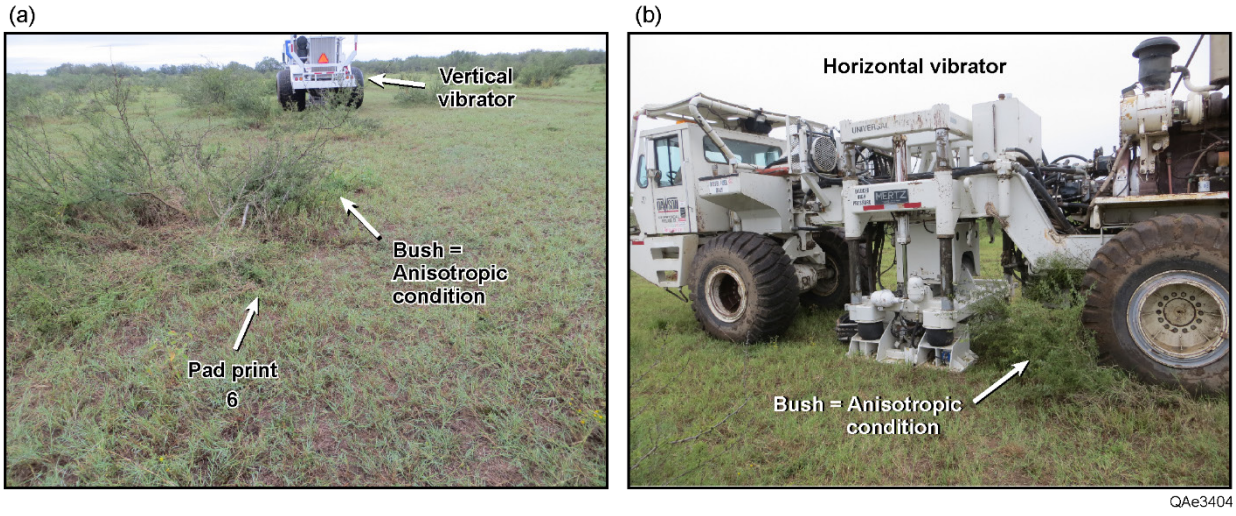

Figure B3. Location **B** identified in Figure B1 (station 6 of the vibrator-array pattern). To maintain a consistent pad spacing of 30 ft (9 m) across the array pattern, the vibrator pad at this location had to be placed partially atop mesquite bushes. (a) A vertical vibrator made the first pass across the source-array stations. (b) A horizontal vibrator made the second and third passes across the source-array area.

Location C

Almost no lateral movement of soil was created by vibrator baseplate action at any of the 16 vertical-vibrator station points within this vibrator test area except at location **C** shown in Figure B1. The lateral flow of soil away from the baseplate was significant at this one spot

(Figure B4). Thus stiffness coefficients that control lateral shearing of soil are different at this one intra-array coordinate (source station 11) than elsewhere within the 16-station test area. This variation in stiffness coefficients might affect not only wavefields produced at the pad print shown in Figure B4, but also could affect wavefields produced at neighboring pad prints. To this onsite observer, there was no evidence in the appearance of the surface soil at this location that indicated such a change in stiffness coefficients existed. Thus anisotropic soil conditions can be subtle effects that will not be readily observed even though the alteration in soil stiffness coefficients may be quite significant, as they are in this case.

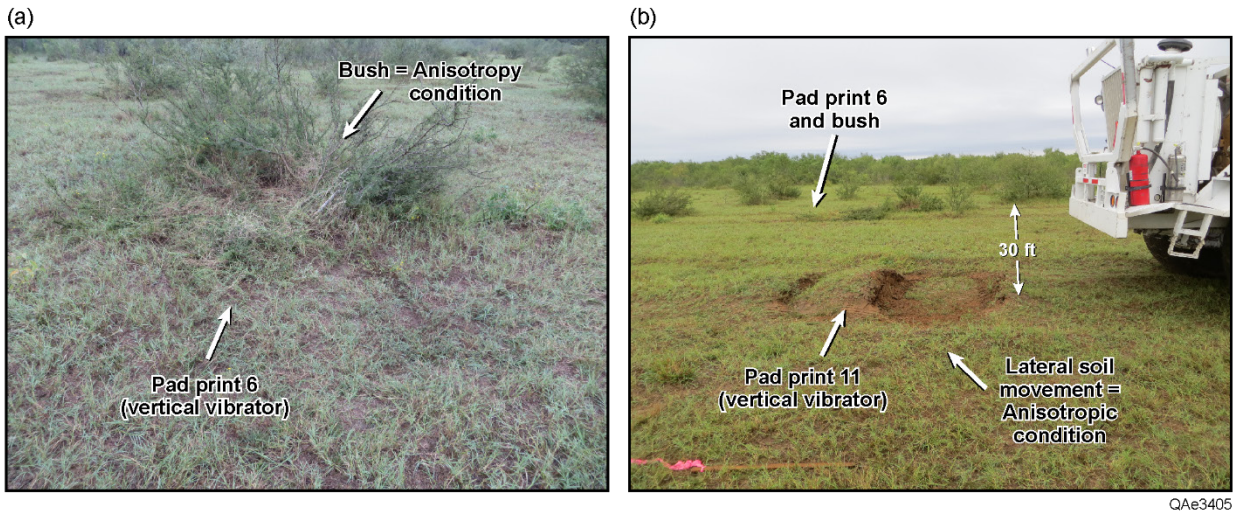

Figure B4. (a) A different view of the same source station (array station 6) shown in Figure B3a. This location will be called **Pad print 6** for this discussion about location **C** identified in Figure B1. (b) Location **C** (array station 11) is only one station away from **Pad print 6**. The soil at **Pad print 2** (location **C**) exhibited much greater lateral flow than did soil at any other source station in the array. One implication is that there may be a significant variation in intra-array S-wave statics between these two baseplate positions.

An interesting observation about the reduced-magnitude stiffness coefficients at vibrator station 11 is that vibrator wavelets generated at station 11 were consistently selected as the reference wavelets to use when analyzing vertical-vibrator and horizontal-vibrator illuminating wavelets (Figures 15 through 28 in the main text of this report). Low-magnitude stiffness coefficients at a source station thus appear to be a positive feature that implies high-amplitude source displacements will occur and robust illumination wavelets will be generated.

Location D

The most informative insights into soil mechanics across the vibrator test array was provided by examination of pad imprints left by a vertical vibrator. For completeness of reporting, a typical pad imprint created by the horizontal vibrator used in the source tests is illustrated in Figure B5. Horizontal-vibrator pad imprints did not deviate much from what is shown in this photograph at any of the 16 stations across the source array area except at

location **C** (Figure B4) where the vertical vibrator showed that stiffness coefficients that affect horizontal shearing were smaller magnitude at this one location than elsewhere across the source array.

The obvious differences in station-to-station soil stiffness coefficients that are so well documented by visual inspection of vertical-vibrator pad imprints were not as easily recognized by visual inspection of horizontal-vibrator pad imprints. In fact, report author Hardage, who was onsite for the complete data-acquisition program at Devine, confirms that differences in surface-layer elastic constants were, for all practical purposes, impossible to observe across the Devine Test Site property by visual inspection of horizontal-vibrator pad imprints. He (Hardage) has no idea why horizontal-vibrator pad imprints were more consistent than vertical-vibrator pad imprints. The difference may be due to the fact that the ground force applied by the horizontal vibrator (24,000 lbs) was significantly smaller than the ground force applied by the vertical vibrator (48,000 lbs). However, the influence of surface vegetation in introducing azimuthal anisotropy effects local to horizontal-vibrator stations could be easily recognized and inferred (Figure B3b).

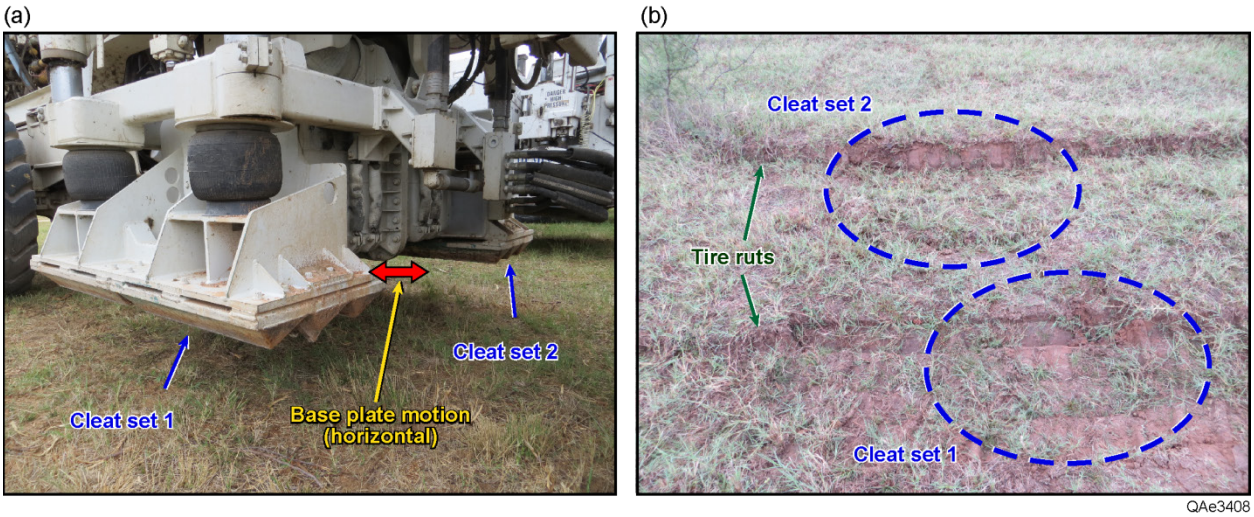

Figure B5. (a) Base plate of horizontal vibrator used in source-array tests. (b) Location **D** identified in Figure B1 (source station **14**). This view illustrates the baseplate imprint left by a horizontal vibrator. Horizontal vibrator baseplate imprints at all 16 intra-array source stations differed from what is shown in these photographs only in minor, insignificant ways.

Location E

Location **E** was approximately 200 ft (60 m) west of the vibrator test pattern (Figure B1). Figure B6a is a view looking southwest from the source-array pattern toward a vibrator that was attempting to get to the vibrator test patch. The vertical-vibrator pad print in the foreground (Figure B6a) shows the soil is quite firm at that location. However, at the position of the oncoming horizontal vibrator, there is an obvious reduction in soil stiffness only a short distance beyond that pad print (Figure B6b).

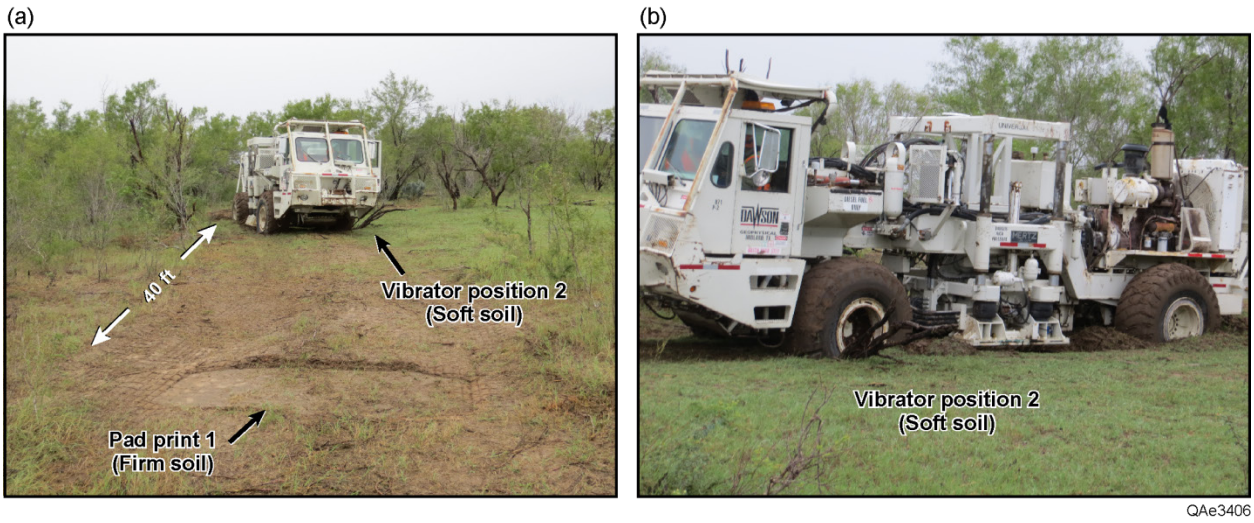

Figure B6. Location **E** identified immediately outside the source-test pattern in Figure B1. (a) This view illustrates how changes in soil elasticity cannot be recognized by visual inspection of surface conditions. The load-bearing capacity of surface soil is significantly greater at **Pad print 1** (almost no tire indentations) than it is at **vibrator position 2** (severe tire imprints). (b) Photo that emphasizes the great difference in the stiffness of the saturated soil at position **2** compared to position **1**.

The view in Figure B7 is looking northwest from location **E** toward the vibrator test pattern, which is located immediately behind **Pad print 1** in the background. The deep tire ruts in the foreground were made by the horizontal vibrator as it was driven to the vibrator test patch. There is no obvious condition visible on the surface that indicates the dramatic difference in soil stiffness that occurs at the dash-line boundary. The change in surface elevation is perhaps 2 inches (5 cm) across the complete field of view in this photograph. This small elevation change no doubt caused more runoff rainfall to temporarily accumulate in the foreground. However at the time the source tests were done, visual inspections implied soil saturation was identical across this entire field of view. There are obviously two distinct soil-elasticity domains: a soft-soil (low-magnitude stiffness coefficients) domain in the foreground of Figure B7 and a firm-soil (higher-magnitude stiffness coefficients) domain in the background.

The abrupt change in soil stiffness across the dashed boundary would be a significant contribution to azimuthal anisotropy of P and S wavefields produced at source stations local to this boundary. The root systems of the large mesquite trees in this area would create additional azimuthal anisotropic effects on locally generated direct-P and direct-S wavefields.

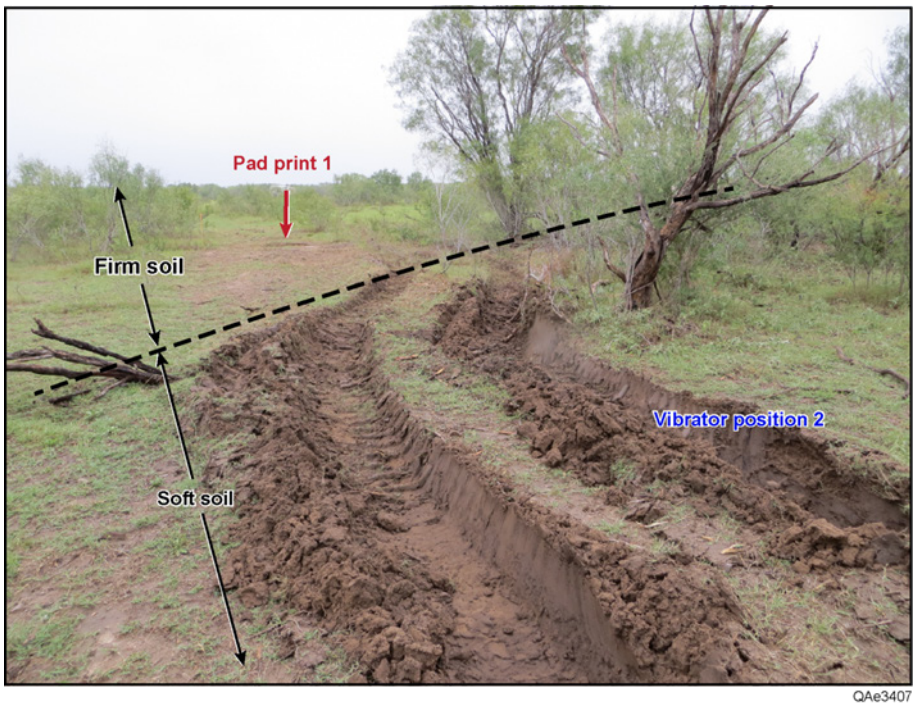

Figure B7. Opposite direction view of location **E** compared to the view in Figure B6. The dashed line shows where there is apparently an invisible change in the stiffness coefficients of the near surface. The difference in surface elevation is only 1 or 2 inches (3 to 5 cm) across this field of view.

Implications

EGL contends that when real seismic data are acquired across prospective areas, azimuthal anisotropic conditions exist at most (perhaps all?) source stations where illuminating wavefields are generated. The photos exhibited in this report illustrate that when a change in soil elasticity is found, it is common that there will be no visual surface-exposed evidence of that change in soil conditions.

The visual examples shown in this report are only a few of the real-earth conditions that contribute to azimuthal anisotropy effects in direct- P and direct-S wavefields. Figure B8 documents other causes of azimuthal anisotropy that can be encountered in real seismic field programs. Many causes of source-station azimuthal anisotropy could be proposed other than those shown in this figure. It is not difficult to recognize some surface-exposed features such as trees, fence posts, abrupt changes in surface topography, etc. that cause changes in stiffness coefficients in near-surface layers (Figure B8). One can only speculate what types of unknown buried features contribute to azimuthal anisotropy, how many such buried features exist, and where they are located relative to a source station.

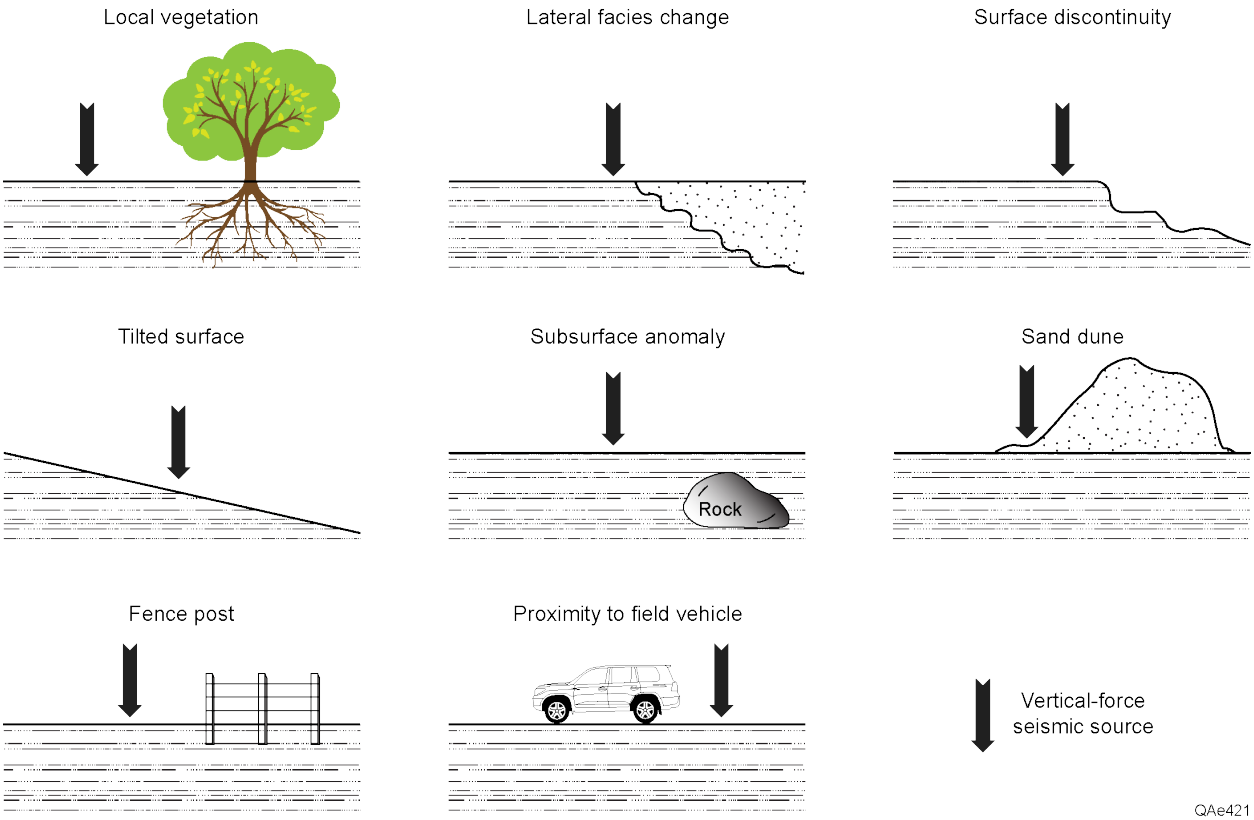

Figure B8. Common contributors to azimuthal anisotropy that can be local to seismic source stations.

Several implications result from azimuthal anisotropy effects caused by surface-exposed and buried alterations in near-surface elastic constants. Only one implication will be stressed at this point, and that is that in real seismic data generated by a vertical-displacement source (i.e. a P-wave source), direct-SH wavefields will be observed by far-field sensors in addition to direct-SV wavefields. This concept is illustrated in Figure B9. Although a vertical-displacement source produces only SV displacements, when azimuthal anisotropy is present local to a source station, the effect is that the amplitudes of SV displacement vectors vary with azimuth (Figure B9a). Thus when a far-field, 3-component receiver **G** "looks" at the direct-SV wavefield radiating from the source station in Figure B9, that receiver "sees" two orthogonal S-wave sources (Figure B9b):

1. S-wave source 1 is a source that is the vector sum of all SV displacement components produced by the vertical-displacement source that are oriented parallel to the vertical plane that passes through the source station and receiver location **G**. The vector sum of these radially oriented SV displacements pointing directly at, and directly away from, a receiver becomes a direct-SV source positioned at the source station for that particular receiver (vector **SR** in Figure B9b). If the vector sum of the radial components in quadrants **3** and **4** (Figure B9a) equals the vector sum of the radial components in quadrants **1** and **2** (Figure B9a), then **SR** = 0 when only one receiver is deployed away

from a source station, for example when VSP data are being acquired in only one receiver well. When there is perfect homogeneity around a source station, all SV displacements created by a vertical-displacement source have equal magnitude, and this vector sum will always be zero for a single receiver such as **G** (Figure B9a). The fact that direct-SV modes are consistently seen radiating from source stations in VSP data acquisition is probably the most powerful proof that azimuthal anisotropy such as that drawn in Figure B9a exists at all (or essentially all) vertical-displacement source stations. It needs to be emphasized that the orientation of vector **SR** in Figure B9b will reverse polarity at receiver **G** if the sum of all of the radial components of the outward propagating direct-SV modes in quadrants **1** and **2** is larger than the vector sum of all of the radial components of the outward propagating direct-SV modes in quadrants **3** and **4**.

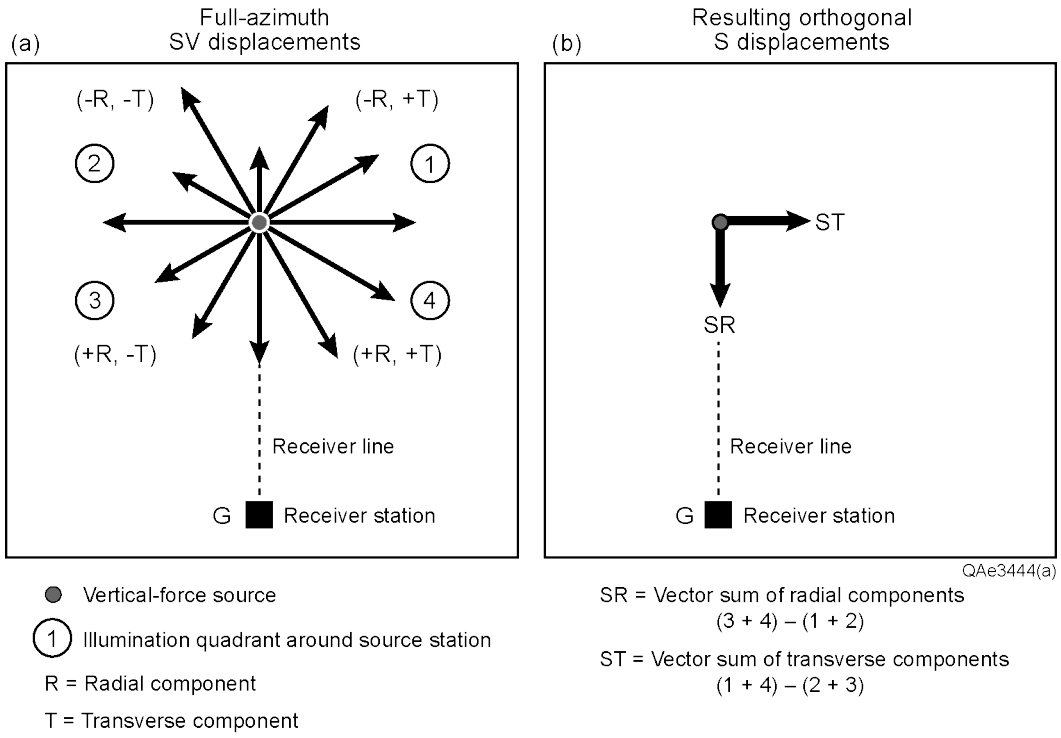

Figure B9. The concept that a far-field receiver **G** sees a vertical-displacement source **X** as a direct-SV source if the propagation medium is isotropic but as two orthogonal S-wave sources if there is azimuthal anisotropy local to the source station. (a) Map view of the 360-degree radiation of direct-SV displacements produced by a vertical-displacement source. (b) Vector sum of all the azimuthally radiated direct-SV displacements can be represented as two orthogonal vectors.

2. S-wave source 2 is a source that is the vector sum of all of the SV displacement vectors that are perpendicular to the vertical plane passing through the source station and receiver station **G**. This vector sum is zero when only one receiver is deployed (e.g. as in VSP data acquisition) if there is no azimuthal anisotropy because the left-pointing vector

components have the same amplitudes as the right-pointing vector components. However, when azimuthal anisotropy is present local to the source station, either the right-pointing SV displacements will be greater than the left-pointing as drawn for positive-polarity vector **ST** in Figure B9b, or vice versa, which would create left-pointing negative-polarity **ST** vector. The end result is that SV displacements that are normal to the source-receiver vertical plane do not cancel. The vector sum of these transverse SV displacements then becomes a transverse-oriented direct-SH source positioned at the source station for receiver **G**. If a second receiver is positioned at a different azimuth from the source station than is receiver **G**, that second receiver will react to a different set of radiation quadrants than **G** and may, or may not, see positive-polarity **SR** and **ST** displacements as **G** does.

The terms ***SV*** and ***SH*** that EGL uses to describe these two orthogonal S-wave sources refer to the directions of source displacement vectors relative to the vertical plane that passes through the source and a receiver station, not to the SV and SH wave modes that propagate in isotropic media. To minimize confusion as to what the terms **SV** and **SH** mean in EGL research, we are attempting to use the term ***SR*** instead of the term ***SV*** to describe displacements in the vertical source-to-receiver plane, and the term ***ST*** instead of the term ***SH*** to describe displacements transverse to a vertical source-to-receiver plane (Figure B9). However, we find many people in the geophysical community prefer to retain the terms **SV** and **SH** to describe the directions of vector displacements relative to vertical source-to-receiver planes. EGL will attempt to use whichever notation and language make sense to the audience that is being addressed.

The key point is that source-station azimuthal anisotropy allows the 360-degree radiation of direct-SV displacements by a vertical-displacement source (Figure B9a) to be described as two orthogonal SV displacement vectors (Figure B9b). These orthogonal-displacement sources will, in turn, cause fast-S and slow-S wave modes to radiate from a vertical-displacement source station in the same manner that two orthogonal horizontal vibrators do.

One uncertainty that source-station anisotropy introduces into direct-S data produced by a vertical-displacement source is that the polarity of the illuminating direct-S wavefields can vary from source station to source station. For example if the sum of the radial components in quadrants **3** and **4** of Figure B9a is greater than the vector sum of the radial components in quadrants **1** and **2**, then the polarity of the radial-S source is shown by vector **SR** in Figure B9b. However, if the vector sum of the radial components in quadrants **3** and **4** is less than the vector sum of the radial components in quadrants **1** and **2**, the direction of vector **SR** reverses, as does the polarity of the radiated S wavefield. This same variability in data polarity exists for the transverse vector sum labeled **ST** in Figure B9b.

A report has been provided to EGL sponsors that illustrates how this station-to-station variability in radiated direct-S polarity can be controlled when processing 3D data and possible effects and limitations that need to be considered when processing 2D data and VSP data (Hardage, 2015).

Conclusions for Appendix B

Azimuthal anisotropy exists at the great majority, and probably at all, real seismic source stations. As a result, far-field receivers do not see a vertical-displacement source as only a direct-SV source but as two orthogonal horizontal-displacement sources, which is the same deployment geometry used to generate direct-S data with horizontal vibrators. The S-wave displacements produced by these two orthogonal sources need to be described relative to the vertical plane that passes through each source-receiver pair involved in a seismic survey. Even though these two orthogonal S-wave sources are created by vector summations of SV displacements produced by a vertical-displacement source, the language used to describe the resulting orthogonal-displacement sources should be the same terminology used to describe orthogonal-displacement sources, such as two orthogonal horizontal vibrators. If a person uses the terms SV and SH to describe orthogonal horizontal vibrators at a source station, she/he should use the same terms, SV and SH, to refer to the orthogonal-displacement sources that are produced by a single vertical-displacement source positioned when azimuthal anisotropy exists around a source station. If a person prefers to use terms other than SV and SH to describe data generated by orthogonal horizontal vibrators, then those preferred terms should also be used for the orthogonal-displacement S-wave sources produced by a single vertical-displacement source.

Appendix C: Vertical Profile Data Used to Construct Source-Array Data

This Appendix shows big-picture views of the test data that were acquired in this investigation of intra-array source statics at the Devine Test Site. Only a few selected examples of data acquired with the full 42-station vertical receiver array are shown here. These example vertical profiles should be sufficient to allow readers to evaluate the quality of the data acquired in this field experiment. The data exhibited in this Appendix are typical examples of the test data, not special exemplary examples.

Data generated by a buried explosive at a source station in the shot-hole patch are displayed in Figure C1. Data generated by vertical, radial-horizontal, and transverse-horizontal vibrators at a source station in the vibrator test patch follow as Figures C2, C3, and C4, respectively. For each of these sources, every 3C geophone in the vertical-well receiver array has been mathematically rotated in 3D space so that one of its three orthogonal sensors is aligned with the downgoing direct-P displacement (Figure C1a), a second sensor is aligned with the downgoing direct-ST displacement (Figure C1b), and the third sensor is aligned with the downgoing direct SR displacement (Figure C1c). It is important that the illuminating wavelets that are analyzed be true body waves and not be contaminated by critical refractions traveling along horizontal interfaces to a receiver station. Because of the large offset distance (approximately 1000 ft) between receiver Well 9 and each source test patch, only data acquired by 3C geophones positioned in the lower half of the vertical array of receivers (1000 ft to 2125 ft) were used to study intra-array source static effects. The specific data windows used in the main text as examples of direct-P, direct-SR, and direct-ST wavelets generated by each source are defined in each vertical profile (Figures C1 through C4).

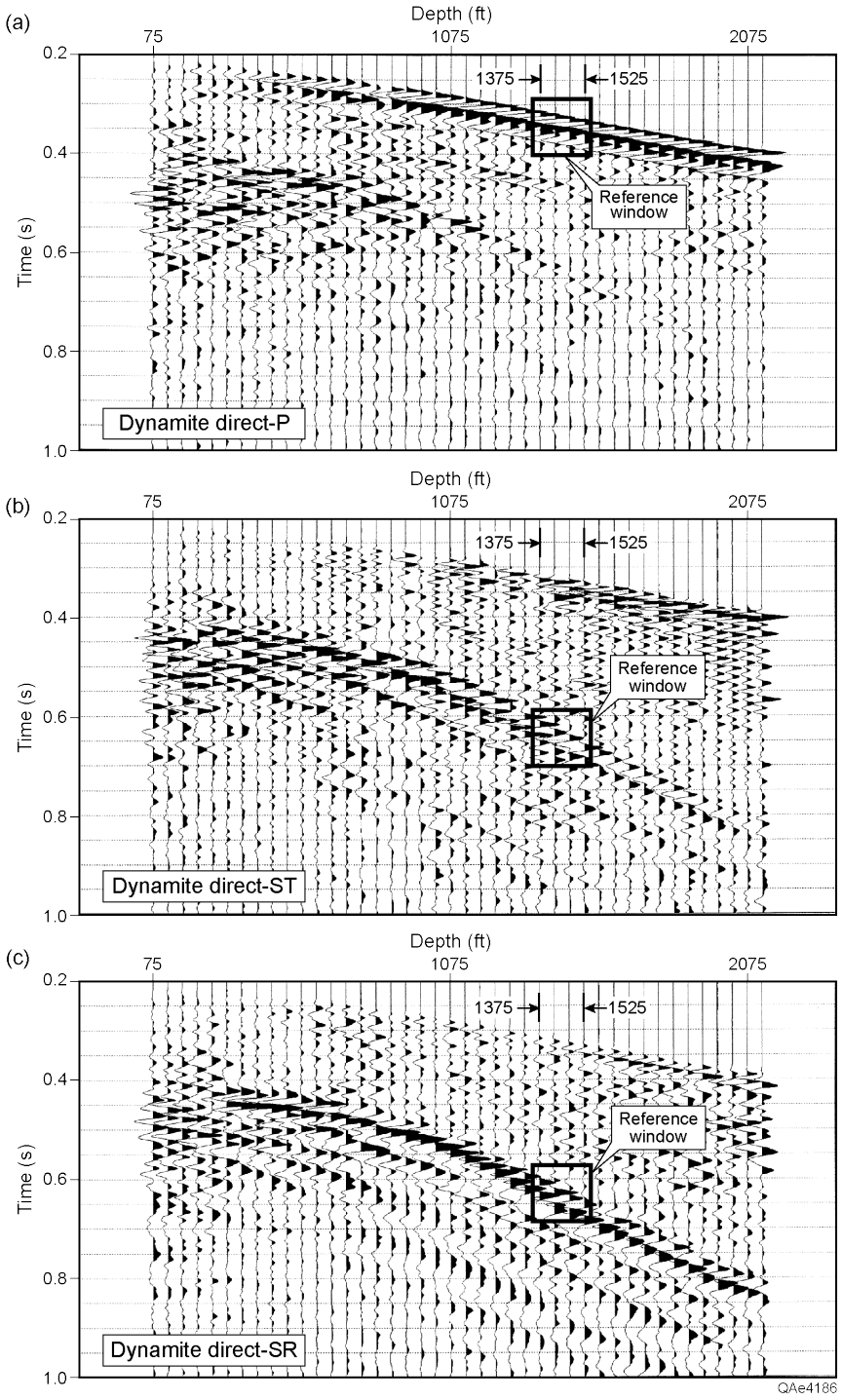

Figure C1. The 42-station profile used to analyze direct-P, direct-ST, and direct-SR modes created by a **buried explosive**. (a) Response of horizontal geophones H1 after they are oriented in the vertical source-receiver plane to align with the downgoing direct-P displacement vector. (b) Response of horizontal H2 geophones after they are oriented perpendicular to the vertical source-to-receiver plane and aligned with downgoing direct-ST displacements. (c) Response of vertical Z geophones after they are oriented in the vertical source-to-receiver plane so they are aligned with downgoing direct-SR displacements.

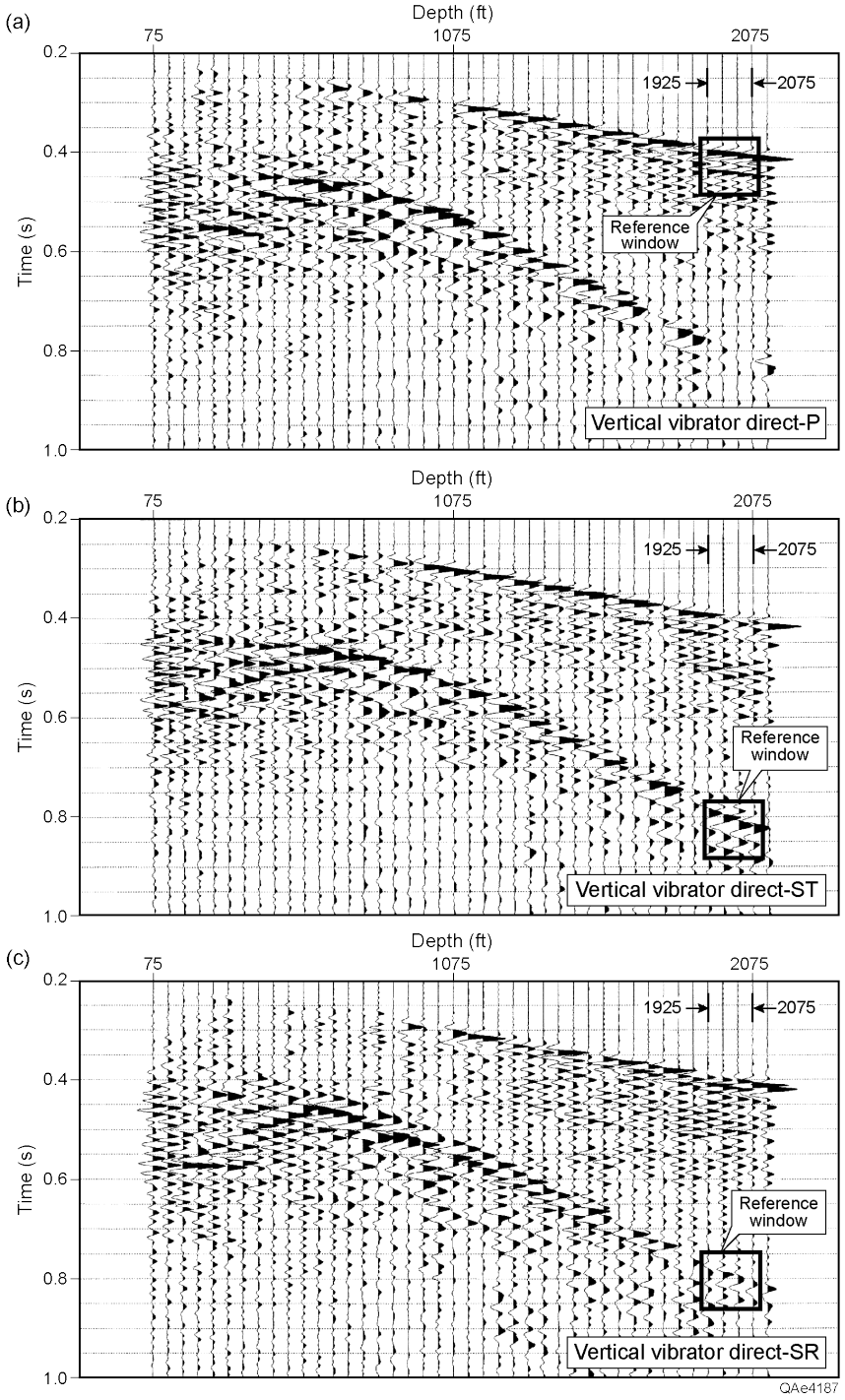

Figure C2. The 42-station profile used to analyze direct-P, direct-ST, and direct-SR modes created by a **vertical vibrator**. (a) Response of horizontal geophones H1 after they are oriented in the vertical source-receiver plane to align with the downgoing direct-P displacement vector. (b) Response of horizontal H2 geophones after they are oriented perpendicular to the vertical source-to-receiver plane and aligned with downgoing direct-ST displacements. (c) Response of vertical Z geophones after they are oriented in the vertical source-to-receiver plane so they are aligned with downgoing direct-SR displacements.

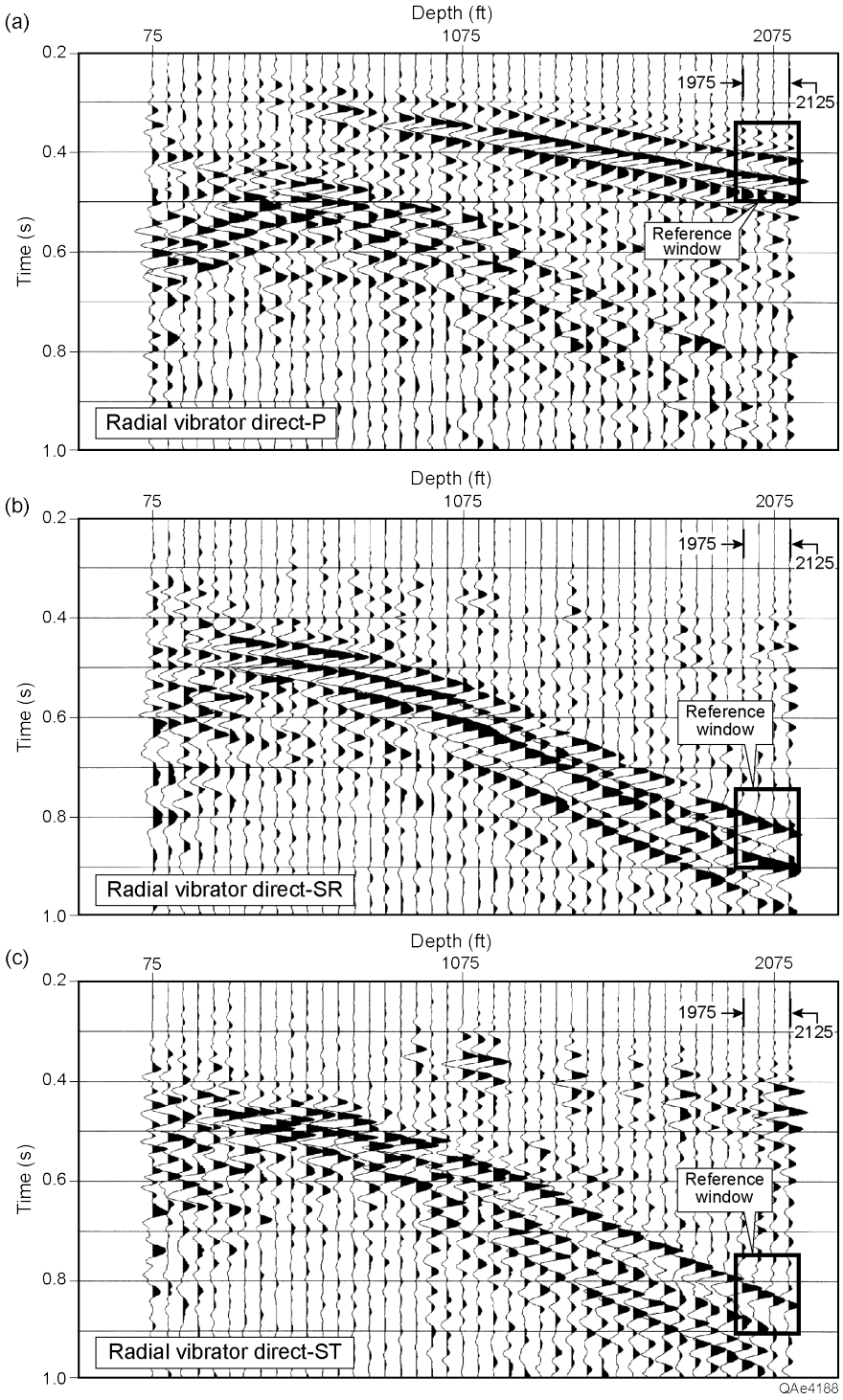

Figure C3. The 42-station profile used to analyze direct-P, direct-ST, and direct-SR modes created by a **radial-horizontal vibrator**. (a) Response of horizontal H2 geophones after they are oriented perpendicular to the vertical source-to-receiver plane and aligned with downgoing direct-ST displacements. (b) Response of vertical Z geophones after they are oriented in the vertical source-to-receiver plane so they are aligned with downgoing direct-SR displacements. The weak-amplitude direct-P mode produced by the radial-horizontal vibrator was not analyzed.

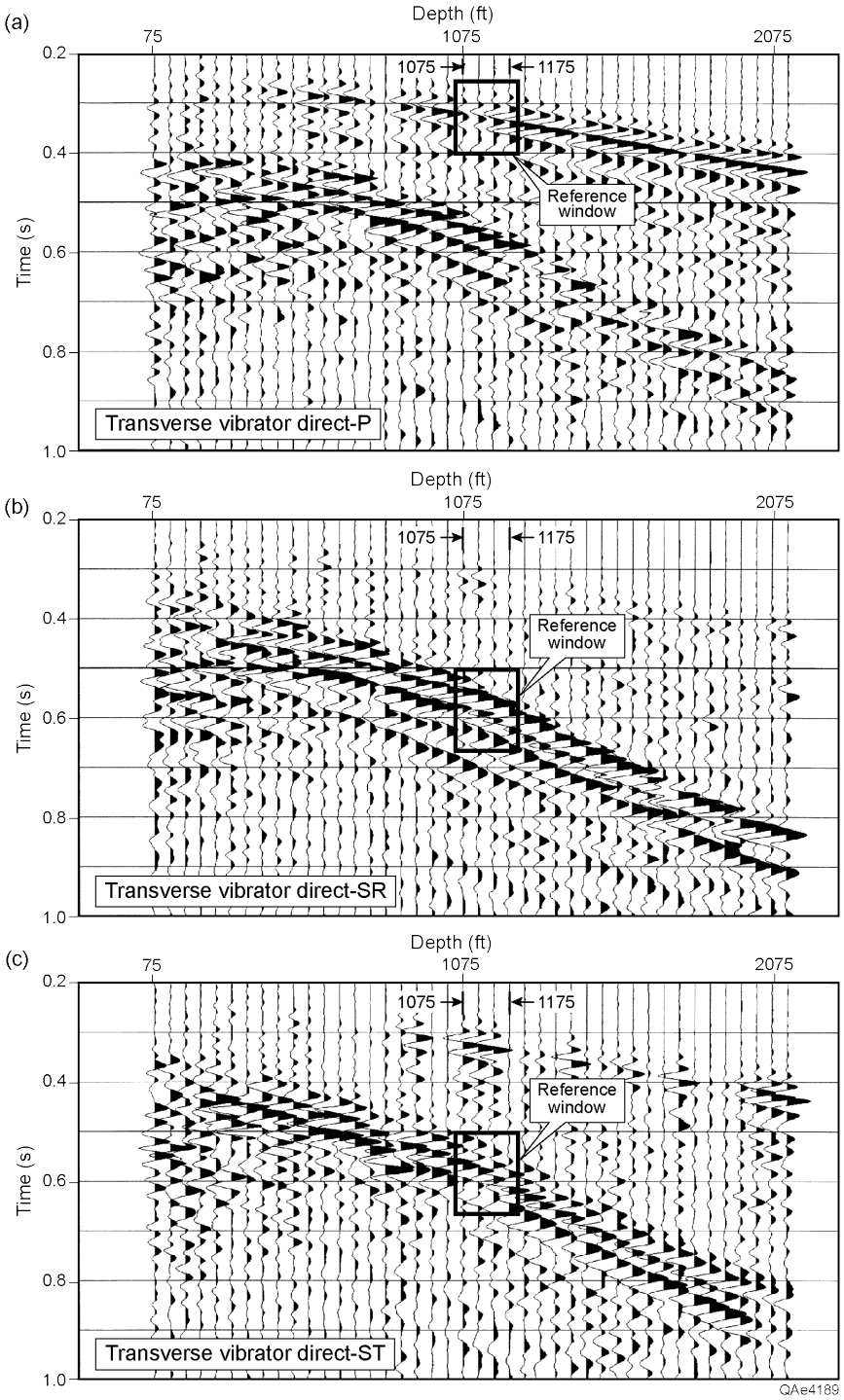

Figure C4. The 42-station profile used to analyze direct-P, direct-ST, and direct-SR modes created by a **transverse-horizontal vibrator**. (a) Response of horizontal H2 geophones after they are oriented perpendicular to the vertical source-to-receiver plane and aligned with downgoing direct-ST displacements. (b) Response of vertical Z geophones after they are oriented in the vertical source-to-receiver plane so they are aligned with downgoing direct-SR displacements. The weak-amplitude direct-P mode generated by the transverse-horizontal vibrator was not analyzed.

References

Daley, P.F., and F. Hron, 1988, A non-geometric SH-arrival: Geophysical Prospecting, **36**, p. 430-445.

Daley, P.F., 2002, S* shear energy from a P-wave source: CREWES Research Report, **14**, p. 1-21.

Fertig, J., 1984, Shear waves by an explosive point-source – the earth surface as a generator of converted P-S waves: Geophysical Prospecting, **32**, p. 1-17.

Fertig, J., and P. Krajewski, 1989, Acquisition and processing of pure and converted shear waves generated by compressional wave sources: Surveys in Geophysics, **10**, p. 103-132.

Gutowski, P.R., F. Hron, D.E. Wagner, and S. Treitel, 1984, S*: Bulletin of the Seismological Society of America, **74**, p. 61-78.

Hardage, B.A., and D. Wagner, 2014a, 2D modeling of direct-S and direct-P wavefields, part 1, modeling principles and examples: EGL Sponsor Report distributed to sponsors and placed in the private Members Area of the EGL Web site.

Hardage, B.A., and D. Wagner, 2014b, 2D modeling of direct-S and direct-P wavefields, part 2, P and S radiation patterns: EGL Sponsor Report distributed to sponsors and placed in the private Members Area of the EGL Web site.

Hardage, B.A., and D. Wagner, 2014c, 2D modeling of direct-S and direct-P wavefields, part 3, reflectivity modeling using real log data: EGL Sponsor Report distributed to sponsors and placed in the private Members Area of the EGL Web site.

Hardage, B.A., and D. Wagner, 2014d, Comparison of direct-S modes produced by vertical-force and horizontal-force sources: EGL Sponsor Report distributed to sponsors and placed in the private Members Area of the EGL Web site.

Hardage, B.A., 2015, Processing direct-S data produced by vertical-displacement sources – data polarity concepts and velocity analysis strategies: EGL Sponsor Report distributed to sponsors and placed in the private Members Area of the EGL Web site.

Hron, F., and B.G. Mikhailenko, 1980, Discovery of a new nongeometrical S* arrival generated at a free interface: Proceedings og the 17th Assembly of the ESC, Budapest, p. 293-297.

Hron, F., and B.G. Mikhailenko, 1981, Numerical modeling of nongeometrical effects by the Alekseev-Mikhailenko method: Bulletin of the Seismological Society of America, **71**, p. 1011-1029.

Kim, J.Y., and J. Behrens, 1986, Experimental evidence of S* wave: Geophysical Prospecting, **34**, p. 100-108.

Lash, C.C., 1985, Shear waves produced by explosive sources: Geophysics, **50**, p.1399-1409.

Acknowledgements

Dawson Geophysical provided the vertical and horizontal vibrators that generated much of the source test data discussed in this report. Austin Powder provided the buried explosives and firing caps that were used. Halliburton and Avalon Sciences Ltd combined resources to provide the 42-station vertical receiver array. These source tests could not have been done without the assistance of these supporters of the Exploration Geophysics Laboratory (EGL).

The extractions of the source wavelets that illustrate direct-P and direct-S modes produced by the various source options that were tested were done by Daniela Costa Melo and Andrey Marcos, two Brazilian undergraduates who did summer internships at EGL in 2015. These students had never worked with any VSP seismic data, but they quickly learned how to operate EGL's workstations and software, to access EGL databases, wrote their own code to do proper rotations of VSP 3-component geophones that would segregate P and S wave modes, and worked diligently on their summer assignments. Thank you, Daniela and Andrey. Without your assistance, this report would have been issued at a much later date.